



UNIVERSITÀ DI PISA

## Department of Physics Masters Degree in Physics

# Characterization of monolithic CMOS pixel sensors for charged particle detectors and for high intensity dosimetry

**6 Candidate:**  
Ravera Eleonora

Supervisor:  
Francesco Forti

7 Academic year 2021/2022

# **Contents**

9	<b>Introduction</b>	<b>5</b>
10	<b>1 Use of pixel detectors</b>	<b>6</b>
11	1.1 Tracking in HEP . . . . .	6
12	1.1.1 Hybrid Pixels at LHC . . . . .	8
13	1.1.2 Monolithic Active Pixels . . . . .	9
14	1.2 Other applications . . . . .	13
15	1.2.1 Applicability to FLASH radiotherapy . . . . .	13
16	<b>2 Pixel detectors</b>	<b>18</b>
17	2.1 Signal formation . . . . .	18
18	2.2 Charge Coupled Devices . . . . .	20
19	2.3 Hybrid pixels . . . . .	20
20	2.4 CMOS MAPS and DMAPS . . . . .	22
21	2.4.1 DMAPS: large and small fill factor . . . . .	23
22	2.4.2 A modified sensor . . . . .	24
23	2.5 Analog front end . . . . .	24
24	2.5.1 Preamplifier . . . . .	26
25	2.6 Readout logic . . . . .	26
26	<b>3 MAPS devices description</b>	<b>30</b>
27	3.1 TJ-Monopix1 . . . . .	30
28	3.1.1 The sensor . . . . .	32
29	3.1.2 Front end . . . . .	33
30	3.1.3 Readout logic . . . . .	36
31	3.2 ARCADIA MD1 . . . . .	38
32	3.2.1 The sensor and the front end . . . . .	39
33	3.2.2 Readout logic and data structure . . . . .	41
34	<b>4 Characterization</b>	<b>46</b>
35	4.1 TJ-Monopix1 characterization . . . . .	46
36	4.1.1 Threshold and noise: figure of merit for pixel detectors . . . . .	46
37	4.1.2 Linearity of the ToT . . . . .	51
38	4.1.3 Calibration of the ToT . . . . .	51
39	4.1.4 Changing the bias . . . . .	56
40	4.1.5 Measurements with radioactive sources . . . . .	59
41	4.1.6 Dead time measurements . . . . .	65
42	4.2 ARCADIA-MD1 characterization . . . . .	67

43	<b>5 Test beam measurements</b>	<b>71</b>
44	5.1 Apparatus description . . . . .	72
45	5.1.1 Accelerator . . . . .	72
46	5.1.2 Mechanical carriers . . . . .	72
47	5.2 Measurements . . . . .	73

# <sup>48</sup> Introduction

<sup>49</sup> Since the 1980s, when the fabrication of device with very small electrodes (50-100  $\mu\text{m}$ )  
<sup>50</sup> became a practical possibility, pixel detectors have been widely employed for imaging and  
<sup>51</sup> tracking charged particles in the vertex region of experiments at accelerators. Thanks to  
<sup>52</sup> their excellent spatial resolution, today even better than 10  $\mu\text{m}$ , they allow for true three  
<sup>53</sup> dimensional space-point determination even at high particle fluxes and in particular for  
<sup>54</sup> the identification of secondary vertices of short-lived particles such as  $\tau$  and B mesons.  
<sup>55</sup> Requirement imposed by accelerators are stringent and they will become even more so  
<sup>56</sup> with the increase of luminosity; in this scenario CMOS Monolithic Active Pixel Sensors  
<sup>57</sup> (MAPS), based on the technology of CMOS cameras, are being developed to improve  
<sup>58</sup> the performance of the hybrid pixel detectors, which currently constitute the state-of-art  
<sup>59</sup> for large scale pixel detector, in particular by reducing the amount of material, power  
<sup>60</sup> consumption and pixel dimension. Indeed, while hybrid pixels are made by two parts, the  
<sup>61</sup> sensor and the electronics, welded together through microconnections, the MAPS integrate  
<sup>62</sup> them all on the same wafer.

<sup>63</sup> Experiments such as ALICE at LHC and STAR at RHIC have already introduced the  
<sup>64</sup> CMOS MAPS technology in their detectors. ALICE Tracking System (ITS2), upgraded  
<sup>65</sup> during the LHC long shut down in 2019-20, was the first large-area ( $\sim 10 \text{ m}^2$ ) silicon vertex  
<sup>66</sup> detector based on CMOS MAPS. Thanks to the reduction of the material budget, ITS2,  
<sup>67</sup> which uses the ALPIDE chip developed by ALICE collaboration, obtained an amazing im-  
<sup>68</sup> provement both in the position measurement and in the momentum resolution, improving  
<sup>69</sup> the efficiency of track reconstruction for particle with very low transverse momentum (by  
<sup>70</sup> a factor 6 at  $p_T \sim 0.1 \text{ GeV}/c$ ). Further advancements in CMOS MAPS technology are  
<sup>71</sup> being aggressively pursued for the ALICE ITS3 and the Belle II vertex detector upgrades  
<sup>72</sup> (both foreseen around 2026-27), and by the R&D53 collaboration for the upgrade at HL-  
<sup>73</sup> LHC, with the goals of further reducing the sensor thickness and improving the readout  
<sup>74</sup> speed of the devices, while keeping power consumption at a minimum.

<sup>75</sup> Beside tracking, the development of pixel detectors is a very active field with many  
<sup>76</sup> applications: a noteworthy example of detector originally used in particle physics and later  
<sup>77</sup> employed for medical imaging, in space detectors and for art authentication, is Medipix,  
<sup>78</sup> a hybrid system developed at CERN within the Medipix collaboration. Among medical  
<sup>79</sup> applications, a possible use of CMOS MAPS could be in dosimetry: in the last few years  
<sup>80</sup> the search of radiotherapy oncological treatments with high intensity beams (FLASH  
<sup>81</sup> mode) is requiring new dosimeters, both for the therapies as well as new beam-monitors  
<sup>82</sup> (especially for focused very high energy electron beams), which are capable of deal with  
<sup>83</sup> extreme dose rate (up to 40 Gy/s).

<sup>84</sup> I have studied the characteristics of two ALPIDE-like CMOS MAPS chips and tested  
<sup>85</sup> them under different front end configuration. The first chip, the TJ-Monopix1 from the  
<sup>86</sup> Monopix series, is a TowerJazz MAPS fabricated in 180 nm CMOS technology with an

active area of  $1 \times 2 \text{ cm}^2$  ( $448 \times 224$  pixels) and is one of the prototypes for the Belle II vertex detector upgrade. The second chip, called Main Demonstrator-1, has an active area of  $1.28 \times 1.28 \text{ cm}^2$  ( $512 \times 512$  pixels) is produced by LFoundry in 110 nm CMOS technology and designed by the ARCADIA (Advanced Readout CMOS Architectures with Depleted Integrated sensor Arrays) group; it is intended to be a general purpose device with possible use in medical scanners, space experiments, future lepton colliders and also possibly X-ray applications with thick substrates. The main differences between the two chips are in the output signal type and in the readout sequence of the matrix. Concerning the former, TJ-Monopix1 returns an analog output information, that is the time over threshold of the pulse, which can be related with the charge released by the particle in the sensor, while MD1 returns only a digital information; regarding the latter, instead, TJ-Monopix1 has a completely sequential readout, while MD1 roughly combines the information of the hits before the readout in order to reduce the data transmission time.

I have set up the test systems for the two chips in the INFN clean laboratories and characterized the devices electrically and with radioactive sources in terms of threshold, noise, dead time and analog response. The mean minimum stable threshold evolved through different generation of chips and nowadays it is less than  $500 \text{ e}^-$ , allowing thinner sensors with smaller signals: TJ-Monopix1 has proven to be in agreement with this trend, having a threshold of  $\sim 400 \text{ e}^-$ , to be compared with the  $2000 \text{ e}^-$  signal expected for a minimum ionizing particle in an epitaxial layer of  $25 \mu\text{m}$ . Moreover, since one of the main challenges of MAPS are the differences between pixels due to process parameters variation across the wafer, which make the sensor response nonuniform, I have measured the threshold and noise dispersion across the matrix, which I found to be  $40 \text{ e}^-$  and  $2 \text{ e}^-$  respectively. I have also studied the response of the analog signal recorded by TJ-Monopix1, that is the time over threshold, and performed a calibration of its absolute value using a Fe55 X-ray source. All these measurements are important to verify the design parameters of the chip and to validate the chip simulation.

As conclusion of the measurement campaign, we have tested TJ-Monopix1 at very high intensity using the electron beam of the new ElectronFlash accelerator designed for both medical research and R&D in FLASH-radiotherapy and recently installed at Santa Chiara hospital in Pisa. I have participated in the design of the setup needed for testbeam measurement and I am currently working on the analysis of the data collected.

<sup>119</sup> **Chapter 1**

<sup>120</sup> **Use of pixel detectors**

<sup>121</sup> This chapter tries to summarize the main applications of pixel detectors while a description  
<sup>122</sup> of the technological implementation is presented in chapter 2. In the following sections I  
<sup>123</sup> will also use terms such as hybrid pixels, monolithic active pixel system (MAPS), Charge  
<sup>124</sup> Coupled Devices (CCDs), Depleted Field Effect Transistor sensors (DEPFET) that will  
<sup>125</sup> discussed later.

<sup>126</sup> The relation between the development of cameras and that of pixel detectors dates back  
<sup>127</sup> to 1969, when the idea of CCDs, for which Boyle and Smith were awarded the Nobel Prize  
<sup>128</sup> in Physics in 2009, revolutionized photography allowing light to be captured electronically  
<sup>129</sup> instead of on film. Even though the CMOS technology already existed at the time the  
<sup>130</sup> CCDs spread, the costs of production were too high to allow the diffusion of these sensors  
<sup>131</sup> for the following 20 years. From that moment on, the fast diffusion of CMOS was mainly  
<sup>132</sup> due to the less cost than CCD, and the less power supply required. Nowadays CCDs  
<sup>133</sup> are still preferred over MAPS in astronomy, where the astronomical sources' rate are low  
<sup>134</sup> enough to cope with slow readout time (tens of ms).

<sup>135</sup> The principal use cases of pixel detectors are particle tracking and imaging: in the  
<sup>136</sup> former case individual charged particles have to be identified, in the latter instead an  
<sup>137</sup> image is obtained by the usually un-triggered accumulation of the impinging radiation.  
<sup>138</sup> Also the demands on detectors performance depends on their usage, in particular tracking  
<sup>139</sup> requires high spatial resolution, fast readout and radiation hardness.

<sup>140</sup> **1.1 Tracking in HEP**

<sup>141</sup> In the early days of high-energy physics gaseous detector were used for tracking and  
<sup>142</sup> there was no need to replace them since they had a sufficient spatial resolution ( $100 \mu\text{m}$ ).  
<sup>143</sup> Since 1974, with the measurement of the invariant mass of the J/Psi and the affirmation  
<sup>144</sup> of the quark model, all experiments start to look for better spatial resolutions in order to  
<sup>145</sup> achieve the possibility of reconstructing short lived particles and measuring their decays  
<sup>146</sup> length.

<sup>147</sup> Historically, the first pixel detector employed in particle physics was a CCD: it was  
<sup>148</sup> installed in the spectrometer at the CERN's Super Proton Synchrotron by the ACCMOR  
<sup>149</sup> Collaboration (Amsterdam, CERN, Cracow, Munich, Oxford, RAL) in the mid 1980s,  
<sup>150</sup> with the purpose of studying the (at the time) recently-discovered charmed particles.  
<sup>151</sup> The second famous usage of CCDs took place in the SLAC Large Detector at SLAC  
<sup>152</sup> linear collider in the years 1996-98, where the CCD technology was adopted instead of

153 the microstrip detectors for their excellent spatial resolution (cell size  $22 \times 22 \mu\text{m}^2$  giving  
154 a resolution of  $\sim 5 \mu\text{m}$ ) thanks to the sufficient time for readout between two successive  
155 collisions (160 ms).

156 From that period on, particle tracking in HEP experiments has been transformed  
157 radically. It became mandatory to build a inner vertex detector, with the following tasks:

- 158     • pattern recognition with the identification of particle tracks even in the presence of  
159       large backgrounds and pile-up
- 160     • measurement of vertices (primary and secondary)
- 161     • multi-track and vertex separation in the core of jets
- 162     • measurement of specific ionization
- 163     • momentum measurement combining with the information from other detectors

164     The more demanding requirements led to the development of hybrid pixel detectors  
165 satrting from 1990s: a dedicated collaboration, RD19, was established at CERN with the  
166 specific goal of defining a semiconductor micropattern detector with an incorporated signal  
167 processing at a microscopic level. In those years a wide set of prototypes of hybrid pixel has  
168 been manufactured; among the greatest productions a mention goes to the huge ATLAS  
169 and CMS vertex detectors. From the middle of 2013 a second collaboration, RD53, has  
170 been established with the new goal of finding a pixel detector suitable for the phase II in  
171 future upgrades of those experiments. Even if the collaboration is specifically focused on  
172 the design of hybrid pixel readout chips (aiming to 65 nm tecnique), also other options have  
173 been taken in account and many test have been done on MAPS. Requirements imposed by  
174 LHC are stringent and they will become even more with the increase of luminosity at HL-  
175 LHC: for example, a dose and radiation of 500 Mrad and  $10^{16} 1\text{MeV n}_{eq}/\text{cm}^2$  are exepcted  
176 after 5 years of operation. Time resolution, material budget and power consumption  
177 are also issues for the upgrade: to distinguish different events from different bunches a  
178 time resolution better than 25 ns for a bunch crossing frequency of 40 MHz is required, a  
179 material budget lower than  $2\% X_0$  and a power consunption lower than  $500 \text{mW/cm}^2$  are  
180 required.

181     Amidst the solutions proposed to improve radiation robustness of the sensor, 3D silicon  
182 detector, invented by Sherwood Parker in 1995, are very promising. In 3D sensors the  
183 electrode is a narrow column of n-type implanted vertically across the bulk instead of being  
184 implanted on the wafer's surface. The charge produced by the impinging particle is then  
185 drifted transversally within the pixel, and, as the mean path between two electrode can  
186 be souffcient low, the trap probability is not an issue. Even if 3D detector are adequately  
187 radiation hard and are a possible solution for hybrid pixel modules, especially in the  
188 innermost pixel detector layer, their fabrication process is currently low volume, making  
189 them unlikely to cover large areas. Another promising possibility is to use fast Monolitich  
190 Active Pixels systems which could allow the reduction of material budget and improve  
191 spatial resolution.

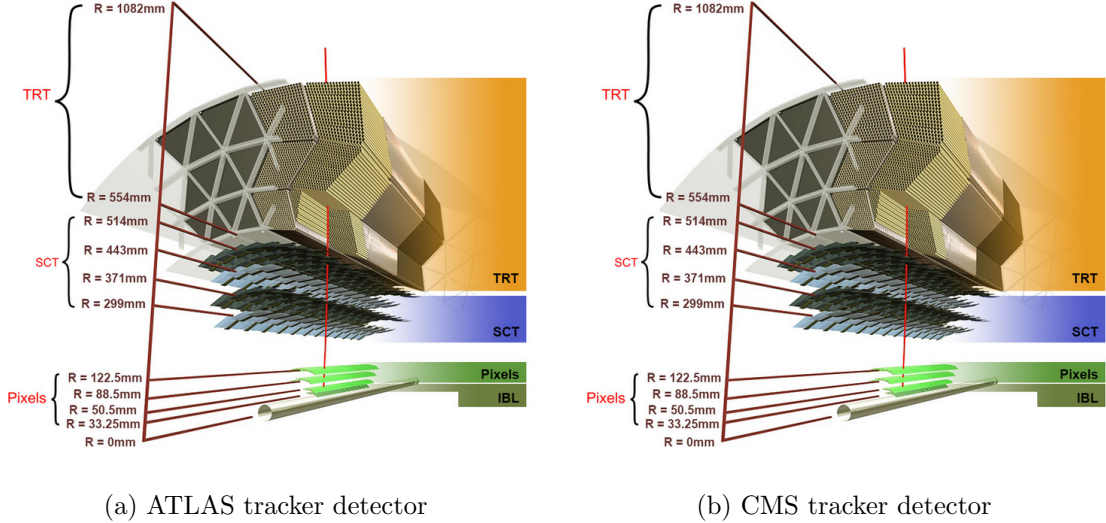


Figure 1.1: CMS

### 192 1.1.1 Hybrid Pixels at LHC

#### 193 ATLAS

194 ATLAS is one of two general-purpose detectors at the LHC and has the largest volume  
 195 detector ever constructed for a particle collider (46 m long and 25 m in diameter). The  
 196 Inner Detector (ID) consists of three different systems all immersed in a magnetic field  
 197 parallel to the beam axis whose main components are: the pixel, the micro-strips and  
 198 transition radiation trackers. Concerning the pixel detector, they installed a 3-layer hybrid  
 199 pixel detector in 2007 and an additional one inserted within the original detector envelope  
 200 and therefore called insertable B-layer (IBL) in 2014. 92 million pixels are divided in 4  
 201 barrel layers and 3 disks in each end-cap region, covering a total area of  $1.9 \text{ m}^2$  and having  
 202 a 15 kW of power consumption.

203 As stated by the ATLAS collaboration the pixel detector is exposed by an extreme  
 204 particle flux: "By the end of Run 3<sup>1</sup>, the number of particles that will have hit the  
 205 innermost pixel layers will be comparable to the number it would receive if it were placed  
 206 only a few kilometres from the Sun during a solar flare". Considering that the particle  
 207 density will increase even more with HL-LHC, radiation hardness is definitely a target  
 208 to achieve. Hybrid pixels will be used at the start of high-luminosity application, although  
 209 an active development of monolithic devices is ongoing for possible future use in the outer  
 210 pixel layers. The TJ-Monopix1 which I will describe in 3 is part of this development.

211 The sensor will be bonded with ITkPix, the first full-scale 65 nm hybrid pixel-readout  
 212 chip developed by the RD53 collaboration. Regarding the sensor, a valuable option is  
 213 using 3D pixels, which have already proved themselves in ATLAS, for the IBL, where they  
 214 were introduced in a limited acceptance range and introduced a new readout integrated  
 215 circuit called FE-I4. Also the complexity of the readout will be raised, as the number of  
 216 pixels will be increased of a factor about 7, passing from 92 millions to 6 billion.

---

<sup>1</sup>Run 3 start in June 2022

217 **CMS**

218 The CMS hybrid pixel detector has been upgraded in 2017, when, with the replacement  
219 of a piece of the beam pipe, a layer has been added to the detector at 3 cm from it.  
220 124 million pixels are divided between the barrel pixel detector (BPIX) and the forward  
221 disks (FPIX), with sensors which are different from each other and produced by different  
222 foundries. The sensors have an area equal to 100  $\mu\text{m}$  by 150  $\mu\text{m}$  and have been produced  
223 on 285  $\mu\text{m}$  to 300  $\mu\text{m}$  thick wafers.

224 The time resolution is 25 ns, and the information coming from the detector are stored on  
225 chip for the Level-1 trigger latency ( $\sim 4 \mu\text{s}$ ). The upgrade baseline ROIC was redesigned for  
226 the outer 3 layers, replacing analog signal readout with on-chip ADCs and digital readout  
227 at higher rate. reads out the pulse height information for each pixel.

228 **LHCb**

229 LHCb is a dedicated heavy-flavour physics experiment that exploits pp interactions at  
230 14 TeV at LHC. It was the last experiment to upgrade the vertex detector, the Vertex  
231 Locator (VELO), replacing the silicon-strip with 26 plane pixel detector (beacause of the  
232 fixed target geometry) in May 2022. As the instantaneous luminosity in Run3 is increased  
233 by a factor  $\lesssim 10$ , much of the readout electronics and of the trigger system have been  
234 developed in order to cope with the large interaction rate. To place the detector as close as  
235 possible to the beampipe and reach a better track reconstruction efficiency and resolution,  
236 the VELO has a surprising feature: during the injection of LHC protons it is parket at  
237 3 cm from the beams and only when the stability is reach it is moved at  $\sim 5$  mm. Readout  
238 speed is a priority for the detector that use a triggerless readout at 40 MHz collision rate,  
239 producing 20 Gbps per ROIC. The Velopix, which is the hybrid system designed for LHCb,  
240 is made bonding sensors, each measuring  $55 \times 55$  micrometers, 200  $\mu\text{m}$ -thick to a 200  $\mu\text{m}$ -  
241 thick ASIC specially developed for LHCb and coming from the Medipix family (sec. ??),  
242 which can handles hit rates up to 900 MHz per chip. Since the detector is operated under  
243 vacuum near the beam pipe, the heat removal is particularly difficult and evaporative CO<sub>2</sub>  
244 microchannel cooling are used.

245 **1.1.2 Monolithic Active Pixels**

246 MIMOSA [MIMOSA][MIMOSA26] (standing for Minimum Ionizing MOS Active pixel  
247 sensor), designed in 2008, prefigured the architecture of MAPS for coming vertex detector  
248 being the first large scale sensor to be employed as detector. MIMOSA-26 equiped the  
249 final version of EUDET high resolution beam telescope both at CERN-SPS and at DESY  
250 while the MIMOSA-28 devices are used for the first MAPS-based vertex detector at the  
251 STAR experiment at RHIC. MIMOSA-26 is fabricated in a 350 nm CMOS technology,  
252 and a module features 1152 columns, split into 18 indipendent groups, and 576 rows, with  
253 square pixels having a side of 18.4  $\mu\text{m}$  lenght; the epitaxyal layer is not fully depleted and  
254 the charge collection is mostly by diffusion, resulting in charge sharing between pixels and  
255 collection time bigger than 100 ns.

256 The chip is an Active Pixels (APS) and therefore it incorporates the amplification on  
257 pixel, while the signal discrimination and zero-suppression logic are placed at the End of  
258 Column: the readout is done in a rolling shutter mode with a frame integration time that  
259 can be lowered down to 85 ms, and a memory allowing to store up to six hits is.

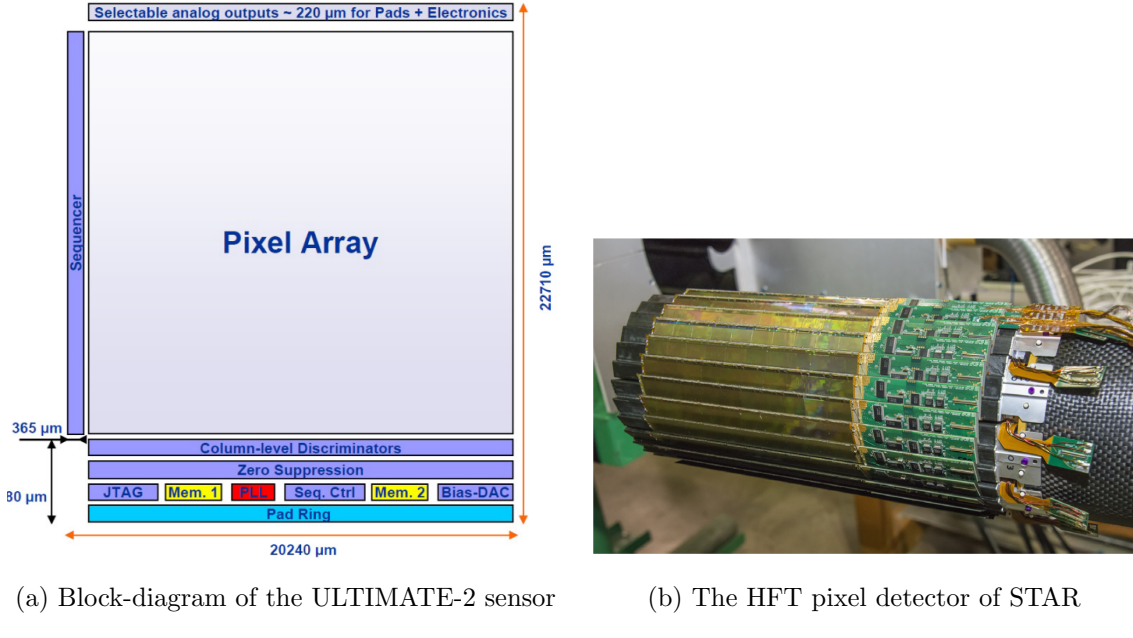
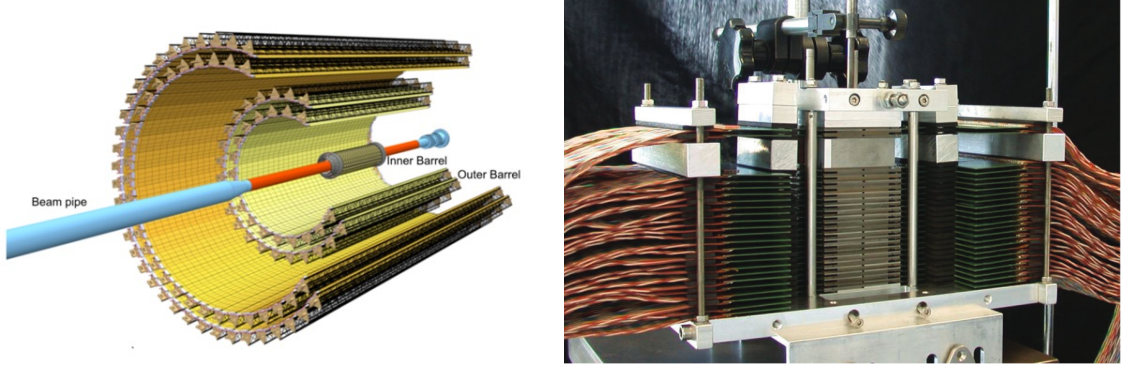


Figure 1.2

The EUDET telescope, equipped with six sensor planes, requires highly granular and thin pixel detectors in order to achieve an excellent track resolution (around 2 μm) even at the rather low particle energies of up to 6 GeV. The STAR experiment at the Relativistic Heavy Ion Collide (RHIC) accelerator at the Brookhaven National Laboratory (BNL) is the first to include MAPS in the vertex detector[**STAR**]. The main tracking detector in STAR is a TPC with radii 60-190 cm embedded in a 0.5 T solenoidal magnetic field, that provides a pointing resolution of approximately 1 mm. The pixel detector, PXL, is a part of a 3-detector system, Heavy Flavor Tracker (HFT), that has been added to the pre-existing STAR apparatus just before the 2014 Run in order to improve the impact parameter resolution and to enable the direct reconstruction of hadronic decays of heavy flavor mesons and baryons. The Heavy Flavor Tracker (HFT) is composed by the Silicon Strip Detector (SSD), the Intermediate Silicon Tracker (IST) and the Pixel Detector (PXL); the first one is placed at 22 cm from the beam pipe and consists of double sided strips with 95 μm inter-strip pitch, the second one, placed at 14 cm, is made of single sided silicon pads with 600 μm × 6 mm pitch and the last one made by two layers is placed at 2.8 cm and 8 cm fabricated with ULTIMATE2 (also known as MIMOSA-28), a successor of MIMOSA-26 sensor, with pitch 20.7 μm and thinned down to 50 μm. An area of 0.16 m<sup>2</sup> are covered by 400 MAPS sensor, corresponding to 356 millions of pixels divided into array size of 928 × 960. Each pixel includes circuitry for readout, amplification, and Correlated Double Sampling (CDS) for signal extraction and noise subtraction and the frame integration time is 185.6 μs; after the subtraction the signal to noise ratio is ∼ 30, with a noise between 10-12 electrons and a signal of 1000 e<sup>-</sup>. Thanks to the HFT system and the PXL, STAR achieved a track pointing resolution of 46 μm for 750 MeV/c kaons, and better than 30 μm for particle momenta bigger than 1 GeV/c: this performance enabled the study of D-meson production with a high significance signal.



(a) ALICE ITS scheme

(b)

Figure 1.3: FoCAL prototype fabricated with MAPS

## 285 ALPIDE at ALICE

286 The ALICE (A Large Ion Collider Experiment) tracking detector consists of the Inner  
 287 Tracking System (ITS), the gaseous Time Projection Chamber (TPC) and the Transition  
 288 Radiation Detector (TRD), all embedded in a magnetic field of 0.5 T. The ITS is made  
 289 by six layers of detectors, two for each type, from the interaction point outwards: Silicon  
 290 Pixel Detector (SPD), Silicon Drift Detector (SDD) and Silicon Strip Detector (SSD).  
 291 Contrary to the others LHC experiments, ALICE tracker is placed in a quite different  
 292 environments, which enables the usage of a MAPS-based detector: the expected dose  
 293 assorbed by the tracker is expected to be smaller by two order of magnitude and the rate  
 294 of interactions is few MHz instead of 40 MHz, even though the number of particles coming  
 295 out from each interaction is very high (the SPD is invested by a density of particles of  
 296  $\sim 100 \text{ cm}^{-2}$ ). The reconstruction of very complicated events with a large number of particle  
 297 is then a challenge, hence to segment and to minimize the amount of material, which may  
 298 cause secondary interaction futher complicating the event topology, is considered a viable  
 299 strategy.

300 ITS2, upgraded during the LHC long shut down in 2019-20, was the first large-area  
 301 ( $\sim 10 \text{ m}^2$  covered by 2.5 Gpixels) silicon vertex detector based on CMOS MAPS. The  
 302 detector employes the ALPIDE chip, developed by ALICE collaboration, fabricated in the  
 303 180 nm CMOS Imaging Sensor process of TowerJazz, whose design takes full advantage  
 304 of process feature which allows full circuitry within the pixel matrix. Thanks to the  
 305 reduction in the material budget, ITS2 obtained an amazing improvement both in the  
 306 position measurement and in the momentum resolution, especially improving the efficiency  
 307 of track reconstruction for particle with very low transverse momentum (by a factor 6 at  $p\text{T}$   
 308  $\sim 0.1 \text{ GeV}/c$ ). Further advancements in CMOS MAPS technology are being aggressively  
 309 pursued for the ALICE ITS3 vertex detector upgrades (foreseen around 2026-27), with  
 310 the goals of reducing the sensor thickness and improving the readout speed (which now is  
 311 completely asynchronous) of the devices, while keeping power consumption at a minimum.

312 Beside tracking, ALICE has been studing the possibility of exploiting the extreme  
 313 granularities of MAPS for calorimeter application. In a such calorimeter, the energy mea-  
 314 surement would come out from the counts of particles traversing the active layers, resulting  
 315 then in a digital calorimeter. A prototype forward calorimeter (FoCAL), fabricated with  
 316 the MIMOSA23 chips and containing 39 million pixels devided in 24 layers, alternated  
 317 with 24 layers of tungsten (1.3b), have been tested with electron beams and exhibited an

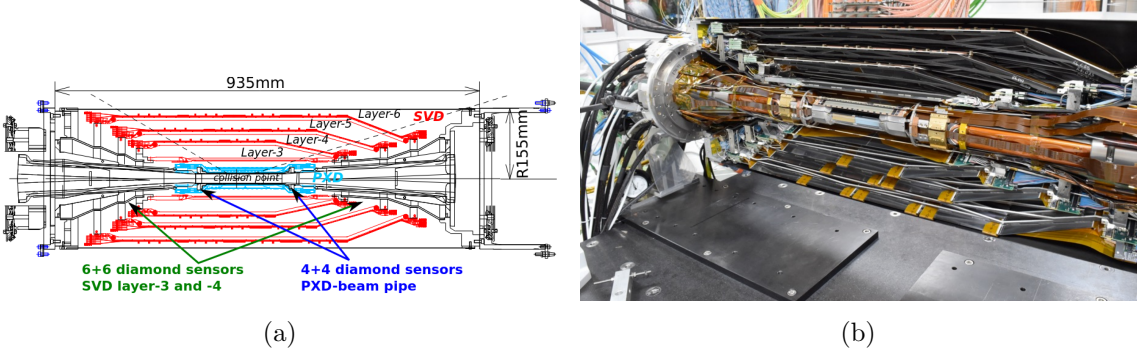


Figure 1.4: Belle2 vertex detector

318 energy resolution better than standard hadronic calorimeters, with a stochastic terms of  
 319  $30\%/\sqrt{E(GeV)}$ , a constant term of 2.8% and noise term of 0.063 GeV. Moreover, the  
 320 passive cooling via the tungsten structure has proven to be sufficient for the higher level of  
 321 heat produced by the chip with respect the conventional sensor while keeping the structure  
 322 compact.

### 323 **BelleII**

324 Due to the high background level coming from the nanobeam used at SuperKEKB in order  
 325 to achieve a such high luminosity ( $4.7 \times 10^{34} 1/cm^2/s$ ), silicon strip cannot be used in the in-  
 326 nner layer of the tracker. The occupancy is too high to allow the usage of strips up to 40 mm  
 327 from the beam pipe. Moreover for a precise reconstruction of B-decay vertices, the usage  
 328 of thin detector is mandatory at the low energy (4 GeV to 7 GeV) of the beam, in order to  
 329 minimize the multiple scattering of particles. The current vertex detector of BelleII, VXD,  
 330 is made of a pixel detector (PXD), fabricated with 2 layers of DEPFET-based pixels, and  
 331 4 layers of a double-sided silicon strip detectors (SVD)[**BelleII-DEPFET**]. Due to the  
 332 small capacitance of the collection node, DEPFET presents a high signal-to-noise ratio  
 333 (in 30-50) thanks to the low intrinsic noise and to the large signal achieved with the fully  
 334 depleted bulk: pixels are thinned to 75  $\mu m$  in the active region, then a MIP is supposed  
 335 to create a signal of  $\sim 6000 e^-$ , while the typical noise of DEPFET is around  $200 e^-$ . The  
 336 ASIC read out is still based on a rolling shutter logic, with an integration time of 20  $\mu s$ .  
 337 In order to reduce the data-storage memory PXD hits are only used to improve spatial  
 338 resolution of tracks: the SVD informations are used by the High Level Trigger (HLT) to  
 339 look for regions of interest in the pixel ladders just by extrapolating back the tracks found  
 340 in the tracker detector, and this method allows to store only data belonging to these areas;  
 341 the PXD hits are then used in offline track fit to improve the vertex resolution.

342 MAPS have been proposed for the replacement of VXD during the Long Shut Down  
 343 2 (LS2) foreseen around 2026-27; the new vertex detector, VTX, should be made of 5  
 344 layers fabricated with the optimized Belle II pixel sensor (OBELIX), a detector based on  
 345 TJ-Monopix (see at chapter 3). The main advantages VTX should bring are a significant  
 346 improvement in the track and vertex resolution (14  $\mu m$  before upgrade,  $\lesssim 10 \mu m$  expected  
 347 after upgrade), a reduction in the material budget, a higher background tolerance because  
 348 of the smaller sensor than strips dimension.

## 349 1.2 Other applications

350 Pixel detectors are widely used also for photon detection: they can be used as single photon  
351 counter or integrating and collecting the charge released by more impinging particles. The  
352 utilisation in the first case is similar to the tracking one, except that the requirements are  
353 less tight, so much that two noteworthy of microchips originally meant for detectors in  
354 particle physics at the LHC, and later employed in other fields are Medipix and Timepix.  
355 They are read-out chips developed by the Medipix Collaborations since early 1990s. For  
356 two decades, different Medipix generations have been produced, having a rough correlation  
357 with the feature size used: Medipix2 (1999) used 250 nm feature size CMOS while Medipix3  
358 (2005) 130 nm. For photons imaging other materials with higher atomic charge than silicon  
359 could be preferred, as a high photon absorption efficiency is needed: it was for this reason  
360 that Medipix2 was bump bonded to identically segmented sensors of both silicon and  
361 GaAs.

362 The applications in scientific imaging vary from astrophysics and medical imaging and  
363 dosimetry to more exotic domains as studies of protein dynamics, material science, art  
364 authentication and archaeology. One of the most important employment of Medipix is as  
365 X-ray single photon counting in industrial and medical radiography and in 3D computed  
366 tomography<sup>2</sup>. Thanks to a New-Zealand company, the MARS Bioimaging detector has  
367 been fabricated, which is capable of resolving the photons energy and produce 3D coloured  
368 images. Besides tracking in HEP (I have already cited the use of Timepix3 is in the beam  
369 telescope of the LHCb VELO), an important use of Timepix is in dosimetry. [Timepix](#)  
370 [Detector for Imaging in Ion Beam Radiotherapy- articolo e qualche info](#). A small-Timepix  
371 detector with the dimension of a USB can also be found at the International Space Station,  
372 where it is exploited for radiation, principally made of heavy-ion, monitoring.

### 373 1.2.1 Applicability to FLASH radiotherapy

374 A possible new application of pixels detector is dosimetry or beam monitoring of charged  
375 particles in high intensity radiography. Recently<sup>3</sup> a promising method for RT at ultra  
376 high dose rate (at least 40 Gy/s) and for this reason called FLASH-RT[FLASH review],  
377 instead of CONV-RT (0.03 Gy/s), came out. However, finding dosimeters suitable at ultra  
378 high dose rate is still an open issue since almost all standard online dosimeters have shown  
379 saturation problems.

### 380 Radiotherapy

381 The radiological treatment is a common method used in 60% of tumors both as palliative  
382 care and as treatment. It can be given before, after or during a surgery, (Intra-operative  
383 radiation therapy-IORT) and many different types of radiations (photons, electrons,  
384 protons and ions, which mainly are hydrogen and carbon) can be used to irradiate the  
385 affected tissues. Exploiting the ionizing energy loss, that can be parametrized by the  
386 Linear Energy Transfer (LET), a biological damage can be delivered to the tissue: while  $\alpha$   
387 and  $\beta$  particles are high LET radiations with values in 100 keV/ $\mu$ m to 200 keV/ $\mu$ m, x-rays

<sup>2</sup>The analysis of the direction dependence of X-ray absorption is performed, for example, in order to obtain an image in Computed Tomography (CT)

<sup>3</sup>The first evidences have been observed on mice experiments in 1966 and in 2014 by the group of Favaudon and Vozenin. After this, many tests on cats and pigs have been performed, and also there has been a clinical trial on a cutaneous tumor-patient

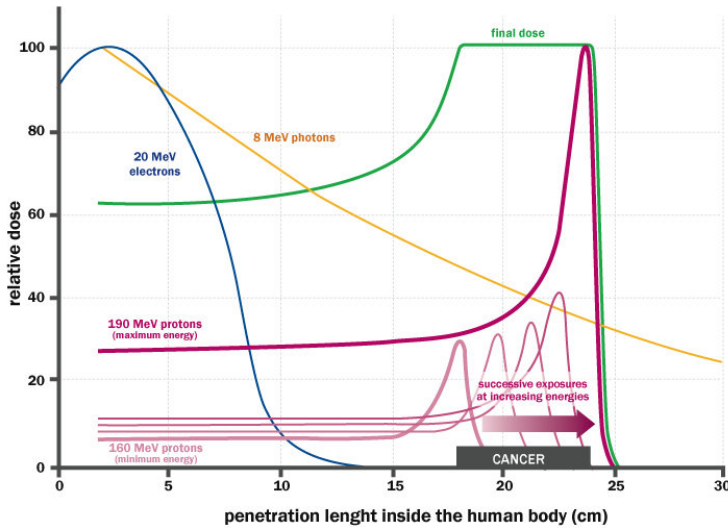


Figure 1.5: The Spread Out Bragg Peak (SOBP) curve (green), which is a constant dose distribution, is obtained from the superposition of many Bragg peak of hadrons with different energy.

	CONV-RT	FLASH-RT
Dose rate	0.03 Gy/s	40 Gy/s
Intra pulse dose rate	100 Gy/s	106 Gy/s
Treatment duration	~minutes	$\lesssim 500$ ms
Dose Per Pulse	0.3 mGy	1 Gy to 10 Gy
Pulse width	3 $\mu$ s	$\sim 2$ $\mu$ s

Table 1.1: Typical value of treatment parameters

and gamma-rays are low LET radiations with values in range  $0.2 \text{ keV}/\mu\text{m}$  to  $2 \text{ keV}/\mu\text{m}$ . If x-ray photons, with energy in 4 MeV to 25 MeV are used, the ionization is caused by the Compton electrons and is more in the superficial layers of the tissue due to the exponential attenuation of the beam. The hardrons energy loss, instead, is strongly localized in the last region of the track, that is the Bragg peak, such as the the treatment typically requires the scanning of the target. The Relative Biological Effectiveness (RBE) of ions near th Bragg peak depends on their mass, and in particular it increases with the ion's mass; even though, too heavy ions generally increases the damage produced also in the entrance region. Carbon is considered the optimum between the two trends.

Electrons, instead, of energy in range of a dozen of MeV tend to spread out on a bigger region of a few centimeters in both the diameter and thickness. Using Very High Energy Electrons (VHEE) has been taken into account for irradiation of deeper tissues, however, to date, the FLASH effect has been tested and demostrated only using low-energy electrons.

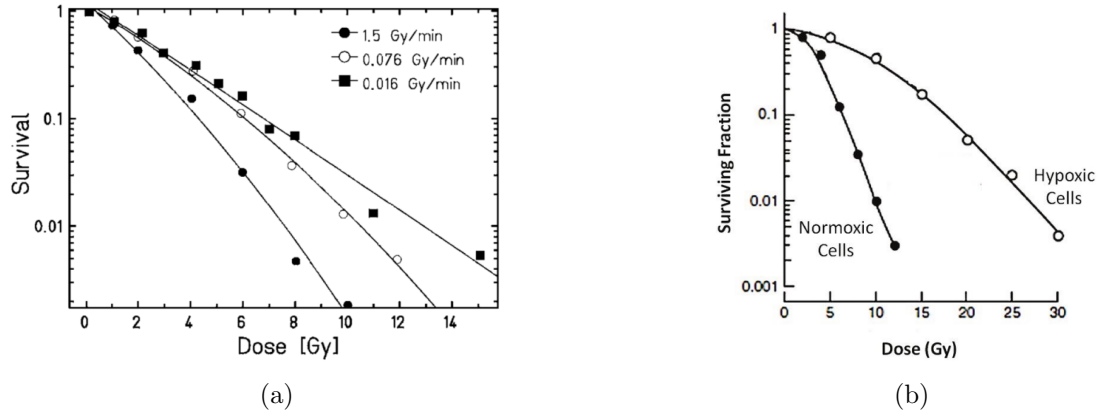


Figure 1.6: (a) Survival curve for different dose rate and (b) for different oxygen cell content

#### 402 FLASH effect

403 This treatment takes advantages of biological differences between tumors and healthy  
 404 tissues: it is characterized by reducing normal tissue toxicity and maintaining equivalent  
 405 tumor damage. The response to dose can be described by the survival fraction probability,  
 406 describing the fraction of surviving cell as a function of the dose:

$$S(D) = S(0) e^{-(\alpha D + \beta D^2)} \quad (1.1)$$

407 where  $\alpha$  and  $\beta$  respectively represents the rate of cell killing by single ionizing events and  
 408 by double hits. Hence, at high doses the density of damages increases and the cells repair  
 409 becomes more difficult. Even if the FLASH effect is not yet completely understood and  
 410 the underlying mechanisms are not clear, it looks like there are two different recipes which  
 411 are involved:

- 412 • **The dose rate:** higher dose rate produce bigger damages (fig. 1.6a) since this  
 413 prevent cells from sparing.
- 414 • **The presence or absence of oxygen:** while hypoxic cells are very resistant to radi-  
 415 ation, normal oxygenated cells are highly radiosensitive. This is because if molecules  
 416 containing  $O_2$  break due to the impinging radiation, then the oxygen can build Re-  
 417 active Oxygen Species (ROS) (fig.1.6b)

418 The Tumor Control Probability (TCP) and the Normal Tissue Complication (NTC)  
 419 functions parametrize respectively the efficiency of damaging on the tumor after having  
 420 released a certain dose and the probability of not affecting the healthy tissues. The  
 421 intermediate zone between the increase of the TC and of the NTC is called therapeutic  
 422 window, and the wider it is and the more effective the treatment is.

#### 423 Dosimetric problems

424 Up to now, all online dosimeters have shown saturation problems at high Dose Per Pulse,  
 425 differently from radiochromic films, which are the standard passive dosimeters and have  
 426 shown a dose-rate independece up to 100 Gy/s. In spite of the linear response in wide  
 427 dynamic range, they do not provide any online dosimetric informations, since the time

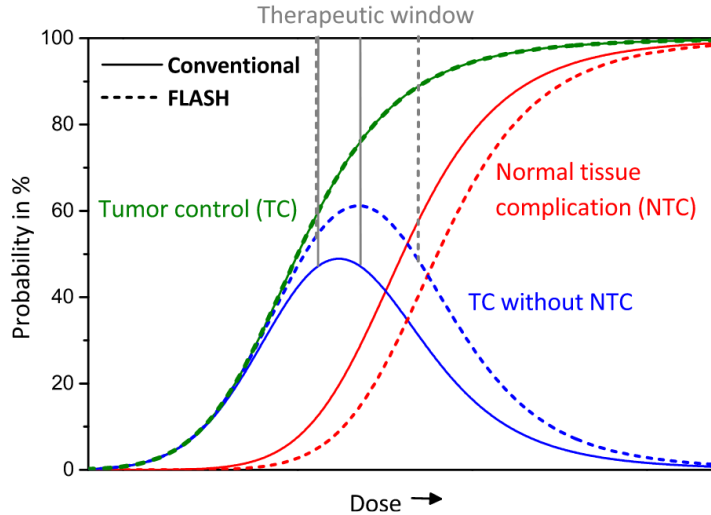


Figure 1.7: Illustration of dependence of TCP, NTCP and therapeutic window on dose, for CONV-RT ad FLASH-RT.

428 required to extract the physical value from the reading is not long, requiring a measurement  
429 of the film density<sup>4</sup>.

430 Ionization Chambers (ICs), which are the online reference dosimeter also according  
431 to law protocols, at high level of radiation (already at dose per pulse two orders of mag-  
432 nitude lower than the ones used for FLASH-RT) show both problems of saturation and  
433 recombination. When a high density of ions and electrons is produced in the gas, a high  
434 counter electric field opposed to the drift one might be generated; if a neutral region build  
435 up, both the recombination of i/e pairs, with a subsequent photoemission and abrupt dis-  
436 charge can happen. A correction factors,  $k_{sat}$ , can be introduced for sufficient low level of  
437 radiation and in this case a precise dose measurement can still be done: under conventional  
438 operation, with Dose Per Pulse lower than 1 mGy the correction factor is <5%.

439 Concerning the conventional semiconductor, if exposed to high dose rate, they suffer of  
440 saturation problems just as the ICs, but the development of fast MAPS devices, with rate  
441 capability of 100 MHz/cm<sup>2</sup> or more, might open the possibility of using these detectors as  
442 dosimeters at high dose rates. The idea is to use the high readout speed to split the dose  
443 per pulse in many buckets to reduce the saturation effect. Indeed a thin planar sensor  
444 could allow for the preservation of an enough strong electric field even at high dose rate  
445 which, together with the short mean path the e/h must cover to get the electrode (the  
446 epitaxial layer typically is ~30 μm), could result in a fast collection of electrons by drift  
447 and in a non-saturated response. Besides the thinness, also the small capacity typical of  
448 MAPS is beneficial for reducing the readout time: a reduced  $C_d$  enables for a fast discharge  
449 and then for a fast readout. Finally, MAPS devices would provide good time and space  
450 resolutions compared to other dosimeter technologies, and since they can be thinned down  
451 to about 50 μm, could also be employed in monitoring the beam position with minimal  
452 disturbance.

453 Among other detectors, optical fiber and alanine dosimeters have been proposed for  
454 high dose environments and many groups are going on studies on their applicability on  
455 FLASH-RT. In reference [FLASH dosimeters] are presented some results related with

---

<sup>4</sup>The radiation produces a polymerization of an active layer, resulting in a different density of coloration.

Commercial detector	Detector type	saturation [Gy/p]
PTW TW34045 Advanced Markus EC	ionization chamber	0.3
PTW TM60017 Dosimetry Diode E	silicon diode	0.15
PTW TW60019 microDiamond	diamond	0.15
DoseVue DoseWireTM Series 100	scintillator fiber	11-26

Table 1.2: Results obtain in [**FLASH** dosimeters]

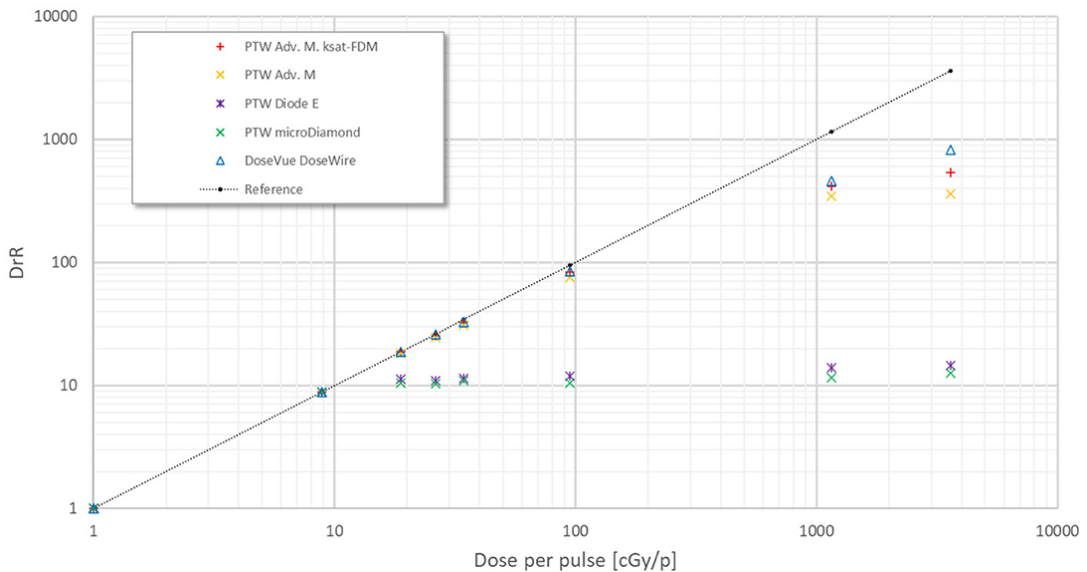


Figure 1.8: Saturation problems underlyed in [**FLASH** dosimeters].

saturation problems at high DDP of different types of detectors. The dosimeters tested and their value at which saturation becomes are reported in table 1.2, while in figure 1.8 are reported the measurements. The DrR is then defined as the ratio between the signal response of each dosimeters at a fixed DDP of 1 cGy/p and is called dosimeter reading ratio (DrR):

$$DrR = \frac{R}{R|_{Dp=1cGy/p}} = \frac{R}{R_{ref}} \quad (1.2)$$

Then, for a saturation not affected by saturation problems DrR should be a straight line with a slope equal to 1; since the reference measurements of dose has been performed with radiochromic films (GAFCHROMIC EBT-XD), whose dose independence has been tested<sup>5</sup> in range from 0 Gy to 15 Gy, the dotted black line in figure 1.8 represents the reference measurement done with it.

<sup>5</sup>The radiochromic films calibration has been obtained by irradiating the films with dose values in range from 0 Gy to 15 Gy, by positioning the films in a polymethylmethacrylate (PMMA) phantom at R<sub>100</sub> depth, corresponding to 10 cm

466 **Chapter 2**

467 **Pixel detectors**

468 Pixel detectors are semiconductor detectors which are segmented in two dimensions: this  
469 distinguishes them from the strip detectors, such that a single plane of detector already  
470 provides both the coordinates of impact of the detected particle. Their operation is based  
471 on the p-n junction (fig. 2.1). In an n-doped crystal some silicon atoms are replaced  
472 with valence 5 donor atoms (such as P) which provide loosely bound  $e^-$  carriers, while in  
473 p-doped crystals some atoms are replaced by valence 3 acceptor (such as B) which absorb  
474 existing free electrons, effectively creating a positively charged carrier called "hole".

475 A p-n junction is built by bringing in contact two n and p doped silicon crystals.  
476 At the boundary, recombination of opposite charge carriers occurs, forming a region, the  
477 depletion zone, which is free of charge carriers. The charged donors<sup>+</sup> and acceptor<sup>-</sup> atoms,  
478 that remain ionised in the n-type and p-type regions, constitute a space charge and create  
479 an electric field across the junction, causing a drift current in the opposite direction to  
480 the diffusion one, through which the junction reaches an equilibrium state. Assuming a  
481 constant space charge, the electric field is linear and reach a maximum at the boundary  
482 of the p and n layers.

483 **2.1 Signal formation**

484 When a charged particle passes through a semiconductor and loses energy by ionization,  
485 only a part of that energy is used to generate electron-hole pairs, since another part is used  
486 for other processes, as lattice excitation. The average energy needed to create a pair at  
487 300 K in silicon is  $w_i = 3.65 \text{ eV}$ , that is more than the mean ionization energy because of  
488 the interactions with phonons. For a minimum ionizing particle (MIP) the most probable  
489 value (MPV) of charge released in the semiconductor is  $0.28 \text{ keV}/\mu\text{m}$ , hence the number  
490 of electrons-hole pairs is:

$$\langle \frac{dE}{dx} \rangle \frac{1}{w_i} \sim 80 \frac{e/h}{\mu\text{m}} \sim \frac{1.28 \cdot 10^{-2} fC}{\mu\text{mm}} \quad (2.1)$$

491 Because of the splitting of the energy depositon between the two different processes, the  
492 number  $N_{e/h}$  of couples generated undergoes fluctuations that usually follow a Poisson  
493 distribution; thus the fluctuations of  $N_{e/h}$  is equal to  $\sigma_{e/h} = \sqrt{N_{e/h}}$ . Since the energy loss  
494 is not a purely statistical fact, because of the energy the particle can lose is obviously  $\leq E$   
495 and the energy need for ionization must be  $\geq$  of the mean ionization energy, the resolution  
496 actually is lower by a factor  $\sqrt{F}$ , where F is called the Fano factor. F is a function of the  
497 material and temperature and for silicon is equal to  $\sim 0.115$ .

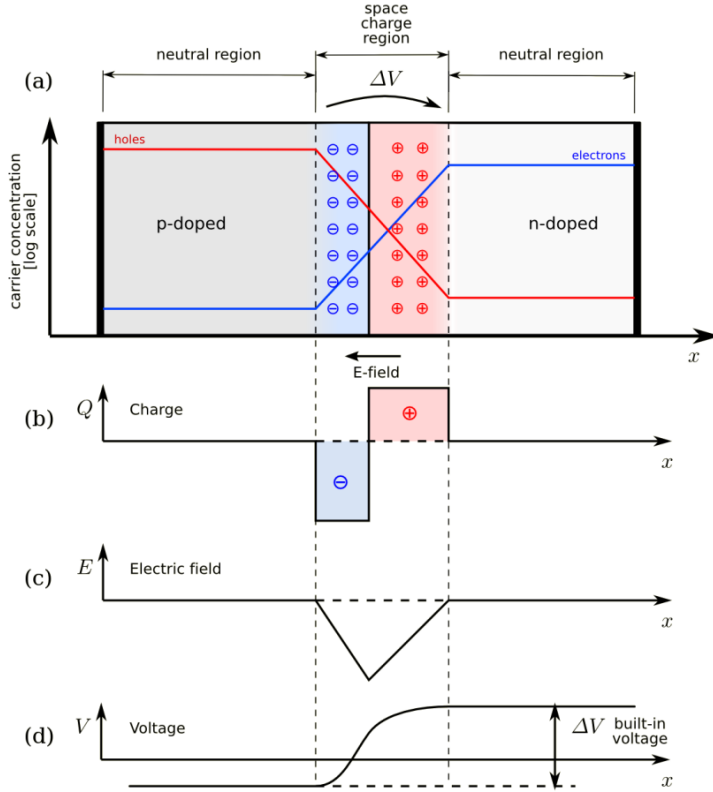


Figure 2.1: The structure of a p-n junction. (a) structure, (b) space charge density, (c) electric field distribution and (d) potential distribution.

498 In order to avoid a signal loss, pairs e/h must be produced in the depleted region of  
 499 the semiconductor, where the probability of recombination with charge carriers is low. For  
 500 this reason pixel detectors are commonly reverse biased: a positive bias is given to the  $n$   
 501 electrode and a negative to the  $p$  in order to increase the depletion zone. The width of  
 502 the depletion region depends on the external bias  $V_{ext}$ , the resistivity  $\rho$  and also with the  
 503 dopant:

$$d_n \sim 0.55 \sqrt{\frac{\rho}{\Omega cm}} \frac{V_{ext}}{V} \mu m \quad d_p \sim 0.32 \sqrt{\frac{\rho}{\Omega cm}} \frac{V_{ext}}{V} \mu m \quad (2.2)$$

504 Thus, high resistivity wafers ( $100 \Omega cm - k\Omega cm$ ) are typically preferred because they allow  
 505 a thicker depletion zone with smaller bias voltage.

506 The charges created within the sensor are separated by the electric field and collected  
 507 at their respective electrodes ( $p$  for holes and  $n$  for electrons)<sup>1</sup>. A signal  $i_e$  is generated on  
 508 the electrode  $e$  by the drift of these charges, as stated by the Shockley-Ramo's theorem:

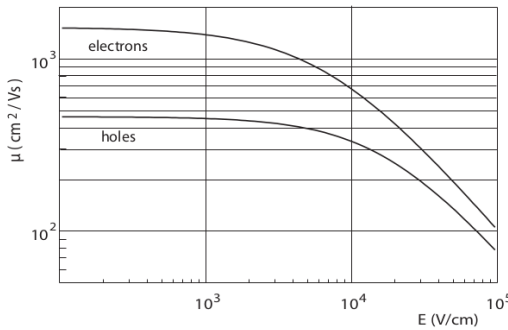
$$i_e(t) = -q v(t) E_{WF,e} \quad (2.3)$$

509 where  $v(t)$  is the instantaneous velocity of the charge  $q$  and  $E_{WF}$  is the weighting field,  
 510 that is the field obtained biasing the electrode  $e$  with 1V and all the others with 0V. The  
 511 drift velocity of the charge depends on the electric field and on the mobility of the particle:

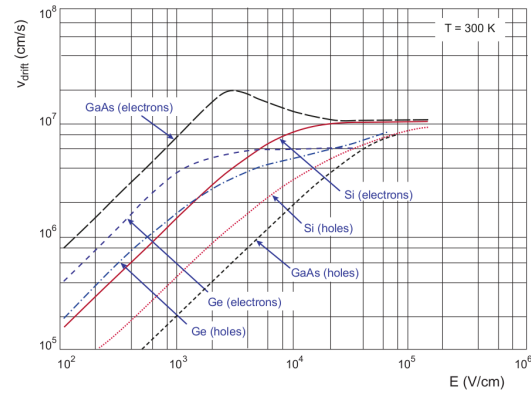
$$v = \mu(E) E \quad (2.4)$$

---

<sup>1</sup>Even if in principle both the electrode can be used to read the signal, for pixel detectors, where the number of channel and the complexity of readout are high, only one is actually used. In strip and pad detectors, instead, is more common a dual-side readout



(a) Dependence of the mobility on the electric field.



(b) Drift velocity at room temperature in different semiconductors

Figure 2.2

where  $\mu(E)$  is a function of the electric field and is linear in  $E$  only for small  $E$ : at higher values the probability of interactions with optical phonons increases, the mobility drops and this leads to a saturation of the velocity (fig. 2.2). Typical values for electrons and holes mobility in silicon at room temperature are  $\mu_n \sim 1450 \text{ cm}^2/\text{Vs}$ ,  $\mu_h = 500 \text{ cm}^2/\text{Vs}$ .

## 2.2 Charge Coupled Devices

Charge Coupled Devices are one of the first pixel detectors initially developed to detect visible light and then adapted for charged particles and x-rays. In CCDs the charge is created in a very thin active epitaxial layer (typically  $10 \mu\text{m}$ , maximally about  $30 \mu\text{m}$ ) and then locally stored in a potential minimum which is created by a MOS structure. The size of the CCD cells is typically in the range  $10 \mu\text{m}$  to  $20 \mu\text{m}$  such that spatial resolutions are of the order of a few micrometres. The collected charges are moved stepwise from electrode to electrode (thus so called 'bucket chain') by applying a potential with a clock with frequency of  $\sim \text{MHz}$ ; the readout chain is completely sequential and this makes the entire process comparatively slow (tens of ms), despite of such high frequency. A particular type of CCD, the pnCCDs, are typically used to detect low energy ( $< 10 \text{ keV}$ ) x-ray photons for their homogeneous spatial detection efficiency of photons. The pnCCDs have a sideward depletion similar to silicon drift chambers that makes the electric field stronger, compared with the normal CCDs. The pnCCDs designed for photon imaging are often fabricated with high Z materials, to increase absorption efficacy.

## 2.3 Hybrid pixels

In hybrid pixels, which currently are the state-of-art technology for large scale pixel detectors in most particle physics experiments, the sensors and the electronics are realized on separate wafers and connected together a bump of conductive material, typically In or Sn (fig. 2.3a). They provide a practical system where the sensor and the ASIC (application specific integrated circuit) can be optimized separately, allowing the fabrication of radiation-hard devices capable of operating at GHz rates. However hybrid pixels have also some disadvantages: the bump-bonding interconnect technology is expensive and delicate;

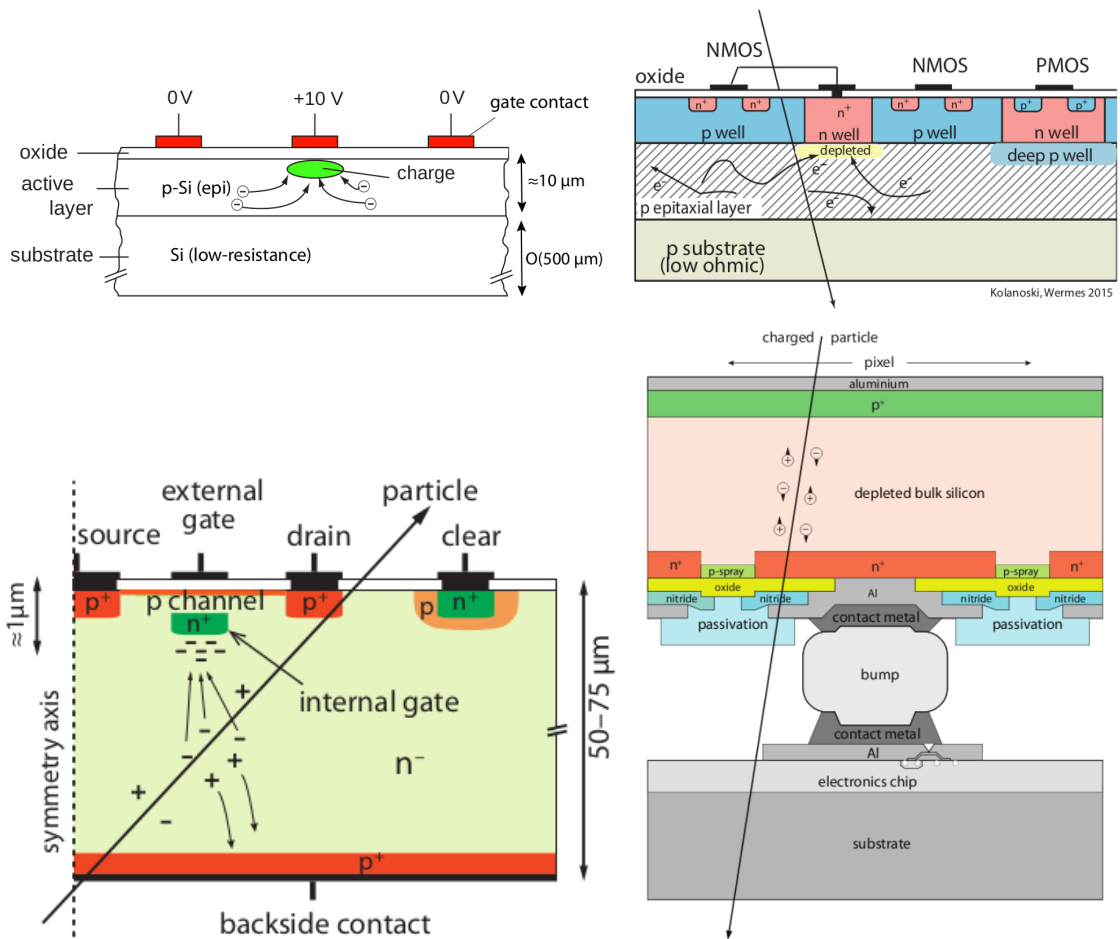


Figure 2.3: Concept cross-section of hybrid pixel (a) and of a DEPFET (b)

539 the separate substrates for electronics and sensor lead to an increase in the material bud-  
540 get; the pixel dimension must be long enough for the bump-bonding technology, with a  
541 current limit of about 50  $\mu\text{m}$ .

542 DEPFETs are the first attempt towards the integration of the front end (FE) on  
543 the same substrate of the sensor. Each pixel implements a MOSFET (metal-oxide-  
544 semiconductor field-effect transistor) transistor (a p-channel in fig. 2.3b): the hole current  
545 flows from source to drain is controlled by the external gate and the internal gate together.  
546 The internal gate is made by a deep  $n+$  implant towards which electrons drift after being  
547 created in the depletion region; the accumulation of electrons in the region underneath  
548 the  $n$  implant changes the gate potential and controls the transistor current, resulting in  
549 an internal amplification, the removal of the signal charge from the internal gate is called  
550 "Clear". DEPFET typically have a good S/N ratio: thanks to the on-pixel amplification,  
551 to the thick depletion region. As in CCDs, DEPFET require a serial readout of the pixel  
552 signal, and are therefore relatively slow devices, but they can be made very think (50  $\mu\text{m}$ ).  
553 In recent years, the sensor development was driven by an intensive R&D and prototyping  
554 for x-ray imagers and the ILC vertex detector.

## 555 2.4 CMOS MAPS and DMAPS

556 Monolithic active pixels accommodate on the same wafer both the sensor and the FE  
557 electronics, with the second one implanted on top within a depth of about 1  $\mu\text{m}$  below  
558 the surface. MAPS have been first proposed and realized in the 1990s and their practical  
559 usage has been enabled by the development of the consumer electronics sector, which  
560 guarantees the halving of CMOS transistors dimension at least every two years, as stated  
561 by the Moore's law. As a matter of fact the dimension of components, their organization  
562 on the pixel area and logic density are important issues for the design and for the layout.  
563 Compared to CCDs, the readout time is dramatically reduced by the in-pixel amplification  
564 and discrimination, typically followed by a sparsified readout selecting only over threshold  
565 pixels and avoiding the need for signal transporation over thousands of pixels.

566 A critical parameter for accelerator experiments is the material budget, which repre-  
567 sents the main limit factor for momentum measurement resolution in a magnetic field;  
568 since hybrid pixels are thicker ( $\sim$  hundreds of  $\mu\text{m}$ ) than monolithic ones (even less than  
569 100  $\mu\text{m}$ ). Using the latter the material budget can be reduced to a third: typical values  
570 for hybrid pixels is 1.5 %  $X_0$  per layer, while for monolithic 0.5 %  $X_0$ . Compared to  
571 MAPS, among other disadvantages of hybrid pixels there is the bigger power consump-  
572 tion, that requires also a bigger cooling system, leading to a futher increase of material.  
573 On the other hand MAPS are still in the development phase, and although they have been  
574 used in several experiments as discussed in chapter 1, their potential remains to be fully  
575 exploited.

576 Monolithic active pixel can be distinguished between two main categories: MAPS and  
577 depleted MAPS (DMAPS). In the initial CMOS MAPS (4.25b) an unmodified CMOS  
578 process was used that presented the full depletion of the 1  $\mu\text{m}$  to 20  $\mu\text{m}$  epitaxial layer.

579 The charge is mainly collected by diffusion rather than by drift, making the path of  
580 created charges in the bulk longer resulting in relatively slow collection (of order of 100 ns).  
581 Moreover, the collection can be partial, especially after irradiation of the detector, when  
582 the trapping probability becomes higher. In DMAPS instead, a modified process is em-  
583 ployed allowing the creation of a much thiker depletion layer, thus increasing significantly

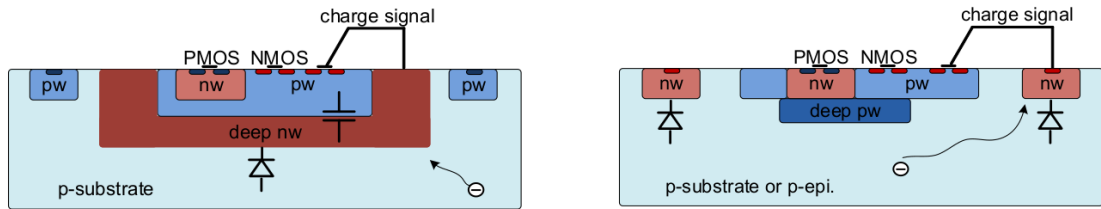


Figure 2.4: Concept cross-section with large and small fill factor

584 the collected charges. This requires the addition deep implanted areas, as shown in figure  
 585 4.25b. The charge released in the epi layer is very small (few thousands of electrons) but  
 586 the extremely small electrode capacitance allows the formation of a detectable voltage  
 587 signal  $V=Q/C$ .

588 In figure ?? it is shown as example of CMOS MAPS: the sensor implements an n well  
 589 as collection diode; to prevent the others n wells (which contain PMOS transistor) of the  
 590 electronic circuit competing in charge collection and to shield the CMOS circuit from the  
 591 substrate, additional underlying deep p well are needed.

#### 592 2.4.1 DMAPS: large and small fill factor

593 There are two different sensor-design approaches (figure 2.4) to DMAPS:

- 594 • large fill factor: a large collection electrode that is a large deep n-well and that host  
 595 the embedded electronics
- 596 • small fill factor: a small n-well is used as charge collection node

597 To implement a uniform and stronger electric field, DMAPS often uses large electrode  
 598 design that requires multiple wells (typically four including deep n and p wells); with this  
 599 layout the total capacity of the sensor increases because of the addition of a new term  
 600 (fig. 2.5), which contributes to the total amplifier input capacity ( $\sim 100 \text{ fF}$ ). In addition  
 601 to the capacity between pixels ( $C_{pp}$ ) and between the pixel and the backside ( $C_b$ ), a non-  
 602 negligible contribution comes from the capacities between wells ( $C_{SW}$  and  $C_{WW}$ ) needed  
 603 to shield the embedded electronics. These capacities affect the thermal and  $1/f$  noise of  
 604 the charge amplifier and the  $\tau_{CSA}$  too:

$$605 ENC_{thermal}^2 \propto \frac{4}{3} \frac{kT}{g_m} \frac{C_D^2}{\tau_{sh}} \quad \tau_{CSA} \propto \frac{1}{g_m} \frac{C_D}{C_f} \quad (2.5)$$

606 where  $g_m$  is the transconductance,  $\tau_{sh}$  is the shaping time. Among the disadvantages coming  
 607 from this large input capacity there is a coupling between the sensor and the electronics  
 608 resulting in cross talk noise on neighbouring electrodes; indeed, since digital switching in  
 609 the FE electronics does a lot of oscillations, this problem is especially connected with the  
 610 intra wells capacities. So, larger charge collection electrode sensors provide a uniform electric  
 611 field in the bulk that results in short drift path and so in good collection properties,  
 612 especially after irradiation, when trapping probability can become an issue.

613 The small fill-factor variant, instead, benefits from a small capacity (5 fF to 20 fF), but  
 614 suffers from a non uniform electric field and from all the issue related to that (slowness  
 615 and high trapping probability). As we'll see these two different types of sensor require  
 616 different amplifier: the large electrode one is coupled with a charge sensitive amplifier,  
 617 while the small one with a voltage amplifier (sec 2.5.1).

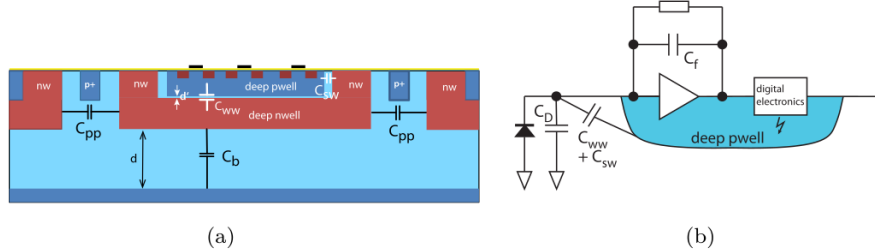


Figure 2.5:  $C_{pp}$ ,  $C_b$ ,  $C_{WW}$ ,  $C_{SW}$

	small fill factor	large fill factor
small sensor C	✓ (< 5 fF)	✗ (~ 100 200 fF)
low noise	✓	✗
low cross talk	✓	✗
velocity performances	✓	✗ (~100 ns)
short drift paths	✗	✓
radiation hard	✗	✓

Table 2.1: Small and large fill factor DMAPS characteristics

#### 617 2.4.2 A modified sensor

618 A process modification, developed by CERN in collaboration with the foundries, which  
 619 has become the standard solution to combine the characteristics of a small fill factor sensor  
 620 (small input amplifier capacity) and of a large fill factor sensor (uniform electric field), is  
 621 the one carried out for the ALICE upgrade for about ten years [AProcessModification].  
 622 A compromise between the two sensors could also be making smaller pixels, but this  
 623 solution requires reducing the electronic circuit area, so a completely new pixel layout  
 624 should be though. The modification consists in inserting a low dose implant under the  
 625 electrode and one of its advantage lies in its versatility: in fact, both standard and modified  
 626 sensor are often produced for testing.

627 Before the process modification, the depletion region extends below the diode towards  
 628 the substrate, and it does not extend much laterally, even if a high bias is applied to the  
 629 sensor (fig. 2.6). After the modification, two distinct pn junctions are built: one between  
 630 the deep p well and the n<sup>-</sup> layer, and the other between the n<sup>-</sup> and the p<sup>-</sup> epitaxial  
 631 layer, extending to the whole area of the sensor. Since deep p well and the p-substrate are  
 632 separated by the depletion region, the two p electrodes can be biased separately and this  
 633 is beneficial to enhance the vertical electric field component. The doping concentration is  
 634 an optimization parameter: it must be high enough to be larger than that in the epitaxial  
 635 layer to prevent the punchthrough between p-well and the substrate, but it must also be  
 636 low enough to allow the depletion for reasonable bias values.

#### 637 2.5 Analog front end

638 After the collection on the electrode, the signal enters the front end amplification circuit  
 639 (fig.2.7), ready to be shaped and transmitted out of chip. Low noise amplification, fast hit  
 640 discrimination and an efficient, high-speed readout architecture, consuming as low power

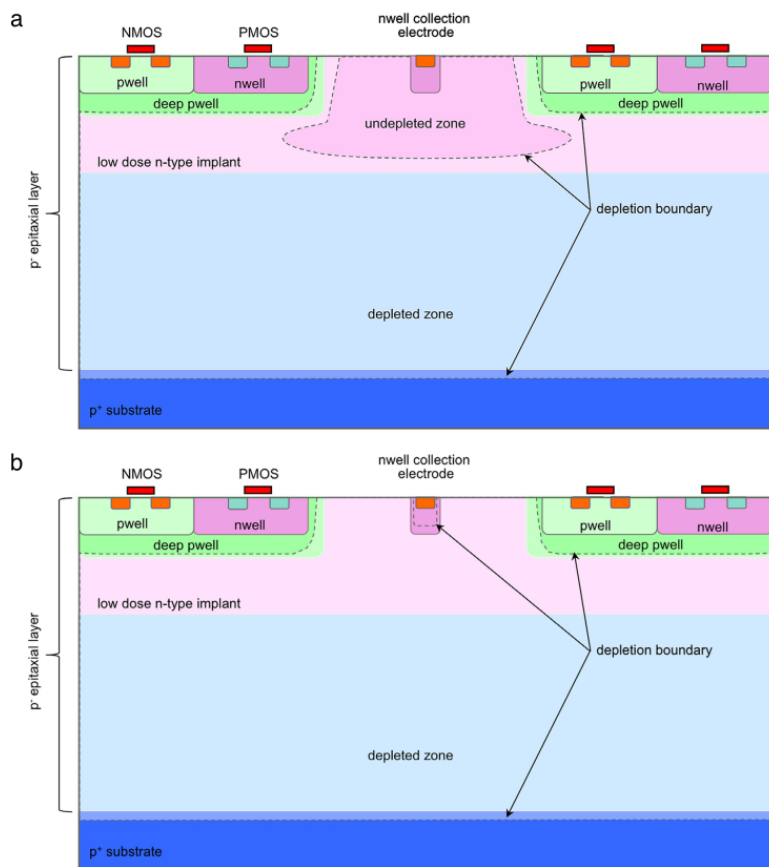


Figure 2.6: A modified process for ALICE tracker detector: a low dose n implant is used to create a planar junction. In (a) the depletion is partial, while in (b) the pixel is fully depleted.

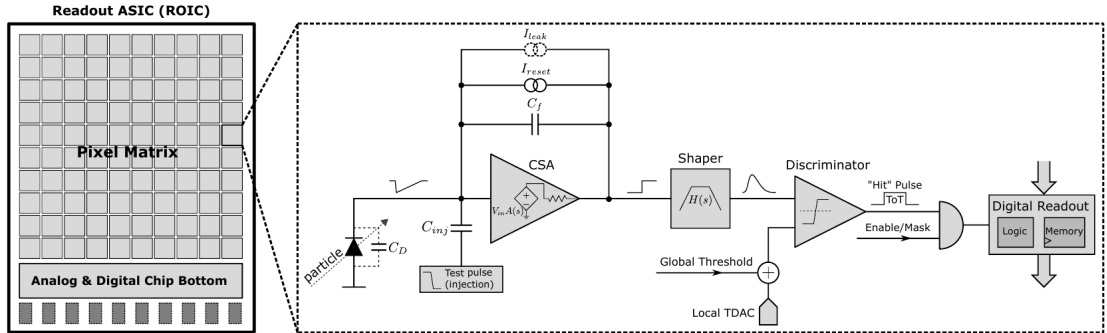


Figure 2.7: Readout FE scheme: in this example the preamplifier is a charge sensitive one (CSA) but changing the capacitive feedback into a resistive one, this can be converted in a voltage or current amplifier.

as possible, are the goal of the readout integrated electronics (ROIC). The main parts of the analog front end chain are a preamplifier (that often is the only amplification stage) with a reset to the baseline mechanism and a leakage current compensation, a shaper (a band-pass filter) and finally a discriminator. The whole chain must be optimized and tuned to improve the S/N ratio. It is very important both not to have a large noise before the amplification stage to avoid amplifying that noise, and to choose a reasonable threshold of the discriminator to cut noise-hits much as possible.

### 2.5.1 Preamplifier

The a preamplifier can be designed as an operational amplifier (OpAmp) where the gain is determined by the input and feedback impedance (first step in figure 2.7):

$$G = \frac{v_{out}}{v_{in}} = \frac{Z_f}{Z_{in}} \quad (2.6)$$

Depending on if a capacity or a resistance is used as feedback, respectively a charge or a voltage amplifier is used: if the voltage input signal is large enough and has a sharp rise time, the voltage sensitive preamplifier is preferred. Consequently, this flavor does not suit to large fill factor MAPS whose signal is small:  $v_{in} = Q/C_D \approx 3 \text{ fC}/100 \text{ pF} = 0.03 \text{ mV}$ , but it's fine for the small fill factor ones:  $v_{in} = Q/C_D \approx 3 \text{ fC}/3 \text{ pF} = 1 \text{ mV}$ .

In the case of a resistor feedback, if the signal duration is longer than the discharge time ( $\tau = R_S C_D$ ) of the detector the system works as current amplifier, as the signal is immediately trasmitted to the amplifier; in the complementary case (signal duration longer than the discharge time) the system integrates the current on the  $C_D$  and operates as a voltage amplifier.

## 2.6 Readout logic

The readout logic includes the part of the circuit which takes the FE output signal, processes it and then transmit it out of pixel and/or out of chip; depending on the situation of usage different readout characteristics must be provided. To store the analogical information (i.e. charge collected, evolution of signal in time, ...) big buffers and a large bandwidth are needed; the problem that doesn't occur, or better occur only with really

667 high rate, if one wants record only digital data (if one pixel is hit 1 is recorded, and if not  
 668 0 is recorded).

669 A common compromise is to store the time over threshold (ToT) of the pulse in clock  
 670 cycle counts; this needs of relatively coarse requirement as the ToT can be trimmed down  
 671 to use only a dozen bits but, being correlated with the deposited charge, it provides a  
 672 sufficient information. The ToT digitalization usually takes advantage of the distribution  
 673 of a clock (namely BCID, bunch crossing identification) on the pixels' matrix. The required  
 674 timing precision is better than  $\sim 25$  ns, that corresponds to the period between bunch  
 675 collisions at LHC; for such reason a reasonable BCID-clock frequency for pixels detector  
 is 40 MHz.

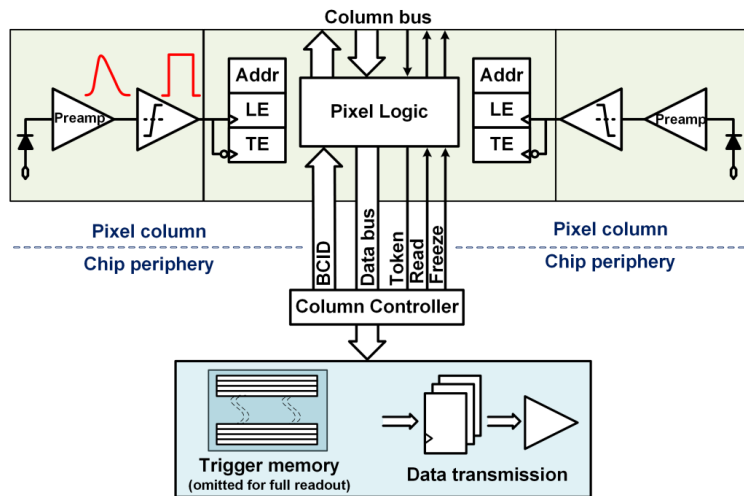


Figure 2.8: Column drain R/O scheme where ToT is saved

676  
 677 Moreover, the readout architecture can be full, if every hit is read, or triggered, if  
 678 a trigger system decides if the hit must be stored or not. On one hand the triggered-  
 679 readout needs buffers and storage memories, hand the full readout, because there is no  
 680 need to store hit data on chip, needs an high enough bandwidth. A triggered readout is  
 681 fundamental in accelerator experiments where the quantity of data to store is very large  
 682 and some selection has to be applied by the trigger: to give an order of magnitude, at LHC  
 683 more than 100 TBit/s of data are produced, but the storage limit is about 100 MBit/s  
 684 [**K-Wermes**](pag. 797). Typically, the trigger signal is processed in a few  $\mu s$ , so the pixel  
 685 gets it only after a hundred clock cycles from the hit arrival time: the buffer depth must  
 686 be able to handle such high trigger latency.

687 After having taken out the data from the pixel, it has to be transmitted to the end of  
 688 column (EoC) where a serializer delivers it out of chip, typically to an FPGA. There are  
 689 several ways of transmitting data from a pixel to the EoC: a common one is the column-  
 690 drain read out, developed for CMS and ATLAS experiments [**column-drain**]. All the  
 691 pixels in a double-column share a data bus and only one pixel at a time, according to a  
 692 priority chain, can be read. The reading order circuit is implemented by shift register (SR):  
 693 when a hit arrives, the corresponding data, which can be made of timestamp and ToT,  
 694 is temporarily stored on a RAM until the SR allows the access to memory by data bus.  
 695 Even if many readout architectures are based on the column-drain one, it does not work  
 696 for large size matrices. The problem is the increasing number of pixels on a column would  
 697 also raise the number of pixels in the priority chain, which would result in a slowdown of

698 the readout.

699 If there isn't any storage memory, the double-column behaves as a single server queue  
700 and the probability for a pixel of waiting a time  $T$  greater than  $t$ , with an input hit rate  
701 on the column  $\mu$  and an output bandwidth  $B_W$  is [Garcia-Review]:

$$P(T > t) = \frac{\mu}{B_W} e^{-(B_W - \mu)t} \quad (2.7)$$

702 To avoid hit loss (let's neglect the contribution to the inefficiency of the dead time  $\tau$  due to  
703 the analog Front End), for example imposing  $P_T > t \sim 0.001$ , one obtains  $(B_W - \mu)t_t \sim 6$ ,  
704 where  $t_t$  is the time needed to transfer the hit; since  $t_t$  is small, one must have  $B_W \gg \mu$ ,  
705 that means a high bandwidth [Garcia-Review].

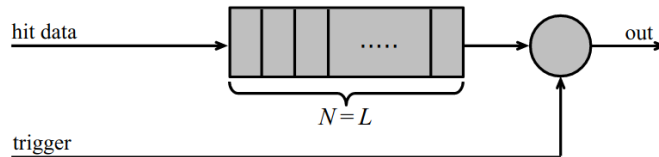


Figure 2.9: Block diagram of a pipeline buffer:  $N$  is the dimension of memory buffer and  $L$  is the trigger latency expressed in BCID cycles

705 Eq.2.7 is actually an approximation, since each pixel sees a different bandwidth de-  
706 pending on the position on the queue: the first one sees the full bandwidth, while the next  
707 sees a smaller one because it can be occasionally blocked by the previous pixel. Then,  
708 the bandwidth seen by the pixel  $i$  is  $B_i = B - \sum_j \mu_j$ , where  $\mu_j$  is the hit rate of the  $j$ th  
709 pixel. The efficiency requirement on the bandwidth and the hit rate becomes:  $B_{W,i} > \mu_i$ ,  
710 where the index  $i$  means that the constraint is for a single pixel; if all the  $N$  pixels on a  
711 column have the same rate  $\mu = N\mu_i$ , the condition reduces to  $B_W > \mu$ . The bandwidth  
712 must be chosen such that the mean time between hits of the last pixel in the readout chain  
713 is bigger than that. In order to reduce the bandwidth, a readout with zero suppression  
714 on pixel is typically employed; this means that only information from channels where the  
715 signal exceeds the discriminator threshold are stored.

717 If, instead, the signal is locally stored until a trigger signal arrives, the input rate to  
718 column bus  $\mu'$  is reduced compared to the hit rate  $\mu$  as:  $\mu' = \mu \times r \times t$ , where  $r$  is the  
719 trigger rate and  $t$  is the bunch crossing period. In this situation there is a more relaxed  
720 constraint on the bandwidth, but the limiting factor is the buffer depth: the amount of  
721 memory designed depends both on the expected rate  $\mu$  and on the trigger latency  $t$  as  
722  $\propto \mu \times t$ , which means that the higher the trigger latency the lower the hit rate to cope  
723 with.

724 In order to have an efficient usage of memory on pixels' area it's convenient grouping  
725 pixels into regions with shared storage. Let's compare two different situations: in the first  
726 one a buffer is located on each pixel area, while in the second one a core of four pixels  
727 share a common buffer (this architecture is commonly called FE-I4).

728 Consider a 50 kHz single pixel hits rate and a trigger latency of 5  $\mu s$ , the probability of  
729 losing hits is:

$$P(N > 1|\nu) = 1 - P(N = 0|\nu) - P(N = 1|\nu) = 1 - e^{-\nu}(1 + \nu) \approx 2.6\% \quad (2.8)$$

730 where I have assumed a Poissonian distribution with mean  $\nu = 0.25$  to describe the counts  
731  $N$ .

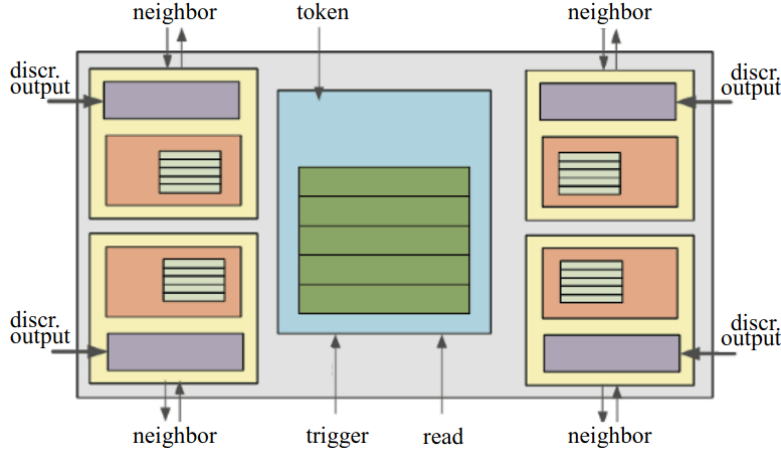


Figure 2.10: Block diagram of the FE-I4 R/O. Read and memory management section is highlighted in light blue; latency counters and trigger management section are highlighted in green; hit processing blocks are highlighted in purple; ToT counters and ToT management units are highlighted in orange

<sup>732</sup> To get an efficiency  $\epsilon$  greater than 99.9 % a 3 hit depth buffer is needed:

$$P(N > 3|\nu) = 1 - \sum_{i=0}^3 P(N = i|\nu) < 0.1\% \quad (2.9)$$

<sup>733</sup> Consider the second situation: if the average single pixel rate is still 50 kHz, grouping four  
<sup>734</sup> pixels the mean number of hits per trigger latency is  $\nu = 0.25 \times 4 = 1$ . To get an efficiency  
<sup>735</sup> of 99.9% (eq. 2.9) a buffer depth of 5 hits in the four-pixels region, instead of 3 per pixels,  
<sup>736</sup> is needed.

737

# Chapter 3

738

## MAPS devices description

739 This chapter presents a brief description of the two DMAPS devices that I have tested  
740 during the thesis work: the TJ-Monopix1 device, originating developments connected to  
741 the ATLAS upgrade, and the ARCADIA Main Demonstrator device, developed by INFN  
742 ARCADIA collaboration as a multipurpose chip for accelerator and space applications.

743

### 3.1 TJ-Monopix1

744 TJ-Monopix1 is a small electrode DMAPS with fast R/O capability, fabricated by Tower-  
745 Jazz foundry in 180 nm CMOS imaging process. It is part, together with prototypes from  
746 other series such as TJ-MALTA, of the ongoing R&D efforts aimed at developing DMAPS  
747 in commercial CMOS processes, that could cope with the requirements at accelerator ex-  
748 periments. Both TJ-Monopix and TJ-MALTA series [**MALTA**], produced with the same  
749 technology by TowerJazz (the timeline of the foundry products is shown in figure 3.1), are  
750 small electrode demonstrators and principally differ in the readout design: while Monopix  
751 implements a column-drain R/O, an asynchronous R/O without any distribution of BCID  
752 has been used by TJ-Malta in order to reduce power consumption.



Figure 3.1: Timeline in TowerJazz productions in 180 nm CMOS imaging process

753 Another Monopix series, but in 150 nm CMOS technology, has been produced by  
754 LFoundry [**LF-Monopix**]. The main differences between the LF-Monopix1 and the  
755 TJ-Monopix1 (summarized in table 3.2), lay in the sensor rather than in the readout  
756 architecture, as both chips implements a fast column drain R/O with ToT capability  
757 [**LF-TJ-Monopix-short**][**LF-TJ-Monopix-long**]. Concerning the sensors, either are  
758 based on a p-type substrate, but with slightly different resistivities; in addition LFoundry

	LF-Monopix1	TJ-Monopix1
Resistivity	$>2 \text{ k}\Omega\text{cm}$	$>1 \text{ k}\Omega\text{cm}$
Pixel size	$50 \times 250 \mu\text{m}^2$	$36 \times 40 \mu\text{m}^2$
Depth	$100\text{-}750 \mu\text{m}$	$25 \mu\text{m}$
Capacity	$\sim 400 \text{ fF}$	$\sim 3 \text{ fF}$
Preamplifier	charge	voltage
Threshold trimming	on pixel (4-bit DAC)	global threshold
ToT	8 bits	6 bits
Consumption	$\sim 300 \text{ mW/cm}^2$	$\sim 120 \text{ mW/cm}^2$
Threshold	$1500 e^-$	$\sim 270 e^-$
ENC	$100 e^-$	$\sim 9 e^-$

Table 3.1: Main characteristics of Monopix1 produced by TowerJazz and LFoundry  
**[LF-TJ-Monopix-short]****[LF-TJ-Monopix-long]**

759 pixels are larger, thicker and have a large fill factor (the very deep n-well covers  $\sim 55\%$  of  
760 the pixel area). The primary consequence is that LF-Monopix1 pixels have a higher ca-  
761 pacity resulting in higher consumption and noise. As I discussed in section 2.4.1, the fact  
762 that LF-Monopix has a large fill factor electrode is expected to improve its radiation hard-  
763 ness. Indeed, a comparison of the perfomance of the two chips showed that TJ-Monopix  
764 suffers a comparatively larger degradation of efficiency after irradiation, due to the low  
765 electric field in the pixel corner; on the other hand, a drawback of the large fill factor in  
766 LF-Monopix is a significant cross-talk.

767 The TJ-Monopix1 chip contains, apart from the pixels matrix, all the required support  
768 blocks used for configuration and testing:

- 769 • the whole matrix contains  $224 \times 448$  pixels, yielding a total active area approximately  
770 equal to  $145 \text{ mm}^2$  over a total area of  $1 \times 2 \text{ cm}^2$ ;
- 771 • at the chip periphery are placed some 7-bit Digital to Analog Converter (DAC), used  
772 to generate the analog bias voltage and current levels and to configure the FE;
- 773 • at the EoC is placed a serializer to transferred datas immediately, indeed no trigger  
774 memory is implemented in this prototypes;
- 775 • the matrix power pads are distributed at the sides
- 776 • four pixels which have analog output and which can be monitored with an oscillo-  
777 scope, and therefore used for testing

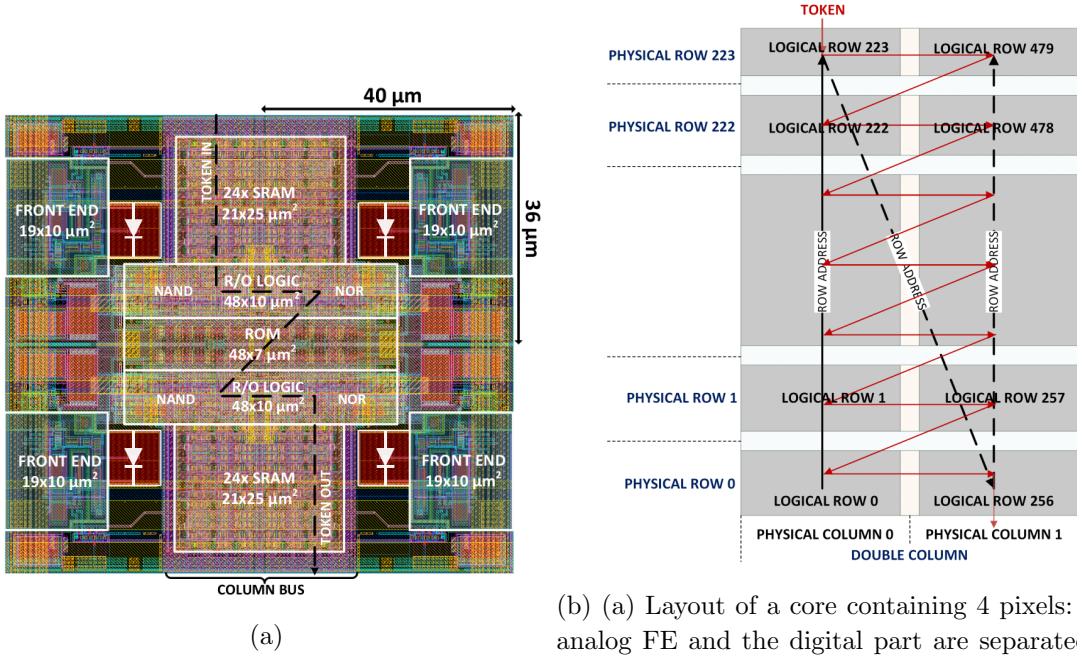
778 Pixels are grouped in  $2 \times 2$  cores (fig. 3.2a): this layout allows to separate the analog  
779 and the digital electronics area in order to reduce the possibile interference between the  
780 two parts. In addition it semplifies the routing of data as pixels on double column share  
781 the same column-bus to EoC. Therefore pixels can be addressed through the physical  
782 column/row or through the logical column/row, as shown in fig. 3.2b: in figure is also  
783 highlighted the token propagaion path, whose I will discuss later.

784 Concerning the integration4.25b of the chip in a readout path, TJ-Monopix1 chips have  
785 been wire-bonded on a dedicated carrier board , the Printed Circuit Board (PCB). Two  
786 other board between the DAQ and the chip: the General Purpose Analog Card (GPAC),

Parameter	Value
Matrix size	$1 \times 2 \text{ cm}^2$
Pixel size	$36 \times 40 \mu\text{m}^2$
Depth	$25 \mu\text{m}$
Electrode size	$2 \mu\text{m}$
BCID	40 MHz
ToT-bit	6
Power consumption	$\sim 120 \text{ mW/cm}^2$

Table 3.2: Characteristics of TJ-Monopix1 chip

787 which provides power supply channels, current/voltage bias sources and I/O buffer, and  
the MIO3 FPGA, which strictly interacts with the DAQ.



788

### 789 3.1.1 The sensor

790 As already anticipated, TJ-Monopix1 has a p-type epitaxial layer and a n doped small  
791 collection electrode ( $2 \mu\text{m}$  in diameter); to avoid the n-wells housing the PMOS transistors  
792 competing for the charge collection, a deep p-well substrate, common to all the pixel FE  
793 area, is used. TJ-Monopix1 adopts the modification described in section 2.4.2 that allows  
794 to achieve a planar depletion region near the electrode applying a relatively small reverse  
795 bias voltage. This modification improves the efficiency of the detector, especially after  
796 irradiation, however a simulation of the electric field in the sensor, made with the software  
797 TCAD (Technology Computer Aided Design), shows that a nonuniform field is still pro-  
798 duced in the lateral regions of the pixel compromising the efficiency at the corner. Two  
799 variations to the process have been proposed in order to further enhance the transversal

component of electric field at the pixel borders: on a sample of chip, which includes the one in Pisa, a portion of low dose implant has been removed, creating a step discontinuity in the deep p-well corner (fig. 3.3); the second solution proposed[MOUSTAKAS THESYS, PAG 58] consists in adding an extra deep p-well near the pixel edge. A side effect of the alteration in the low dose implant is that the separation between the deep p-well and the p-substrate becomes weak to the point that they cannot be biased separately to prevent the punchthrough.

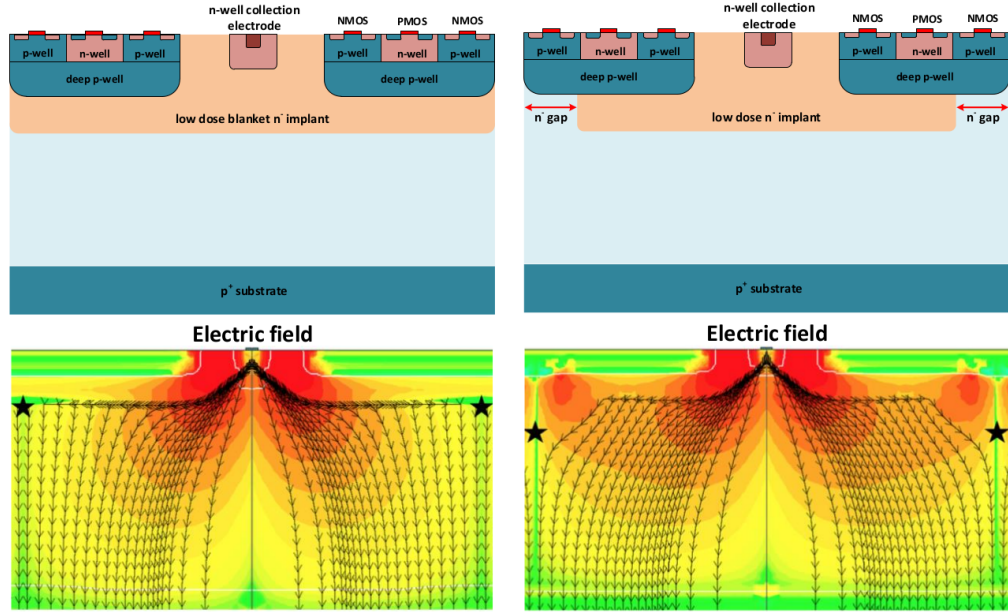


Figure 3.3: On the left the cross-section of a monolithic pixel in the TJ-Monopix with modified process; in the scheme on the right an additional gap in the low dose implant is created to improve the collection of charge due to a bigger lateral component of the electric field. The point indicated by a star at the pixel corner corresponds to the region where the transversal component of the electric field drops; introducing the gap then, a transversal component is restored and the collection becomes more efficient also in that region.

Moreover, to investigate the charge collection properties, pixels within the matrix are split between bottom top half and bottom half and feature a variation in the coverage of the deep p-well: the electronics area can be fully covered or not. In particular the pixels belonging to rows from 0 to 111 are fully covered (FDPW) and pixels belonging to rows from 112 to 223 have a reduced p-well (RDPW), resulting in a enhancement of the lateral component of the electric field.

### 3.1.2 Front end

One of the main advantage of this chip is the small collection electrode, which results in a small capacitance ( $C_{in}=3\text{ fF}$ ) allowing for high input signal amplitude and single stage of amplification, which obviously improves the signal to noise ratio performance of the FE. Assuming a fully depleted epitaxial layer of  $25\text{ }\mu\text{m}$ , which corresponds approximately to a  $20\text{ }\mu\text{m}$  of deep sensing volume, a MIP should produce  $\sim 1600\text{ e}^-$ , then:

$$V_{in} = \frac{1600\text{ e}^- \times 1.6 \cdot 10^{-19}\text{ C}}{3\text{ fF}} = 85\text{ mV} \quad (3.1)$$

819 Secondly, a reset mechanism which slowly discharges the detector capacitance must be  
 820 included in the circuit:

$$V_{in} = \frac{Q_s}{C_{in}} e^{-t/R_b C_{in}} \quad (3.2)$$

821 where  $R_b$  is the equivalent reset element. The general constraint which must be satisfied  
 822 is that the discharge time  $\tau = R_b C_{in}$  must be slower than the characteristic time of  
 823 the amplifier, otherwise a signal loss could occurs. Traditionally the reset can be  
 824 implemented in two different way: with a forward biased diode, that might be implemented  
 825 by a simple p+ diffusion inside the well of the collection electrode n, or with a PMOS  
 826 transistor. Despite of the semplicity of the diode reset, since it is a non-linear element,  
 827 the discharge would depend on the quantity of charge Q generated on the n electrode,  
 828 prejudicing the linearity of the analog output (Q-ToT). To solve the issue, a PMOS reset  
 829 is the method preferred in design such TJ-Monopix1 with analog output; the PMOS  
 830 transistor, indeed, can acts as a constant current source and then used to discharge the  
 831 sensor. Although the PMOS reset is capable of providing a constant current, it has to be  
 832 manually re-tuned every time in order to restore the input DC baseline voltage; to do that  
 833 a low-frequency feedback is used.

834 The matrix is split in four sections, each one corresponding to a different flavor of the  
 FE, implemented in order to test more options.

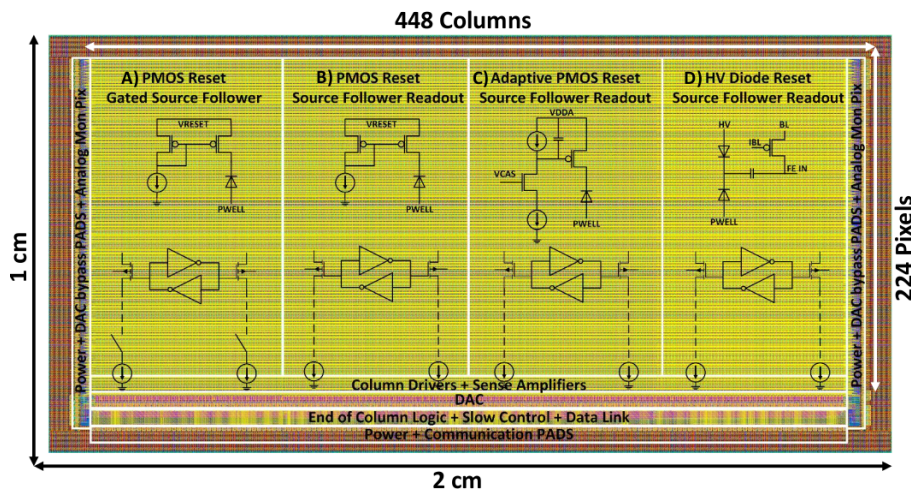


Figure 3.4: TJ-Monopix1 has been developed in four different flavor. The flavor PMOS reset (B) is considered as the reference one.

835 All the flavors implement a source-follower double-column bus readout: the standard  
 836 variation is the flavor B, that features a PMOS input reset (refered as "PMOS reset").  
 837 Flavor A is identical to flavor B except for the realization of the source follower (it is a  
 838 gated one): in the circuit of the gated versione there is a transistor more that operates on  
 839 the baseline and on the feedback mechanism; this aim to reduce the power consumption  
 840 and results in a higher signal baseline, and then in a lower effective threshold. C instead  
 841 implements a novel leakage compensation circuit, with a PMOS reset configuration. More-  
 842 over the collection electrode can be either DC-coupled to the readout electronics, as in  
 843 flavors A, B, C, or AC-coupled through a metal-oxide-metal (MOM) capacitor, as in D  
 844 is AC-coupled. The latter one allows applying a high bias voltage to the electrode n and  
 845 for this reason the flavor D is also called "HV flavor". Unfortunately the "HV" suffer  
 846 from a signal loss, which can achieve even the 50%, due to the additional parasitic capac-

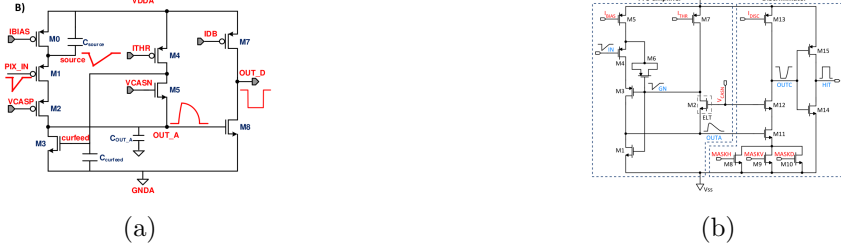


Figure 3.5

848      ity introduced at the input node. The HV voltage above which the breakdown begins is  
 849       $\sim 50$  V; however at values bigger than 20 V, the gain does not increase anymore, since the  
 850      depletion zone is already fully depleted.

851      ALPIDE chips, developed by the ALICE collaboration, implemented a standard FE to  
 852      the point that many CMOS MAPS detectors used a similar FE and are called "ALIPDE-  
 853      like". Considering that both TJ-Monopix1 and ARCADIA-MD1 have an ALPIDE-like  
 854      FE, I am going to explain the broad principles of the early FE stage.

855      The general idea is of the amplification to transfer the charge from a bigger capacity[**ALPIDE-FE**],  
 856       $C_{source}$ , to a smaller one,  $C_{out}$ : the input transistor M1 with current source IBIAS acts  
 857      as a source follower and this forces the source of M1 to be equal to the gate input  
 858       $\Delta V_{PIX\_IN} = Q_{IN}/C_{IN}$ .

$$Q_{source} = C_{source} \Delta V_{PIX\_IN} \quad (3.3)$$

859      The current in M2 and the charge accumulates on  $C_{out}$  is fixed by the one on  $C_{source}$ :

$$\Delta V_{OUT\_A} = \frac{Q_{source}}{C_{OUT\_A}} = \frac{C_{source} \Delta V_{PIX\_IN}}{C_{OUT\_A}} = \frac{C_{source}}{C_{OUT\_A}} \frac{Q_{IN}}{C_{IN}} \quad (3.4)$$

860      A second branch (M4, M5) is used to generate a low frequency feedback, where VCASN  
 861      and ITHR set the baseline value of the signal on  $C_{OUT\_A}$  and the velocity to goes down to  
 862      the baseline. The CURFEED transistor is then used to control the current in the input  
 863      branch and also determines the current that flows at the discriminator input.

864      Finally IDB defines the charge threshold with which the signal  $OUT\_A$  must be com-  
 865      pared: depending on if the signal is higher than the threshold or not, the  $OUT\_D$  is high  
 866      or low respectively.

867      The actual circuit implemented in TJ-Monopix1 is shown in figure 3.5: the principal  
 868      difference lays in the addition of disableing pixels' readout. This possibility is uttermost  
 869      important in order to reduce the hit rate and to avoid saturating the bandwidth due to the  
 870      noisy pixels, which typically are those with manufacturing defects. In the circuit transis-  
 871      tors M8, M9 and M10 have the function of disabling registers with coordinates MASKH,  
 872      MASKV and MASKD (respectively vertical, orizontal and diagonal) from readout: if all  
 873      three transistors-signals are low, the pixel's discriminator is disabled. Compared with a  
 874      configurable masking register which would allow disableing pixels individually, to use a  
 875      triple redundancy reduces the sensistivity to SEU but also gives amount of intentionally  
 876      masked ("ghost") pixels. This approach is suitable only for extremely small number N of  
 877      pixel has to be masked: if two coordinate projection scheme had been implemented, the  
 878      number of ghost pixels would have scale with  $N^2$ , if instead three coordinates are used,  
 879      the N's exponential is lower than 2 (fig. 3.6)

880      Foto dell'oscilloscopio per far vedere cosa fanno i parametri

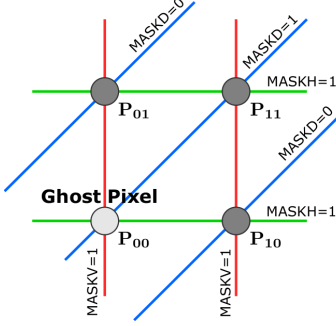


Figure 3.6

Parameter	Meaning	
IBIAS	mainly controls the rise time	yes
IDB	sets the discriminator threshold	yes
ITHR	sets the velocity of the return to the baseline	yes
ICASN	sets the baseline of the signal	yes
VRESET	sets the gain of the preamplifier	yes
IRESET	sets the gain of the preamplifier	no

Table 3.3: FE parameters which must be setted through the DAQ. "Function" means that higher parameter implies higher value

### 881 3.1.3 Readout logic

882 TJ-Monopix1 has a triggerless, fast and with ToT capability R/O which is based on a  
 883 column-drain architecture. On the pixel are located two Random Access Memory (RAM)  
 884 cells to store the 6-bit LE and 6-bit TE of the pulse, and a Read-Only Memory (ROM)  
 885 containing the 9-bit pixel address. Excluded these memories, TJ-Monopix1 hasn't any  
 886 other buffer: if a hit arrives while the pixel is already storing a previous one, the new  
 887 data get lost. After being read, the data packet is sent to the EoC periphery of the  
 888 matrix, where a serializer transfers it off-chip to an FPGA (3.7). There a FIFO is used  
 889 to temporarily stored the data, which is transmitted to a computer through an ethernet  
 890 cable in a later time.

891 The access to the pixels' memory and the transmission of the data to the EoC, following  
 892 a priority chain, is managed by control signals and is based on a Finite State Machine  
 893 (FSM) composed by four state: no-operation (NOP), freeze (FRZ), read (RD) and data  
 894 transfer (DTA). The readout sequence (??) starts with the TE of a pulse: the pixel  
 895 immediately tries to grab the column-bus turning up a hit flag signal called *token*. The  
 896 token is used to control the priority chain and propagates across the column indicating  
 897 what pixel that must be read. To start the readout and avoid that the arrival of new hits  
 898 disrupt the priority logic, a *freeze* signal is activated, and then a *read* signal controls the  
 899 readout and the access to memory. During the freeze, the state of the token for all pixels  
 900 on the matrix remains settled: this does not forbid new hits on other pixels from being  
 901 recorded, but forbids pixels hit from turning on the token until the freeze is ended. The  
 902 freeze stays on until the token covers the whole priority chain and gets the EoC: during  
 903 that time new token cannot be turned on, and all hits arrived during a freeze will turn

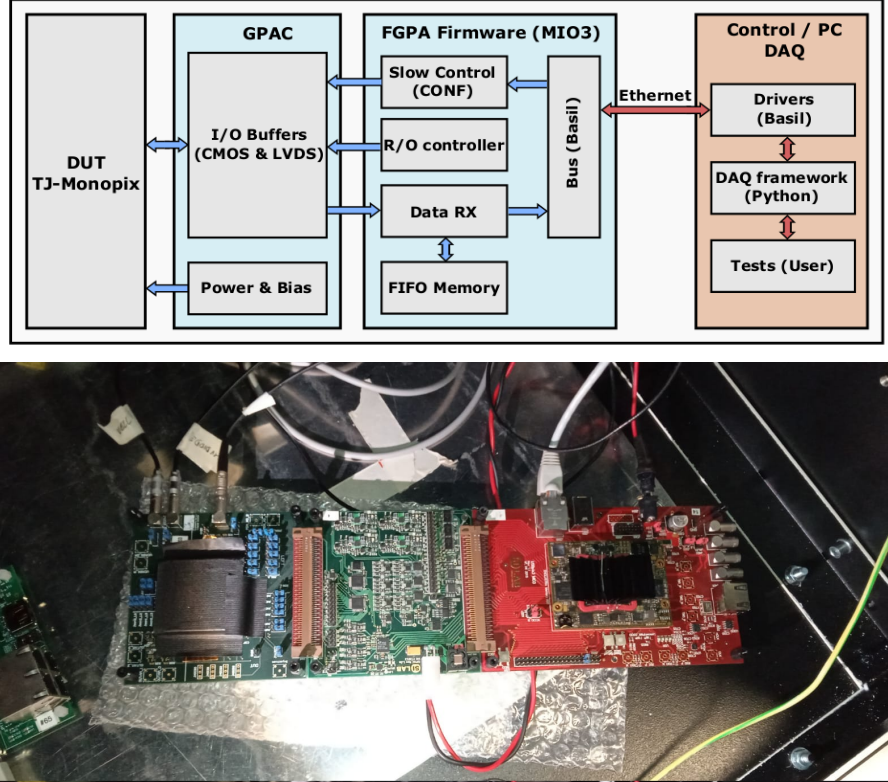
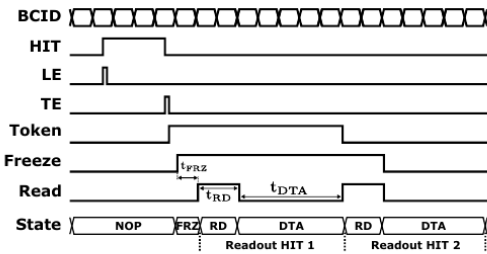


Figure 3.7: Main caption

904 on their token at the end of the previous freeze. Since the start of the token is used to  
 905 assign a timestamp to the hit, the token time has a direct impact on the time resolution  
 measurement; this could be a problem coping with high hits rate.



(b) Readout sequence timing diagram. In this example two hits are being processed.

Figure 3.8: Readout timing diagram: in this example two hits are being processed

906  
 907 The analog FE circuit and the pixel control logic are connected by an edge detector  
 908 which is used to determine the LE and the TE of the hit pulse(figure 3.9): when the TE  
 909 is stored in the first latch the edge detector is disabled and, if the **FREEZE** signal is not  
 910 set yet, the readout starts. At this point the HIT flag is set in a second latch and a token  
 911 signal is produced and depending on the value of **Token** in the pixel can be read or must  
 912 wait until the **Token in** is off. In figure an OR is used to manage the token propagation, but  
 913 since a native OR logic port cannot be implemented with CMOS logic, a sum of a NOR  
 914 and of an inverter is actually used; this construct significantly increases the propagation  
 915 delay (the timing dispersion along a column of 0.1-0.2 ns) of the token and to speed up

916 the circuit optimized solution are often implemented. When the pixel become the next to  
 917 be read in the queue, and at the rising edge of the **READ** signal, the state of the pixel is  
 918 stored in a D-latch and the pixel is allowed to use the data bus; the TE and the HIT flag  
 919 latches are reset and a **READINT** signal that enable access of the RAM and ROM cells  
 is produced.

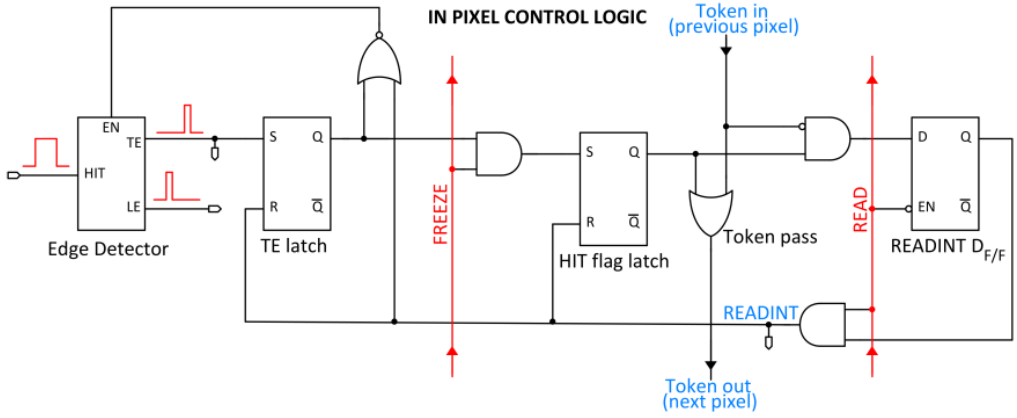


Figure 3.9

920  
 921 The final data must provide all the hits information: the pixel address, the ToT and  
 922 the timestamp. All those parts are assigned and appended at different time during the  
 923 R/O chain:

- 924 • **Pixel address:** while the double column address (6-bit) is appended by the EoC  
 925 circuit, the row address (8-bits for each flavor) and the physical column in the doublet  
 926 (1-bit) are assigned by the in-pixel logic
- 927 • **ToT:** is obtained offline from the difference of 6-bits TE and 6-bits LE, stored by  
 928 the edge detector in-pixel; since a 40 MHz BCID is distributed across the matrix,  
 929 the ToT value is range 0-64 clock cycle which corresponds to 0-1.6  $\mu$ s
- 930 • **Timestamp:** The timestamp of the hit correspond to the time when the pixel set  
 931 up the token; it is assigned by the FPGA, that uses the LE, TE and a 640 MHz  
 932 clock to derive it. For all those hits which arrived while the matrix is frozen, the  
 933 timestamp is no more correlated with the time of arrival of the particle

934 When the bits are joined up together the complete hit data packet is 27-bit. [ARCADIA-Pancheri]  
 935 [ARCADIA-Pancheri2]

### 936 3.2 ARCADIA MD1

937 ARCADIA (Advanced Readout CMOS Architectures with Depleted Integrated sensor Ar-  
 938 rays) and SEED (Sensor with Embedded Electronic Developement) are collaborations  
 939 involved in the development of MAPS sensors based on the CMOS technology and both  
 940 having LFoundry as industrial partner. Many concept and performances studies have been  
 941 carried out with simulations and small-scale test structure by SEED, before ARCADIA,  
 942 applying the experience developed with SEED to a full chip prototype, the MD1. MA-  
 943 TISSE is an example of small-scale prototypes produced for testing: it is made by  $24 \times 24$

Parameter	Value
Matrix size	$1.28 \times 1.28 \text{ cm}^2$
Pixel size	$25 \times 25 \mu\text{m}^2$
Depth	$48/100/200 \mu\text{m}$
Electrode size	$9 \times 9 \mu\text{m}^2$
Power consumption	$\sim 10 \text{ mW/cm}^2$

Table 3.4

944 pixels organised in 4 columns; each pixel has an analog output, which allows for energy  
 945 loss measurements, and a shutter snapshot readout with a speed that can reach 5 MHz.

946 The ARCADIA target are the development of a novel CMOS sensor platform allowing  
 947 for fully depleted active sensors with thickness in the range  $50 \mu\text{m}$  to  $500 \mu\text{m}$ . A  
 948 small charge collecting electrode to achieve a good signal to noise ratio, a high time res-  
 949 olution (the lower bound is set at  $O(\mu\text{s})$  but more advanced solutions are investigating  
 950 for a  $O(10 \text{ ns})$ ) and a scalable readout architecture with low power consumption are the  
 951 main requirement imposed by ARCADIA; the Main Demonstrator 1, has been submit-  
 952 ted in 2020, and its characteristic are shown in table 3.4. A second main demonstrator  
 953 (ARCADIA-MD2) has been submitted in Summer 2021, featuring a similar design of MD1,  
 954 but is expected to be faster and to have a lower power consumption thanks to a logic and  
 955 buffering optimisation.

### 956 3.2.1 The sensor and the front end

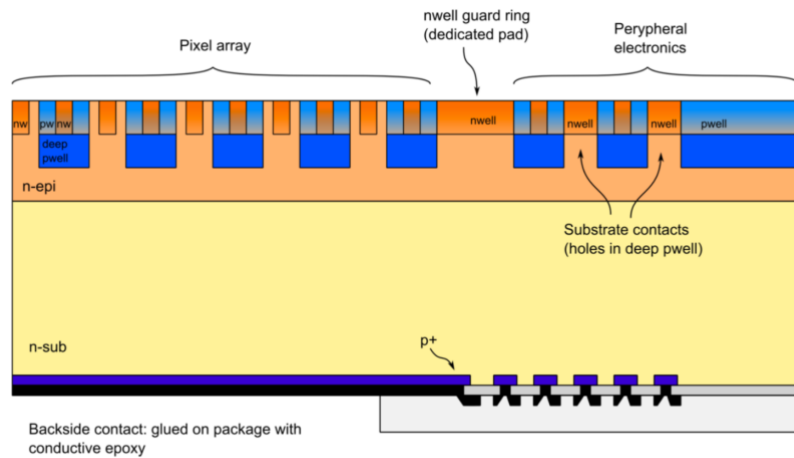


Figure 3.10: Cross section of the ARCADIA MD1 sensor

957 ARCADIA-MD1 is an LFoundry chip fabricated in 110 nm CMOS technology. The  
 958 sensor (fig.3.10) is made by a  $p$  substrate and an  $n$  doped diode within a  $n$  epitaxial  
 959 layer; a custom patterned backside has been developed in collaboration with LFoundry  
 960 to introduce junction at the bottom surface which allows a full depletion. A deep p-well  
 961 enclosure has been used to shield the n-well contained in the electronics circuit and deny  
 962 competing in charge collection; considering the isolation the resulting area available for

963 the analog circuit is  $223 \mu\text{m}^2$ .

964 Up to now the sensor has been implemented in three different variant:  $48 \mu\text{m}$ ,  $100 \mu\text{m}$   
 965 and  $200 \mu\text{m}$  thick, each with the same FE and readout logic but requiring a diffent biasing  
 966 (always higher than  $10 \text{ V}$ ). In figure 3.11 is shown a TCAD simulation, which includes  
 967 two pixels and a guard ring, of the electric-field line whithin the sensor; being part of  
 968 DMAPS and being operated in fully depletion, the charge is fastly collected by drift along  
 the elctric field lines.

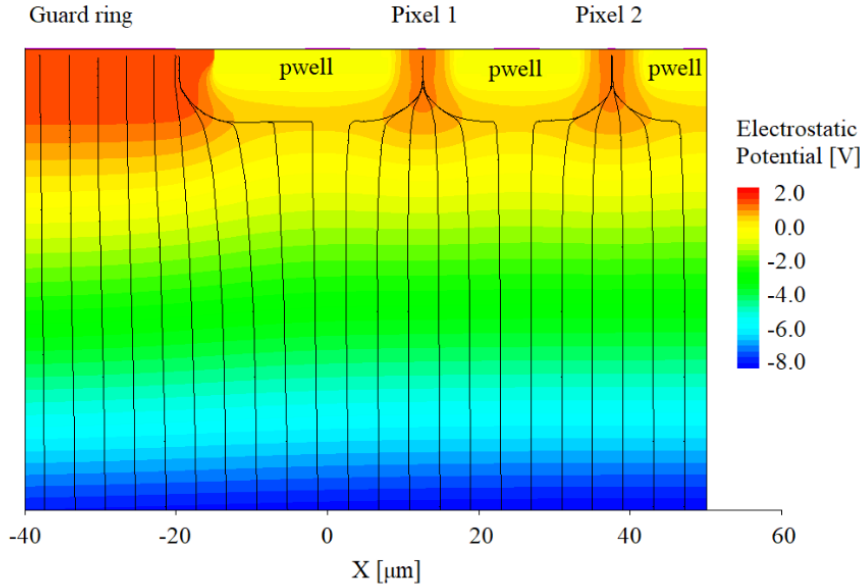


Figure 3.11: TCAD simulation of the electric field in the surface region of the sensor.

969  
 970 There are three types of configuration registers which are used to configure the matrix:

- 971 • the Pixel Configuration Register (PCR), which is a 2-bits word used for enableing  
 972 respectively the masking and injection functionalities. Each bit is made by a latch  
 973 which occupy  $14.6 \mu\text{m}^2$  out of the per-pixel area available,  $223 \mu\text{m}^2$  then it is clear  
 974 that there is not much extra space for any more configuration bits. The on-pixel  
 975 PCR circuit is shown in figure 3.12.
- 976 • the Internal Configuration Register (ICR), which are used for the comuniction with  
 977 the FPGA, for example to send a pulse, reset or configure the whole matrix.
- 978 • the Global Configuration Registers (GCR), which are used to set the configuration  
 979 of the FE parameters are similar to the one of the TJ-Monopix1 circuit, and they  
 980 are (partially) listed in table 3.5.

981 Their bias with the one of the sensors are supplied by padframes (a top, a bottom and a  
 982 side one) placed aside the matrix, which also provide the clock, the reset, the test pulse  
 983 for the injection circuit and the comunication signals. The timestamp clock, which defines  
 984 the timestamp granularity, is not internally generated but it is obtained from an external  
 985 clock of  $320 \text{ MHz}$  with a clock divider; a 4-bit GCR is used set the base-2 logarithm of the  
 986 dividing ratio, such as the timestamp clock frequency is:

$$f_{timestamp} = \frac{320 \text{ MHz}}{2^{GCR}} \quad (3.5)$$

Parameter	Meaning
CLK_DIVIDER	$\log_2$ number to divide the input clock
VINREF	provides the current to restore the input node i
VCASN	sets the threshold
IBIAS	sets the baseline
IFB	current in the feedback branch
ID	discriminator current
ICLIP	baseline

Table 3.5: FE MD1 parameters which must be setted through the DAQ.

987 and then varies in range 320 MHz and 20 MHz.

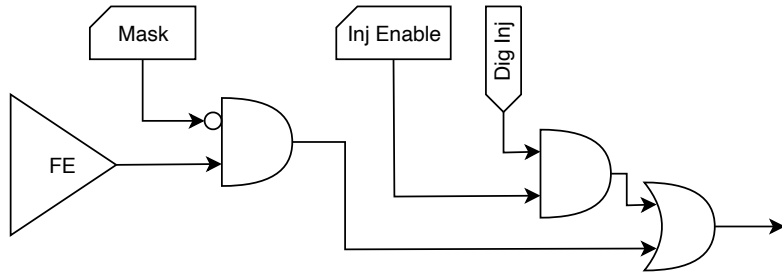


Figure 3.12: Logic used for each pixel to implement the injection and the masking.

988

989 MD1 chips have been submitted in two different front end options: they are commonly  
990 called ALPIDE-like and bulk-driven. The differences between them are in the FE circuit  
991 and in the biasing current of the registers, while the underlying readout is the same.  
992 The main difference is in the amplification stage, while in the ALPIDE-like flavor the  
993 amplification is implemented as explained in section 3.1.2, in the bulk-driven flavor the  
994 gain is adjusted by the ratio of two transconduttances. Consequently, some of the biasing  
995 registers, whose current is settable externally by the DAQ, have different default values  
996 and they might not be available at all in one of the flavor. An example is the ICLIP  
997 register, which is available only in the bulk driven flavor despite the transistor to which  
998 refers is implemented in both the flavor; its function is similar to the *curfeed* capacitor in  
999 figure 3.5(a), which controls the current in the input branch of the FE and also influences  
1000 the value of the baseline at the discriminator input.

### 1001 3.2.2 Readout logic and data structure

1002 One of the main ambition of the MD1 is to achieve the lowest possible power consumption,  
1003 hopefully less than  $20 \text{ mW/cm}^2$ ; this is important for applications in the field of space  
1004 experiment, where the power consumption and the cooling are a major issue. In order to  
1005 fulfill that requirement, the matrix is clockless and the readout is triggerless; moreover the  
1006 chip can be operated both in the high rate mode and low rate by enabling on if only one  
1007 or all serializers, placed at the periphery of the matrix. In addition, to save as much area  
1008 as possible, buffers have not been included on the matrix, at the expense of the maximum  
1009 hit rate sustainable. The readout then is completely data push and when a hit is received

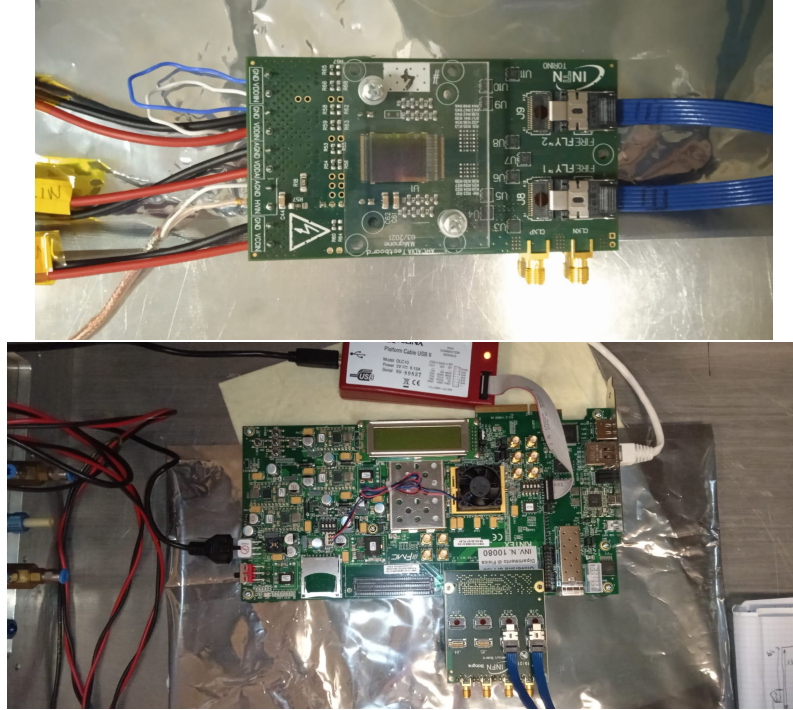


Figure 3.13: (a) Board hosting the MD1 chip. (b) FPGA and breakout board. The chip and breakout boards must be connected with the blue cables

1010 immediately starts the readout mechanism to trasmit it off chip. The board hosting the  
 1011 chip is connected with a breakout board, which is connected to the FPGA; a data packet  
 1012 sent to the EoS, is then encoded and trasmitted to the FPGA using a 320MHz DDR  
 1013 serializers and then trasmitted by ethernet to the PC. A photo of the experimental setup  
 1014 is shown in figure 3.13.

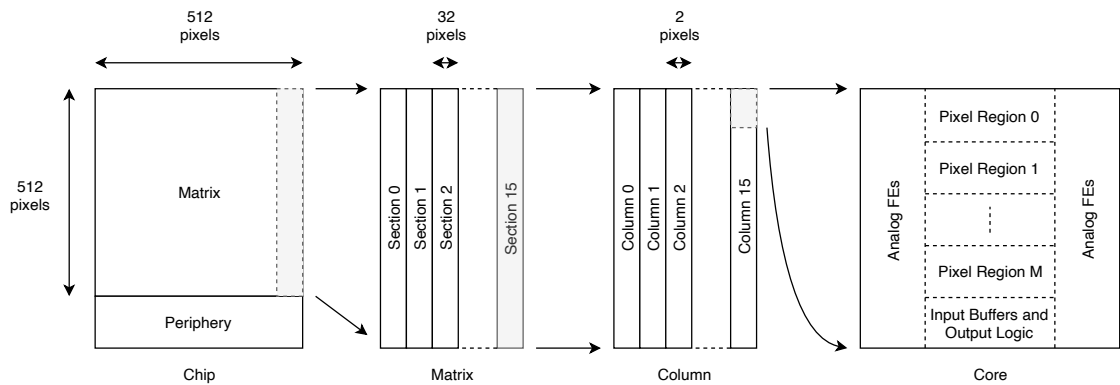


Figure 3.14: Hierarchy of the matrix division

1015 The chip structure is meant to optimize the power consumption and the scalability for  
 1016 future up-scaling retaining high rate operation; in particular it is divided into a physical  
 1017 and logical hierarchy, which also reflects in the way the data pakets are built (tab.3.6).  
 1018 First of all, the 512 columns are split in 16 sections each one containing  $512 \times 32$  pixels  
 1019 and having its own biasing lines and serializers at the matrix periphery. Each section  
 1020 is is devided  $512 \times 2$  double-column mirrored, which just as in TJ-Monopix1, share the  
 1021 same readout buses placed between them and having analog logic on the sides. The rows,

Bits	Meaning
31:24	timestamp
23:20	section index
19:16	column index
15:9	pixel region
8:0	bitmap

Table 3.6: Data packet structure implemented by the MD1 readout logic.

then, are divided in group of 32, resulting in core with  $32 \times 2$  pixels. Finally each core is sub-divided in regions, each one containing  $4 \times 2$  pixels.

The readout has been designed with the constraints of being capable of handling a rate of  $100 \text{ MHz}/\text{cm}^2$ , and it has been optimized to minimize the amount of logic and to have a high bandwidth of transmission of the data to the periphery. For this reason not all pixels have been provided of the readout logic. In particular, each pixel region can either be Master or Slave, depending on if has or has not the readout capability. The Master's data packets are therefore composed of two parts: the bitmap of the Master itself and the one of Slave. Moreover, the pioneer idea of ARCADIA-MD1, which has as final goal the test of a readout capable of transmit cluster data in as few data packets as possible, is the possibility of the Master to decide what Slave (top or bottom) to read; the information of what Slave has been selected is represented by a bit, often called *hot bit*, in the data-packet. Every pixel has an associated status register, that essentially is a flip flop (FF), which is set to 1 when the pixel stores a hit; an OR of the FF whithin the Master or the Slave region generates an active flag which is used to require a readout by the EoS. In

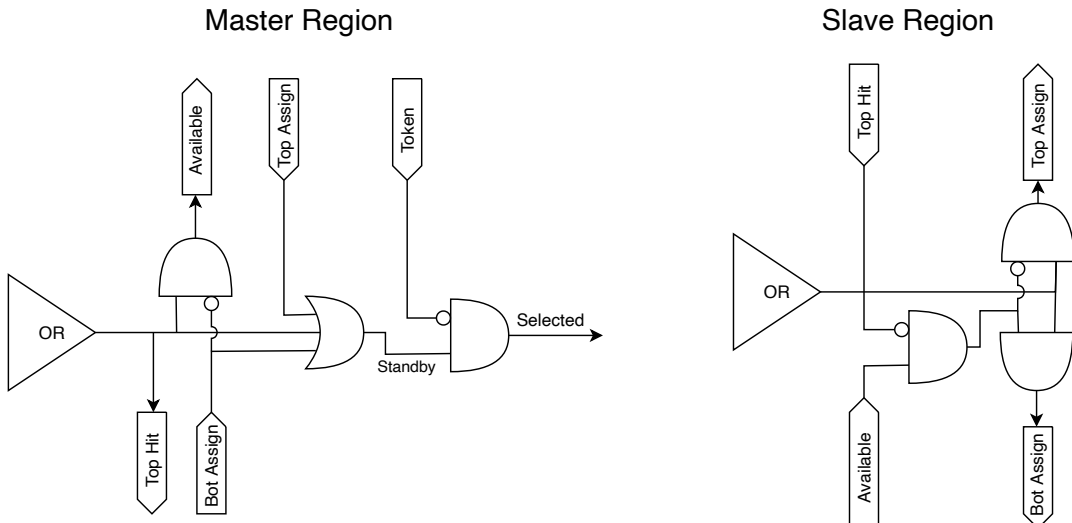


Figure 3.15: Logic of the circuit to implement the online clustering and deciding if to assign the Slave to the top or bottom Master.

figure 3.15 is shown the circuit with the logic of assignment of the Slave to the Master.

Depending on the active flags of the neighbouring Masters, the Slave bitmap is assigned to the one at the top or bottom. If both the Masters have an active flag, the Slave is assigned to the top one. In the example in figure 3.16 two Master-Slave regions are

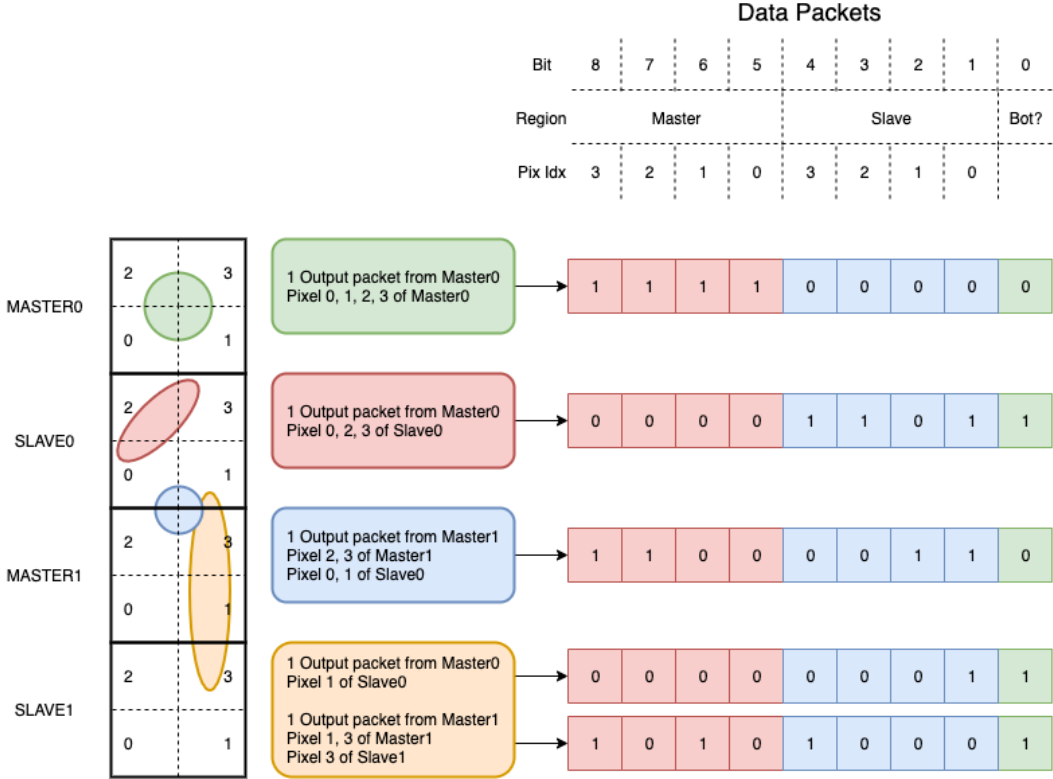


Figure 3.16: Different cluster structures and the data packet produced by them are shown in the example.

1041 considered: the hitmaps of the Master (red colored in the example) and Slave (blue colored)  
 1042 are joined together within a unique data packet and a bit (green colored) is used to specify  
 1043 the Slave.

1044 The data packets are transmitted to the End of Section (EoS) with a priority chain  
 1045 similar to what happens in TJ-Monopix1. If at least one Master set a high flag, a **Token**  
 1046 signal is generated and is assigned to the high priority Master in the column, together  
 1047 with a **Full** flag which is distributed to the active Masters in the whole column in order  
 1048 to deny more region to be accessed at the same time. The readout then propagates down  
 1049 the column from Master to Master, skipping the empty cores; the Master selected for the  
 1050 readout is the one with the flag high and with an input (from top) **Token** equal to 0. In the  
 1051 example in figure 3.17 the **Token** is propagated from the Pixel Region (PR) 10 to the PR  
 1052 7. In the three readout steps the red Masters are the ones selected for the readout, while  
 1053 the yellow are the ones which an active flag high; gray color is used for empty regions.  
 1054 When a specific Master has been selected, a **Read** signal is generated both to transmit the  
 1055 data to the EoS and also to generate a reset for the just read pixels. Once the pixels are  
 1056 reset, the Master's **Full** and **Token** flags fall, and the following region which satisfies the  
 1057 two readout conditions explained above, becomes selected.

1058 The performances of the readout has been studied with simulations by the designer  
 1059 of the chip. Random hits events with cluster size of 4 pixels on average, with a Poisso-  
 1060 nian distribution in time and uniformly distributed on the matrix has been generated.  
 1061 They state that with particle hit rate of 100 MHz/cm<sup>2</sup>, considering a portion of matrix of  
 1062 three section (512×96), the efficiency results to be 98.7%, while reducing the hit rate to  
 1063 80 MHz/cm<sup>2</sup> it is even higher achieving the 99.95%.

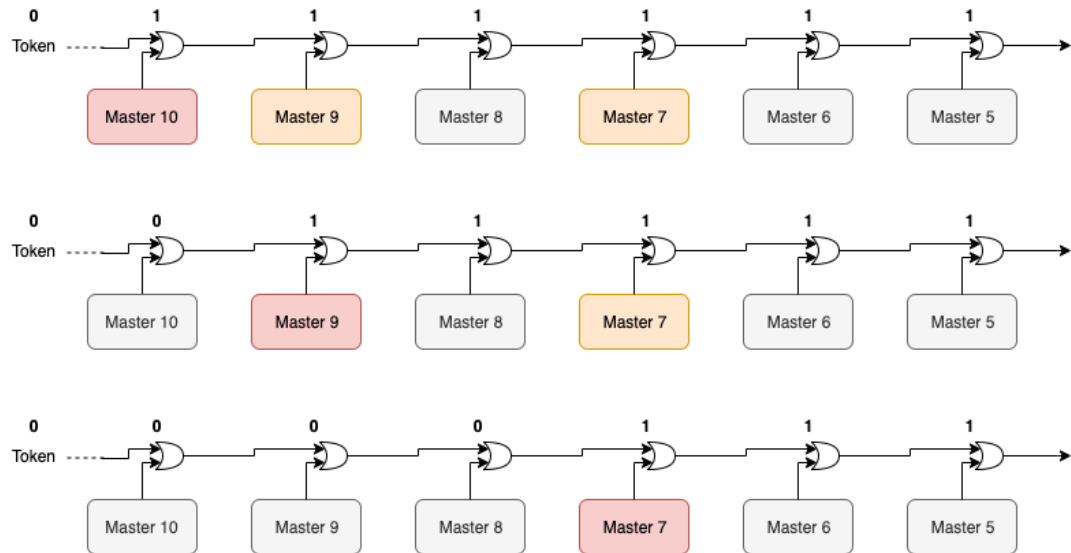


Figure 3.17: Three steps in the readout sequence on the region-column: the Token is propagated from the Master 10, to Master 9 and then to Master 7, according to the priority chain readout.

1064 Due meccanismi di perdita di dati.  
 1065 SPECIFICA CHE é DIGITALE

1066 **Chapter 4**

1067 **Characterization**

1068 Rifai il conto della lunghezza di attenuazione. Ho trovato (presentazione Luciano Mus)  
1069 29 um per ka e 37 um per kb. In this chapter I will present the tests performed  
1070 on TJ-Monopix1 and ARCADIA-MD1; firstly I will describe the characterization of TJ-  
1071 Monopix1, in terms of threshold, noise, dead time, and also provide a calibration of the  
1072 output signal, and then I will show some preliminary results obtained with ARCADIA-  
1073 MD1.

1074 **4.1 TJ-Monopix1 characterization**

1075 **4.1.1 Threshold and noise: figure of merit for pixel detectors**

1076 A characterization of threshold and noise is typically necessary since these values have an  
1077 impact on the operating conditions and on the performance of the chips, so much that  
1078 the signal to threshold ratio may be considered as the figure of merit for pixel detectors  
1079 rather than the signal to noise ratio. The mean minimum stable threshold evolved through  
1080 different generation of chips: in the 1st generation it was around  $2500 e^-$  while in the 3rd  
1081 (corresponding to nowadays chips) is less than  $500 e^-$ . This allows for thinner sensors  
1082 with smaller signals: from  $16\,000 e^-$  produced in  $200 \mu m$ , the signal expected moved down  
1083 to  $2000 e^-$  produced in  $25 \mu m$ . In agreement with this, the threshold of TJ-Monopix1 is  
1084 around  $500 e^-$ .

1085 The threshold should be located between the noise peak around the baseline and the  
1086 signal distribution, in particular it has to be low enough to mantain a high signal efficiency,  
1087 but also high enough to cut the noise: for a low threshold many pixels can fire at the same  
1088 time and a positive crosstalk feedback can set off a chain reaction eventually, causing  
1089 all the other pixels to fire. Thus, the noise sets a lower bound to the threshold: if an  
1090 occupancy  $\leq 10^{-4}$  is required, for example, a probability of firing lower than that value  
1091 is needed and this, assuming a gaussian noise, requires that the threshold is set at least  
1092  $3.7\sigma$ , with  $\sigma$  the RMS of the noise. In this case, if the noise is  $100 e^-$  (resonable), the  
1093 threshold must be higher than  $3.7 \times 100 e^-$ . Typically this argument sets only a minimal  
1094 bound to the threshold since the variation with time and from pixel to pixel have to be  
1095 taken into account: the temperature, the shift in MOSFET threshold voltage caused by  
1096 radiation damage in the oxide layer and the process parameters variation across the wafer  
1097 (as for examplt process mismatch between transistors).

1098 The noise is parameterized as Equivalent Noise Charge (ENC), which is defined as the  
1099 ratio between the noise N at the output expressed in Volt and the out voltage signal S

1100 produced by  $1 e^-$  entering in the preamplifier:

$$ENC = \frac{N_{out}[V]}{S_{out}[V/e^-]} = \frac{V_{noise}^{RMS}}{G} \quad (4.1)$$

1101 with G expressed in V/e $-$ . Considering the threshold dispersion a requirement for the  
1102 ENC is:

$$T > n \cdot ENC \oplus T_{RMS}(x) \oplus T_{RMS}(t) \quad (4.2)$$

1103 where  $T_{RMS}$  is the threshold variation during time (t) and across the matrix (x), and n  
1104 corresponds to the number of  $\sigma$  of noise from which the threshold must set in order to  
1105 obtain a firing probability lower than a certain value; for example, assuming a gaussian  
1106 distribution, if n equal to 3.7, the probability that the pixel fires is less than  $10^{-4}$ .

1107 Because of the changing of the 'real' threshold, the possibility of changing and adapting  
1108 the setting parameters of the FE, both in time and in space is desiderable: these parameters  
1109 are usually set by Digital to Analog Converter (DAC) with a number of bits in a typical  
1110 range of 3-7. Unfortunately DAC elements require a lot of space that may be not available  
1111 on the pixel area; therefore, the FE parameters are typically global, which means that they  
1112 are assigned for the whole chip, or they can be assigned for regions the matrix is divided  
1113 into. The former case corresponds to TJ-Monopix1's design in which 7 bits are used for a  
1114 total 127-DAC possible values, while the latter corresponds to the ARCADIA-MD1's one,  
1115 6-bits. Another possibility, for example implemented in TJ-Monopix2, is to allocate the  
1116 space on each pixel for a subset of bits, then combinig the global threshold with a fine  
1117 tuning. If so, the threshold dispersion after tuning is expected to decrease depening on  
1118 the number of bits available for tuning:

$$\sigma_{THR,tuned} = \frac{\sigma_{THR}}{2^{nbit}} \quad (4.3)$$

1119 where  $\sigma_{thr}$  is the RMS of the threshold spread before tuning.

1120 To measure the threshold and noise of pixels a possible way is to make a scan varying a  
1121 known charge injected through a dedicated injection capacitor: the threshold corresponds  
1122 to the value where the efficiency of the signal exceeds the 50%, and the ENC is determined  
1123 from the inverse of the slope at this point. Assuming a gaussian noise, e.g. a noise  
1124 whose transfer function turns a voltage  $\delta$  pulse in a gaussian distribution, the efficiency of  
1125 detecting the signal and the noise can be described with the function below:

$$f(x, \mu, \sigma) = \frac{1}{2} \left( 1 + erf \left( \frac{x - \mu}{\sigma \sqrt{2}} \right) \right) \quad (4.4)$$

1126 where  $erf$  is the error function. Referring to 4.4 the threshold and the ENC corresponds  
1127 to the  $\mu$  and  $\sigma$ .

1128 I used the injection circuit available on the chip to inject 100 pulses for each in-  
1129 put charge for a fixed threshold. The charge injection is realized sending a voltage  
1130 step  $V_{inj}$ (DAC) on an injection capacitance implemented at the input of the FE circuit  
1131 ( $Q_{inj} = C_{inj} V_{inj}$ ). Knowing the nominal value of the  $C_{inj}$  (230 aF for the PMOS flavor) one  
1132 can calculate the conversion factor for the signal injected from DAC to  $e^-$ . Since the DAC  
1133 are biased at 1.8 V, the Least significant Bit (LSB) corresponds to a voltage of 14.06 mV  
1134 from which (for the PMOS flavor) the charge for LSB  $1.4375 e^-/\text{mV}$  and the conversion  
1135 factor therefore is  $20.2 e^-/\text{DAC}$ . While this value is equivalent for all the PMOS flavor, the  
1136 HV flavor is expected to have a different conversion factor,  $\sim 33 e^-/\text{DAC}$ , beacuse of the

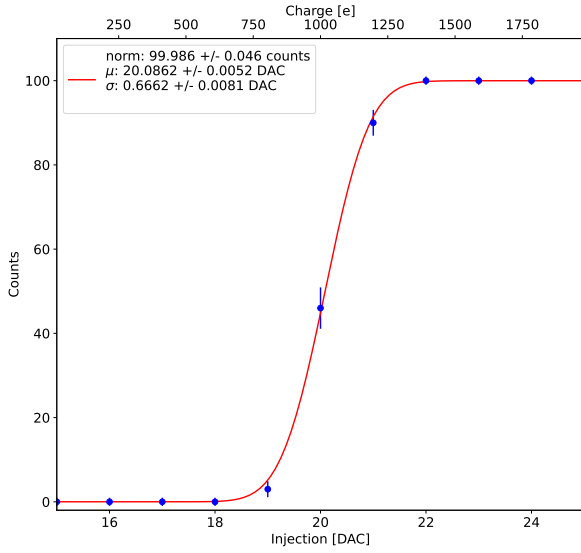


Figure 4.1: S-curve for pixel (10, 10) of the PMOS flavor (flavor B) with IDB fixed at 40 DAC. The conversion of charge injected from DAC to electrons has been performed using a nominal conversion factor of  $20.3 \text{ e}^-/\text{DAC}$  *Mi sono resa conto che l'asse superiore è sbagliato. Devo rigenerare il plot*

1137 different injection capacitance. Besides the charge, also the duration and the period of the  
 1138 injection pulse can be set; it is important to make the duration short enough to have the  
 1139 falling edge during the dead time of the pixel (in particular during the FREEZE signal)  
 1140 in order to avoid the undershoot, coming at high input charge, triggering the readout and  
 1141 creating spurious hits. Since the injection circuit is coupled in AC to the FE, if the falling  
 1142 edge of the pulse is sharp enough to produce an undershoot, this can be seen as a signal.

1143 Therefore I fitted the counts detected using the function in equation 4.4. Figure 4.1  
 1144 shows an example of such fit for a pixel belonging to the flavor B with the register IDB,  
 1145 which sets the discriminator threshold, fixed at 40 DAC; in figure 4.2 are shown the 1D  
 1146 and 2D distributions of the parameters found for the PMOS B flavor. Then I fitted the  
 1147 1D-histograms with a gaussian function to find the average and RMS of the noise and  
 1148 the threshold across the matrix. The results for each flavor are reported in table 4.1;  
 1149 no relevant differences among the flavors have been observed regarding the noise, which  
 1150 results to be  $\lesssim 15 \text{ e}^-$ , while the threshold has been found to be  $\sim 400 \text{ e}^-$  except for the  
 1151 PMOS C flavor, where, with the same FE settings, it is  $\sim 540 \text{ e}^-$ .

	PMOS A	PMOS B	PMOS C	HV
Threshold [ $e^-$ ]	$401.7 \pm 0.2$	$400.8 \pm 0.2$	$539.7 \pm 0.6$	$403.9 \pm 0.2$
Threshold dispersion [ $e^-$ ]	$32.9 \pm 0.1$	$33.0 \pm 0.2$	$55.5 \pm 0.4$	$44.7 \pm 0.2$
Noise [ $e^-$ ]	$13.01 \pm 0.06$	$12.26 \pm 0.07$	$13.9 \pm 0.1$	$11.7 \pm 0.1$
Noise dispersion [ $e^-$ ]	$1.61 \pm 0.04$	$1.50 \pm 0.05$	$1.91 \pm 0.07$	$1.58 \pm 0.07$

Table 4.1: Mean threshold and noise parameters for all flavor and their dispersion on the matrix.

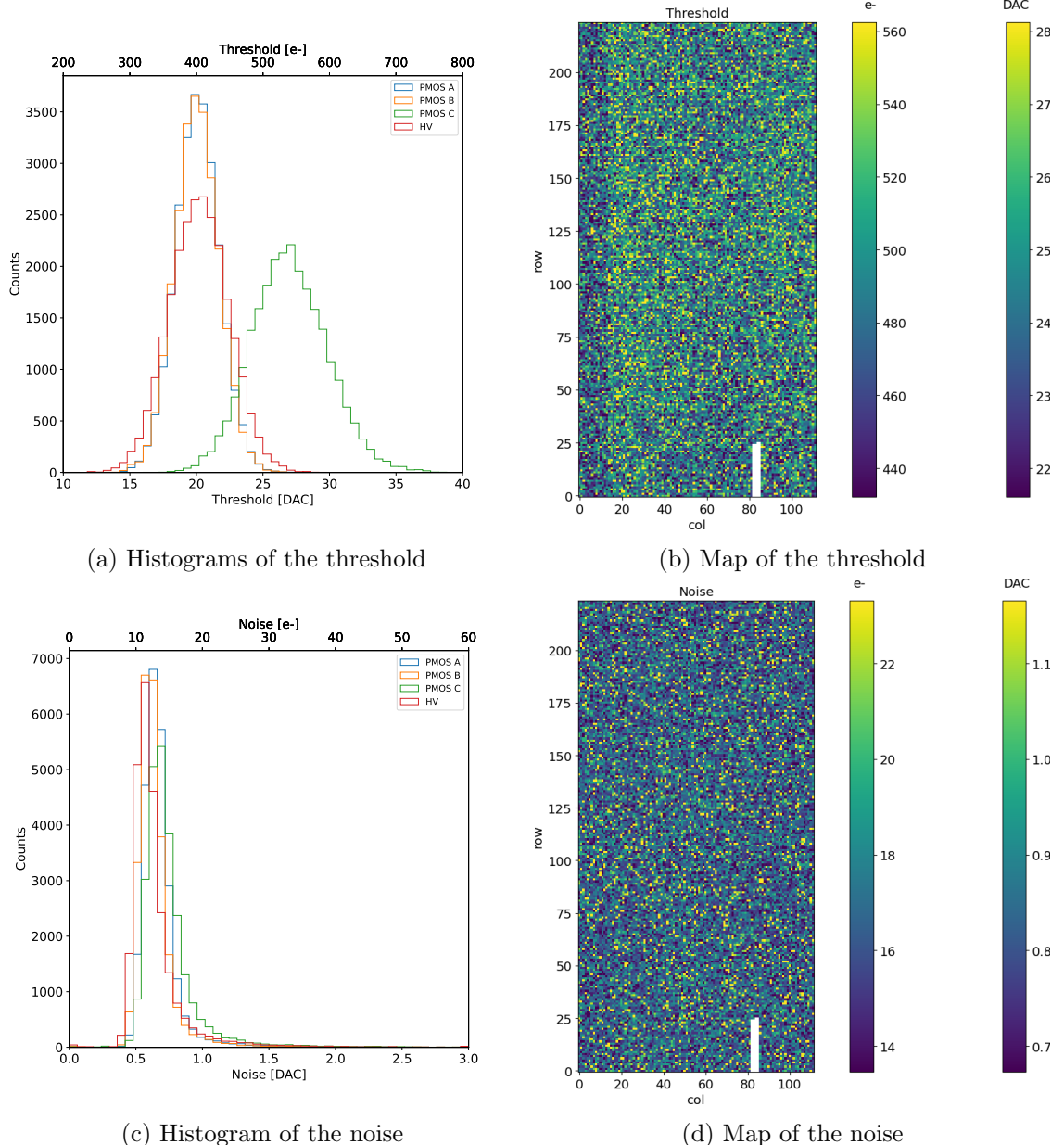


Figure 4.2: The threshold and the noise have been found fitting the s-curve of all flavor with IDB fixed at 40 DAC. The white pixels have the injection circuit broken

1152        Although a slightly lower threshold is visible in the first biasing section (columns from  
 1153        0 to 14) in the map in figure 4.2b; similar structures, but extended to the entire matrix,  
 1154        appear more evidently when using different IDB values. The systematic threshold variation  
 1155        across the biasing group has not a well established explanation, but one could certainly be  
 1156        the transistor mismatch of the biasing DAC registers IDB and ICASN, which both adjust  
 1157        the effective threshold (ICASN regulates the baseline and in the presented measurement  
 1158        has been set at the minimum value, that is 0 DAC).

1159        To verified the trend of the threshold as a function of the front end parameter IDB and  
 1160        find its dynamic range, I have performed different scans changing the FE register IDB. For  
 1161        each value I have injected the whole matrix and searched for the mean and the standard  
 1162        deviation of the threshold and noise distributions. The results are shown in figure 4.3: the  
 1163        blue points are the mean threhsold found whithin the matrix, while in green is shown the  
 1164        width (threshold  $\pm\sigma$ ) of the threshold distribution, i.e. the threshold dispersion. While  
 1165        the threshold increases at higher IDB, the ENC decreases of  $\sim 4 e^-$ , which is  $\sim 1/3$  of the  
 noise at IDB=40 DAC. **Ma ora che ci penso forse del noise ci dovrei mettere un plot?**

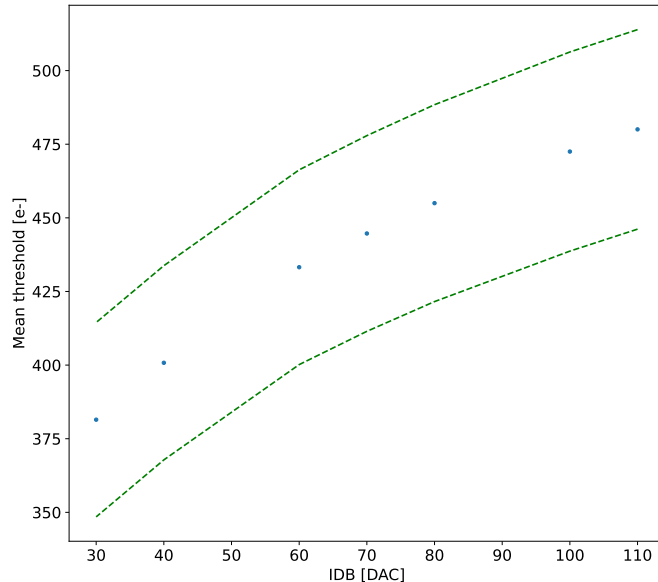


Figure 4.3: Flavor PMOS (B) with Psub-Pwell biased at -6 V. Threshold measured in electrons vs the register which sets the threshold, IDB.

1166  
 1167        Then, to evalute the operation and the occupancy of the chip at different threshold  
 1168        I have made long acquisitions of noise at different IDB and check how the number of  
 1169        pixel masked changes with the threshold. The masking algorithm I have used search for  
 1170        pixels with rate >10 Hz and mask them. With such algorithm, in our standard condition,  
 1171        IDB=40 DAC, a very low noise hit rate is intentionally achieved masking a dozen of pixels  
 1172        of the whole flavor.

1173 **4.1.2 Linearity of the ToT**

1174 I have already stated in chapter 3 that TJ-Monopix1 returns an output signal proportional  
1175 to the charge released by a particle in the epitaxial layer, which is the Time over  
1176 Threshold; the ToT is saved as a 6-bit variable and therefore its dynamic range is 0-64,  
1177 which corresponds to 0-1.6 $\mu$ s assuming a clock frequency of 40 MHz. When a pulse is  
1178 longer than 1.6 $\mu$ s the counter rolls back to zero and there is no way to distinguish that  
1179 charge from a lower one with the same ToT: that is the rollover of the ToT (4.4b(a)).

1180 In order to associate the ToT (in range 0-64) to the charge, a calibration of the signal  
1181 is necessary. The output of TJ-Monopix1 is approximately a triangular pulse, resulting in  
1182 a linear relationship between ToT and charge:

$$Q [DAC] = \frac{(ToT [au] - offset [au])}{slope [au/DAC]} \quad (4.5)$$

1183 where m and q are the fitted parameters of the calibration. It is important to keep in  
1184 mind that the main application target of TJ-Monopix1 is in the inner tracker detector  
1185 of HEP experiments, then the main feature is the efficiency, then a rough calibration of  
1186 the signal to charge is fine. The ToT information can be used both to better reconstruct  
1187 the charge deposition in cluster in order to improve the track resolution, and for particle  
1188 identification, through  $\frac{dE}{dx}$ , especially for low momentum particles which do not reach the  
1189 dedicated detectors.

1190 The study of the output signal has been possible via the injection: I fitted the ToT  
1191 versus the charge injected for all the pixels within the matrix. In figure 4.4b there is  
1192 an example of fit for a pixel belonging to the flavor B, while in figure 4.5 there are the  
1193 histograms and the maps of the parameters of the line-fit for all flavors with IDB fixed at  
1194 40 DAC. Here again a difference among the biasing section appears: since the slope of the  
1195 ToT is related to the gain of the preamplifier (increasing the gain also increases the ToT),  
1196 the mismatch is probably due to the transistor contributing to the amplification stage.

1197 I fitted the average ToT of all the pulses recorded as a function of the pulse amplitude;  
1198 data affected by rollover have been removed in order to avoid introducing a bias in the  
1199 mean values. In figure 4.4b are shown both the fits with a line (red) and with a second  
1200 order polynomial (green): at the bounds of the ToT range values deviate from the line  
1201 model. Since the deviation is lower than 1% and it only interests the region near the 0  
1202 and the 64, in first approximation it is negligible.

1203 **4.1.3 Calibration of the ToT**

1204 Finding a calibration for the ToT means defining a way to pass from the ToT values  
1205 (0-64 clock counts) to a spectrum expressed in electrons collected. The principles of  
1206 the calibration are the following: the ToT in clock counts maps (eq.4.1.2) a DAC range  
1207 between the threshold and a value which depends on the pixel and generally is around  
1208 90-100 DAC. Assuming that a 0 DAC signal corresponds to  $0 e^-$ , if another reference point  
1209 is fixed, a linear calibration function can be defined. After the calibration the ToT goes  
1210 to map a charge range between the threshold and  $Q_{max}$  which is a function of the pixel  
1211 and is around  $2 ke^-$ .

1212 Moreover, considering that the charge injected in the FE depends on the value of the  
1213  $C_{inj}$  ( $Q_{inj} = C_{inj} V_{inj}$ ) which is different from pixel to pixel, the true charge injected does  
1214 not correspond to the nominal value expected assuming  $C_{inj} = 230$  aF. Accordingly to that,

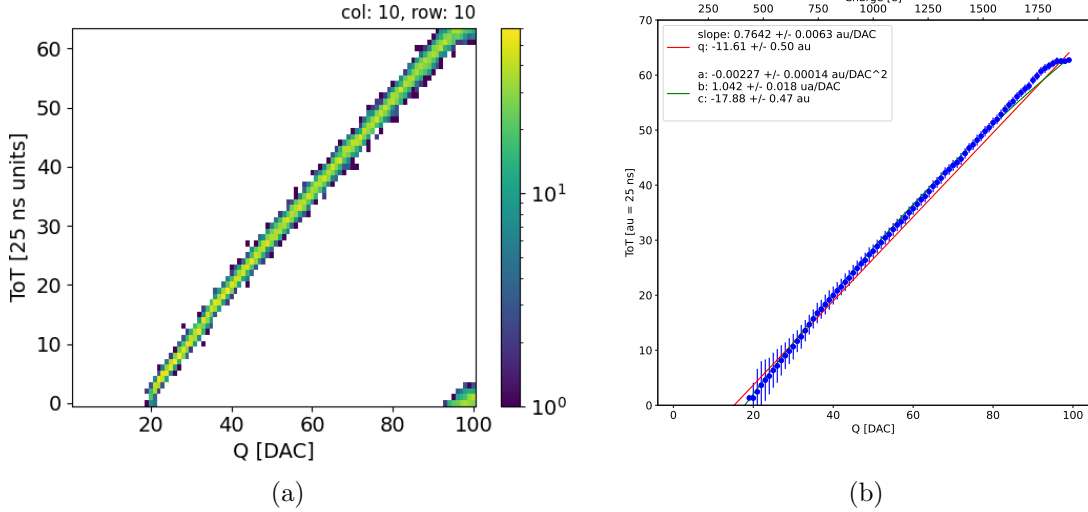


Figure 4.4: The figures refer to pixel (10, 10) of the PMOS-reset flavor B with IDB fixed at 40 DAC. (a) Histogram of the injection pulses: the ToT is in range 0-64 since it is represented by 6 bit, so when achieving the 64 it rolls over back to the zero. (b) Mean ToT vs the the charge: the mean has been calculated removing the rollover hits.

1215 a measurement of the injection capacitance provides both an absolute calibration of  $C_{inj}$   
 1216 and a conversion factor K to have a correspondence of the DAC signal in electrons. K and  
 1217  $C_{inj}$  are defined respectively as:

$$K [e^-/\text{DAC}] = \frac{1616 [e^-]}{Q [\text{DAC}]} \quad (4.6)$$

$$C_{inj} [\text{F}] = K [e^-/\text{DAC}] \frac{1.6 \cdot 10^{-19} [\text{C}]}{14.06 [\text{mV}]} \quad (4.7)$$

1218 where  $1616 e^-$  is the number of electrons produced in the detector by the calibration  
 1219 source (Fe55) and  $14.06 \text{ mV}$  is the voltage value of a DAC (LSB). K is expected to be  
 1220  $20 e^-/\text{DAC}$ , assuming the nominal value of C equal to  $230 \text{ aF}$ , and where 1616 is the  
 1221 expected number of electrons produced by the calibration source used, Fe55. Fe55 is en  
 1222 extremely important radionuclide in the calibration of X-ray spectrometers, proportional  
 1223 counter and scintillator detector since it emits two two X-photons during the electron  
 1224 capture decay: the first one ( $K_\alpha$ ) at  $5.9 \text{ keV}$  and the second one ( $K_\beta$ ) at  $6.5 \text{ keV}$ . The  
 1225  $K_\alpha$  photon, which does photoelectric effect in silicon, has an absorption length  $\lambda=7 \mu\text{m}$  to  
 1226  $8 \mu\text{m}$ , and the probability of being assorbed in the  $25 \mu\text{m}$  thick epitaxial layer is  $\sim 0.95\%$ .  
 1227 The electron emitted has an energy equal to the photon, so recalling that the mean energy  
 1228 needed to produce a couple electron-vacuum is  $3.65 \text{ eV}$ , the signal produced by the Fe55  
 1229 source is expected to be  $1616 e^-$ . In figures 4.6 are shown two histograms of the ToT  
 1230 spectrum of the Fe55 source for two different pixels. The peak on the right corresponds  
 1231 to the events with complete absorption of the charge in the depleted region, while the  
 1232 long tail on the left to all the events with partial absorption due to charge sharing among  
 1233 neighbors pixels. In order to reduce the consistent charge sharing, the pixel dimension in  
 1234 TJ-Monopix2 has been reduced down to  $30 \times 30 \mu\text{m}^2$ . The events on the right side of the  
 1235 peak, instead, corresponds to the  $K_\beta$  photons. Looking at the histograms for pixel (30,  
 1236 185) and (30, 68) respectively at top and bottom of figure 4.6, a significant difference in  
 1237

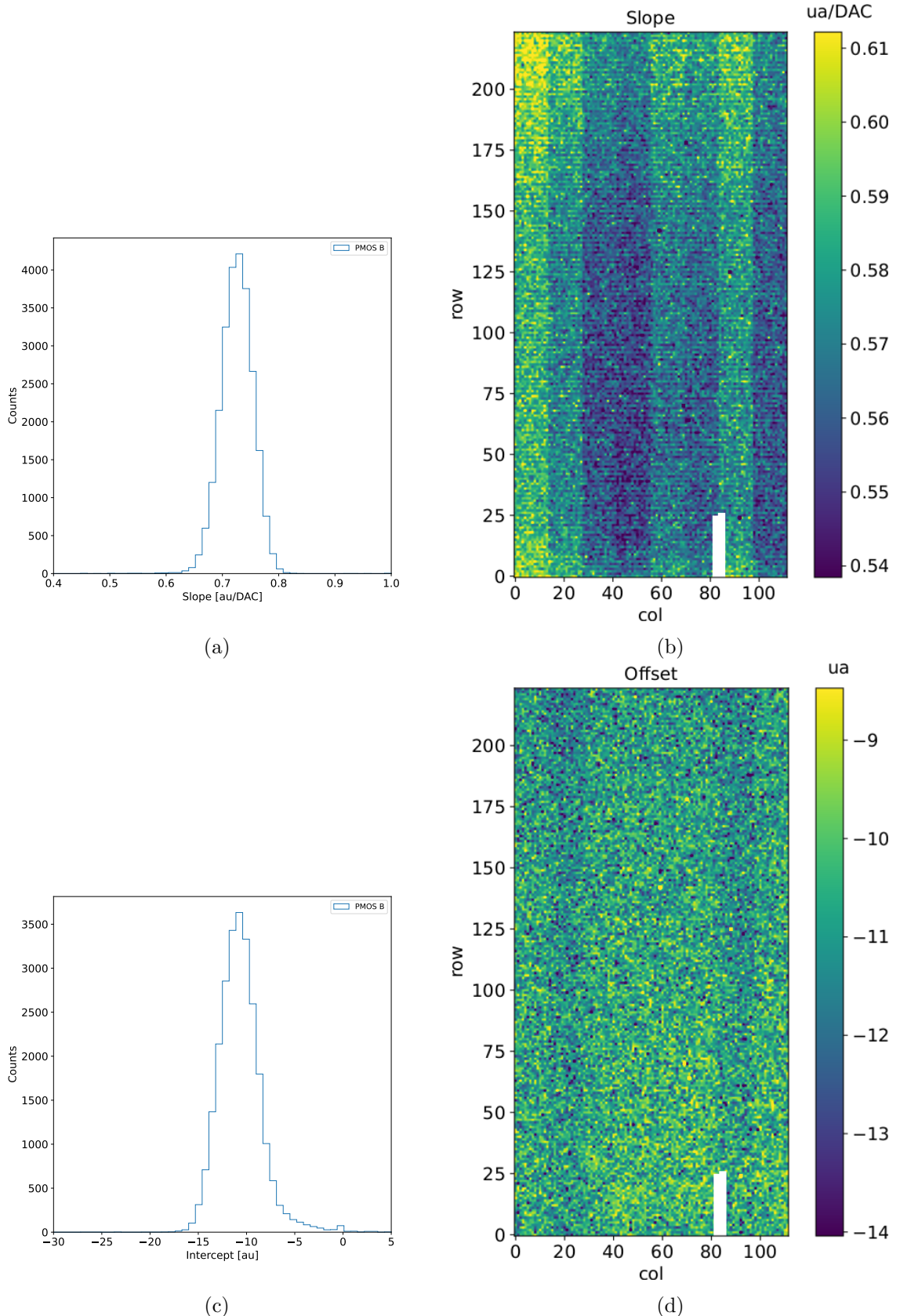


Figure 4.5: Histograms of the calibration parameters, slope (a) and offset (b), found fitting the ToT with a line, for the flavor B and with IDB fixed at 40 DAC. Maps of the calibration parameters, slope (a) and offset (b), found fitting the ToT with a line, with IDB fixed at 40 DAC.

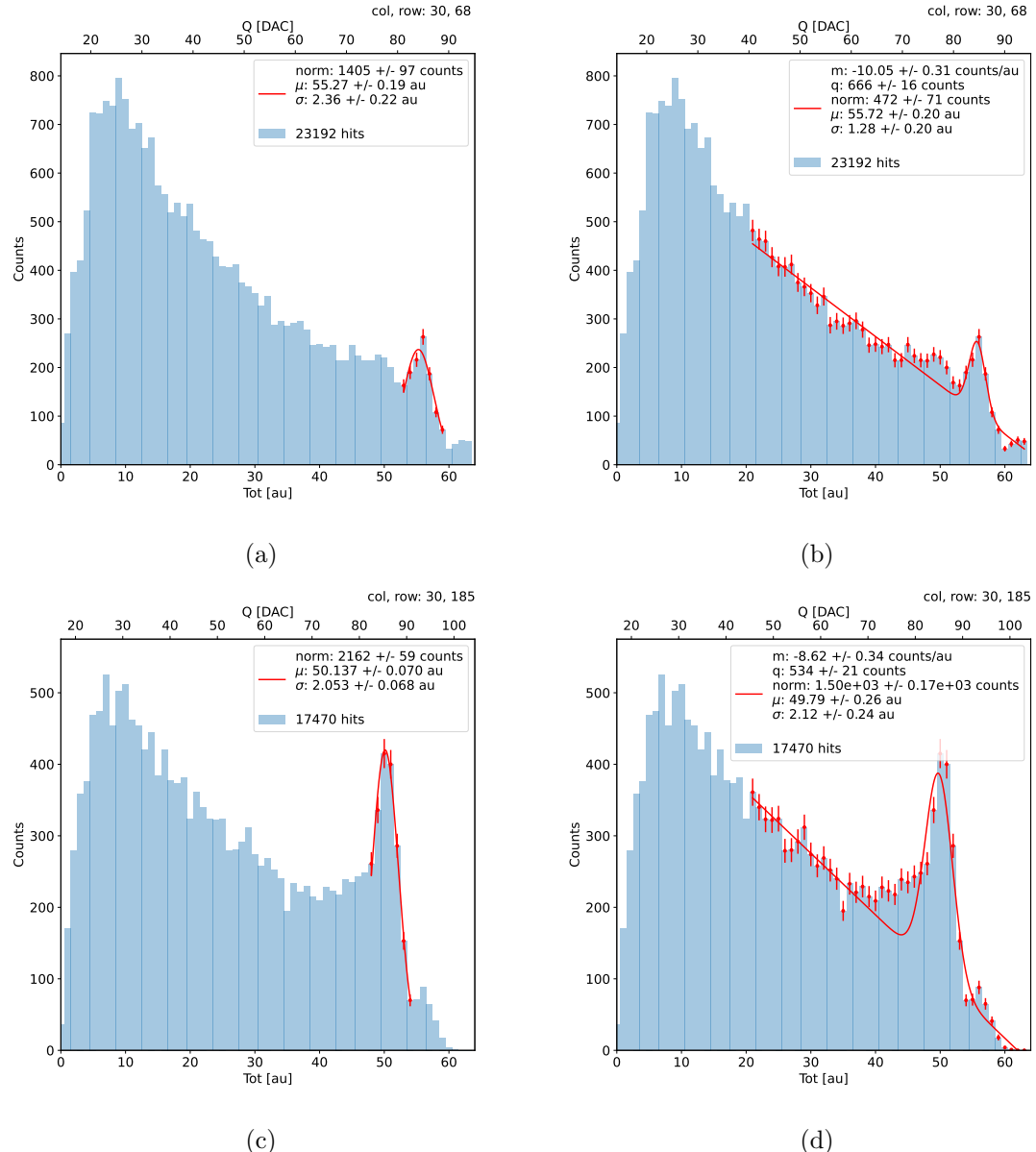


Figure 4.6: Both strategies 4.8 and 4.9 of fitting the Fe55 peak are shown for two pixels on the matrix: the (a) and (b) refers to pixel (30, 68) which has a FDPW, while the (c) and (d) refers to pixel (30, 185) which has a RDPW. The fit has been performed using the bins colored by red.

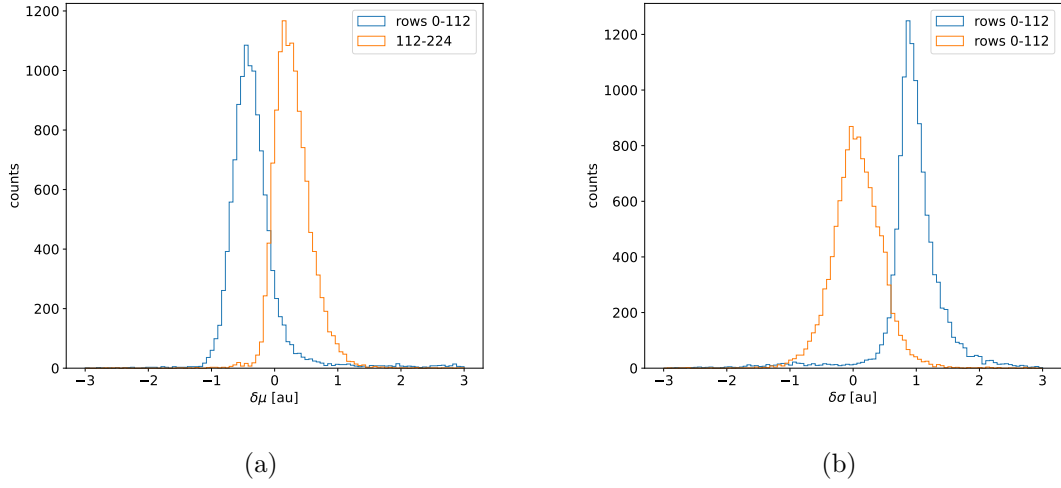


Figure 4.7: Difference between the parameters  $\mu$  and  $\sigma$  obtained with the gaussian fit and those obtained with a gaussian plus a line. When  $\mu < 0$  the fit with function 4.8 is generally worse (the peak is shifted to the left); when  $\sigma < 0$ , the fit with 4.9 is worse (larger sigma).

1238 the peak to tail ratio leaps out, which can be related with the position of the pixel in  
 1239 the matrix. In particular, because of a different charge collection property, pixels in the  
 1240 upper part of the matrix (rows 112-224) have a more prominent peak, while in pixels in  
 1241 the lower part (rows 0-111) there is a higher partial absorption. Indeed, as discussed in  
 1242 section 3.1.1, there is a distinction in the structure of the low dose-epi layer among the  
 1243 rows, in particular pixels in rows 112-224, which have a Reduced Deep P-Well (RDPW),  
 1244 are supposed to have a higher efficiency in the pixel corner.

1245 For the calibration I needed to establish the peak position; to do that I fitted the ToT  
 1246 histogram of each pixel. I tested two different fit functions:

$$f(x, N, \mu, \sigma) = \frac{N}{\sigma\sqrt{2\pi}} e^{-\frac{1}{2}(\frac{(x-\mu)}{\sigma})^2} \quad (4.8)$$

$$f(x, m, q, N, \mu, \sigma) = m x + q + \frac{N}{\sigma\sqrt{2\pi}} e^{-\frac{1}{2}(\frac{(x-\mu)}{\sigma})^2} \quad (4.9)$$

1248 The additional linear term in equation 4.9 is meant to model the tail due to incomplete  
 1249 charge collection and prevent it from introducing a bias in the fitted peak position.

1250 For this reason, when fitting with eq.4.9, I selected a larger region compared to the  
 1251 fit with eq.4.8, for which I used only a small reagion around the peak. The optimal fit  
 1252 region was chosen in both cases through an iterative routine: for the fit with eq.4.9 it  
 1253 starts from an interval including all the pixels above 20 DAC and progressively reduces it  
 1254 by increasing the left boundary; for the fit with eq.4.8, it starts from an interval of 5 bins  
 1255 around the expected peak position and reduces the interval of 1 bin at each iteration.

1256 Even if the difference in the peak position between the two fit strategies is not really  
 1257 relevant for the purpose of the calibration, being of the order of 0.8-1.5% (4.7),it still  
 1258 introduces a systematic bias towards lower values due to the contribution of the tail.  
 1259 Indeed, we know that the sharp edge on the right must correspond to the case of complete  
 1260 absorption of the photon, so that, in general, the closest to this feature is the fitted peak  
 1261 position, the better the fit is. A poor fit tends also to overestimate the peak width. Even

1262 looking at the  $\chi^2$ , the fit function 4.8 seems to be the better choice, except for a set of  
 1263 pixels in the lower part of the matrix, the ones with lower efficiency.

1264 The resolution of the detector, which is expected to be determined by the statistical  
 1265 fluctuations in the number of charge carries generated in the detector as well as by the  
 1266 ENC, can be compared to the observed Fe55 peak width. Ideally:

$$\sigma_{Fe} = \sqrt{ENC^2 + F \times N} \quad (4.10)$$

1267 Since the number of e/h pairs produced in the sensor is 1616, recalling that F for a  
 1268 silicon detector is 0.115 and that the ENC measured with the injection is  $12 e^-$ , the  $\sigma_{Fe}$  is  
 1269 expected to be  $\sim 18 e^-$ . Looking at figure 4.8 the resolution achieved with the Fe55 source  
 1270 seems to be much worse. A contribution we have not taken into account but is certainly  
 1271 relevant is the systematic overestimation of the standard deviation of the Fe55 peak: this,  
 1272 as I already explained, is principally due to the high background of incomplete charge  
 1273 collection, which broadens the fitted peak. Although, this effect is not sufficient to justify  
 1274 a such high peak width value. 2D maps of the value of the capacity and of the conversion  
 1275 factor found are shown in 4.9. The evident stripe-structure in the matrix shows an evident  
 1276 correlation among the same row; the same structure, which is also visible in the slope map  
 1277 of the calibration of the ToT (fig.4.5b), may be related with the structure of the bias lines.  
 1278

1279 An attempt of calibrating the HV flavor, which is the most different from the PMOS  
 1280 B flavor, has been performed; however, because of the loss of signal caused by the higher  
 1281 capacity, we have been unable to identify the Fe55 peak, and then the calibration of the  
 1282 ToT in electrons has been impossible. Moreover the HV flavor did not seem to work  
 1283 properly, as we have observed that all pixels sometimes fire one time simultaneously. For  
 1284 these reasons unfortunately a complete characterization of the HV flavor has not been  
 1285 possible: in fact, since it has the most particular FE compared to the other PMOS flavor,  
 1286 a comparing the results wold be particularly interesting. An example of Fe55 spectrum  
 1287 collected with the HV flavor is shown in figure 4.10.

#### 1288 4.1.4 Changing the bias

1289 In order to study the behavior of the sensor as a function of the bias, I performed several  
 1290 injection scans in different bias conditions. The thickness of the depletion region, which  
 1291 extends with higher bias voltage, has to be considered an important parameters affecting  
 1292 the signal efficiency, and in particular it affects the charge released by a particle which  
 1293 crosses the sensor, since the signal is proportional to the thickness of the epitaxial layer.

1294 Another important benefit of operating the FE with higher bias is the reduction of the  
 1295 capacitance of the collecting diode  $C_{in}$ , and the corresponding increase of the gain of the  
 1296 first stage of the FE, which goes as  $\sim 1/C_{in}$  (as explained in sec. 3.1.2). **With higher gain**  
 1297 **the ENC is reduced (eq 5.1) as well as the discriminator threshold and its dispersion that**  
 1298 **are again reported to equivalent input charge with the usual conversions**

$$1299 THR_{DISC}(e-) = V_{disc}(mV)/gain(mV/e-).$$

$$1300 sigma_{THR_{DISC}}(e-) = V_{rms_{disc}}(mV)/gain(mV/e-)$$

1301 An example of expected change of gain with increased bias is shown in fig.4.11, that  
 1302 reports the output voltage amplitude and gain for the PMOS and HV flavours for chips  
 1303 characterized by other groups. Given that the chip under examination has a gap in the low  
 1304 dose epi-layer, we were not able to change independently the bias of the substrate (PSUB)

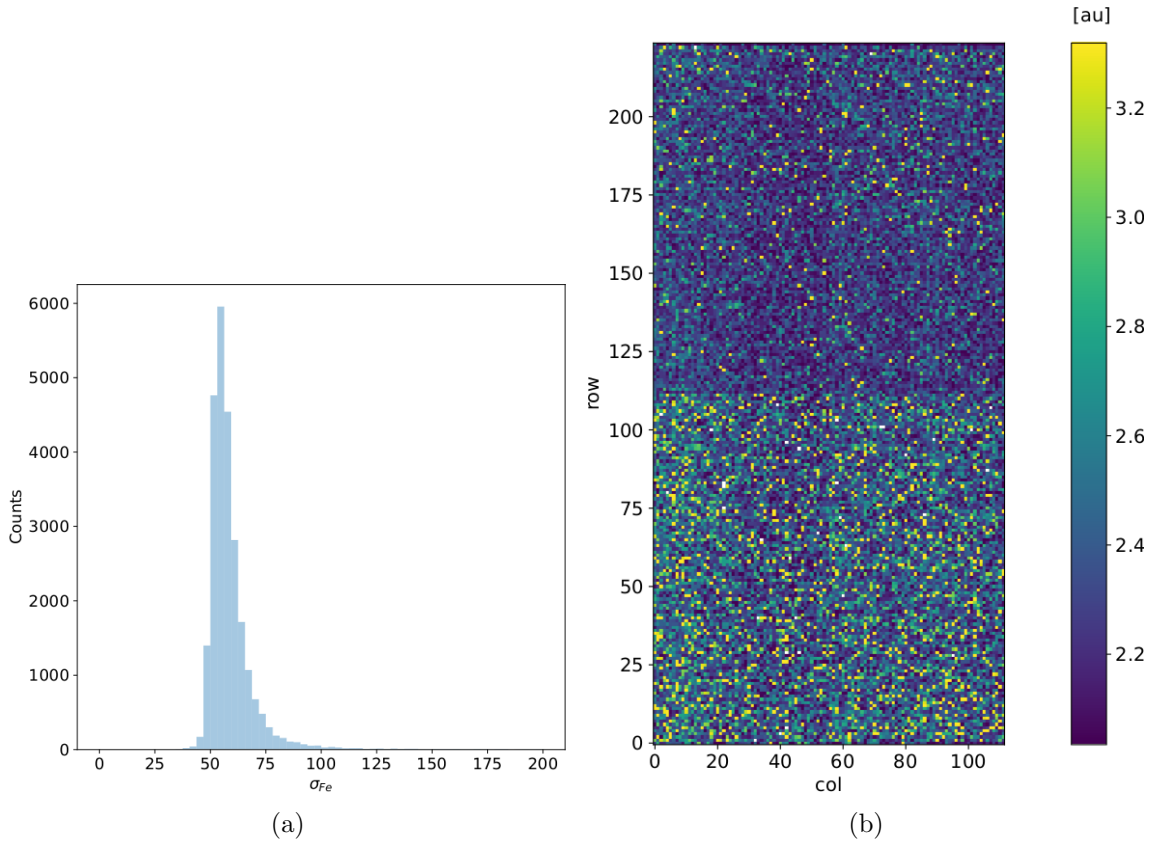


Figure 4.8: (a) Histogram and (b) map of the Fe55 width found by the fit with function 4.8 converted in electrons using the calibration. In the map a clear difference between the two parts of the matrix can be distinguished: in particular, as already stated, the rows with RDPW have a better resolution. It worth noting that the pixels which in the above maps appear disable, here do not show any problem. This prove that they have a problem in the injection circuit but not in the sensor and in the FE.

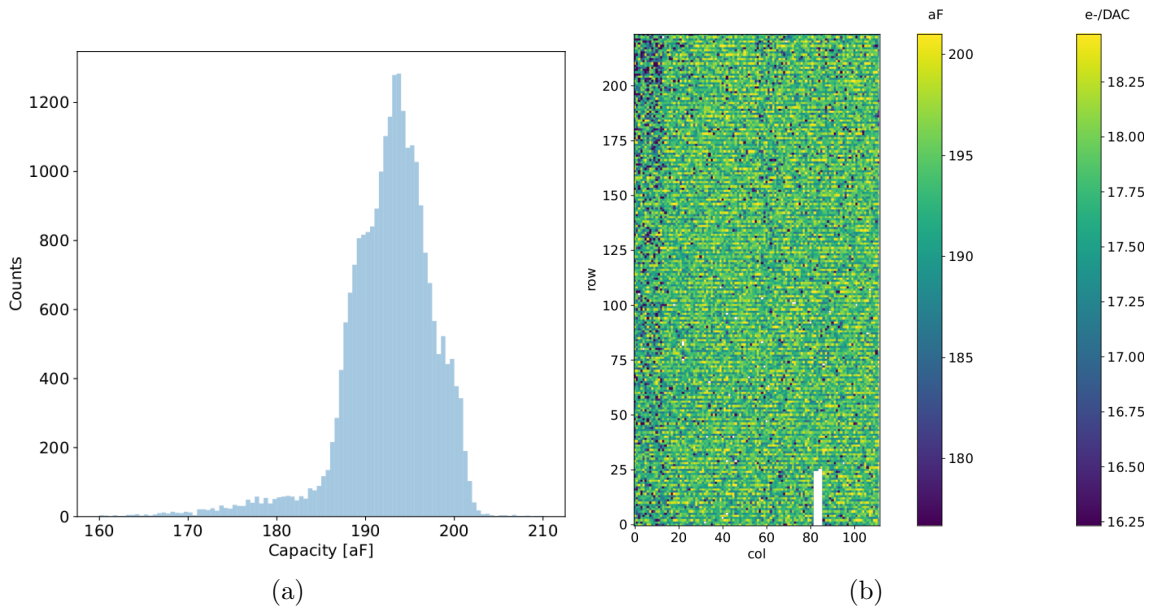


Figure 4.9: Histogram (a) and map (b) of the calibrated capacity of the injection circuit.

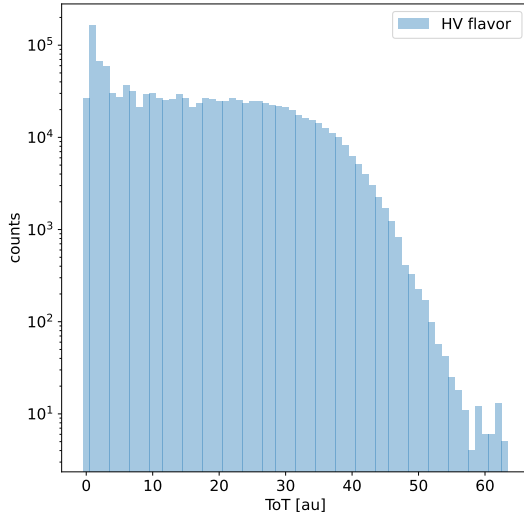


Figure 4.10: Fe55 spectrum with the HV flavor. No peak has been identified because of the loss of the signal due to the higher input capacity.

1305 and of the p-well (PWELL), but they must be kept at the same value, differently from  
 1306 other chips of the same submission. Lowering the bias, the depletion region is expected  
 1307 to narrow and the efficiency to reduce, especially in the pixel corner, thus raising the  
 1308 threshold and the noise and decreasing the slope as a consequence of the reduction in the  
 gain.

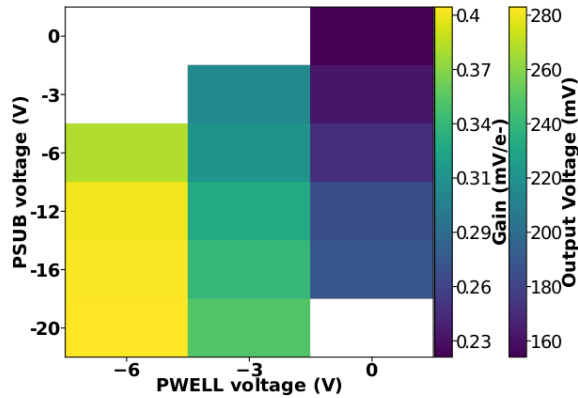


Figure 4.11: Output voltage amplitude and gain with respect to the p-well and p-substrate voltage in the case of the PMOS reset front-end. [referenza tesi mustakas](#)

1309  
 1310 In order to test the behavior of the chip when not completely depleted, I have performed  
 1311 an injection scan with PSUB/PWELL bias at 0 V, -3 V and -6 V (results in tab.4.2);  
 1312 passing from -6 V to a smaller depletion at 0 V, reduces the slope of the output signal of  
 1313  $\sim 1/4$ , which is smaller than the reduction in gain reported in figure 4.11, that is  $\sim 1/3$ .  
 1314 Moreover the increase in the threshold and noise at smaller bias is due to the fact that  
 1315 diffusion becomes a competing collection mechanism, with all the consequences described  
 1316 in section 2.4. Figure 4.12 shows the values of the  $K_\alpha$  peak position, the normalization of  
 1317 the events above the peak that is the normalization coming from the gaussian fit of the

	-6 V	-3 V	0 V
Threshold [DAC]	$20 \pm 2$	$21 \pm 2$	$24 \pm 2$
Noise [DAC]	$0.61 \pm 0.08$	$0.62 \pm 0.08$	$0.82 \pm 0.1$
Slope [au/DAC]	$0.73 \pm 0.03$	$0.71 \pm 0.03$	$0.57 \pm 0.02$
Offset [au]	$-11 \pm 2$	$-11 \pm 2$	$-11 \pm 2$

Table 4.2: The errors of the values are the standard deviations of the corresponding distributions. To convert DAC values to electrons can be used the conversion factor  $\sim 20 \text{ e-}/\text{DAC}$  (nominal) or  $\sim 18 \text{ e-}/\text{DAC}$  (measured).

peak, and the rate as a function of the PSUB/PWELL biases. These quantity have been normalized to their value at -6 V, which is then defined as the reference condition. As expected with reduced bias two effects occur: firstly the position of the Fe55 peak moves to lower values due to a lower gain (the reduction of  $\sim 1/3$  is in agreement with the value measured in [M]), secondly the number of events in the Fe55 peak and rate both become smaller since the depletion region is reduced. So, what happens is the decrease of both the number of events with full collection (of the  $1616 \text{ e-}$  from the Fe55 photon) in a single pixel, which contributes to the normalization of the peak, but also the reduction of the events with charge sharing among neighbours pixels.

#### 4.1.5 Measurements with radioactive sources

In order to completely validate the operation of the whole sensor<sup>1</sup>, I have performed several acquisitions with radioactive sources, specifically Fe55 and Sr90Y, which is a  $\beta^-$  emettitor with electron endpoint at 2.2 MeV, and cosmic rays. I used the data collected with Sr90 and cosmic rays, to study charge sharing and events with more than one hit.

I define *cluster* the ensemble of all the hits with the same timestamp. This is obviously a coarse requirement, but it gave me the opportunity of using a simple and fast clustering algorithm, which is fine when the random coincidence probability is negligible. Defining  $R_1$  and  $R_2$  as the two events rate, and  $\tau$  as the dead time of the detector, the random coincidence rate can be found:

$$R_{coinc} = R_1 \times R_2 \times \tau \quad (4.11)$$

As I am going to prove in the next section, the dead time strictly depends on the occupancy of the matrix, even though we can assume a dead time of  $\sim 1 \mu\text{s}$ , which corresponds to the mean dead time per pixel. However, if in an event a particle hits two different pixels producing a cluster, the total dead time simply doubles. Since the measured rate on the whole matrix of noise, Fe55, Sr90 and cosmic rays are  $\sim \text{Hz}$ ,  $3.3 \text{ kHz}$ ,  $40 \text{ Hz}$  and  $\sim 10 \text{ mHz}$ <sup>2</sup>, the random coincidence probability are negligible except the one of two Fe55 events, which is  $11 \text{ Hz}$ .

In figure 4.13 I report the histograms of the number of pixels in the cluster and of the dimension of clusters, defined in terms of the max and min coordinates on the matrix as:

$$d = \sqrt{(y_{max} - y_{min})^2 + (x_{max} - x_{min})^2} \quad (4.12)$$

---

<sup>1</sup>As I will discuss in chapter 5.2 these measurements serves also as a reference for the spectrum observed at the test beam

<sup>2</sup>The cosmic rays rate at the sea level is expected to be  $\sim 1/\text{cm}^2/\text{s}$

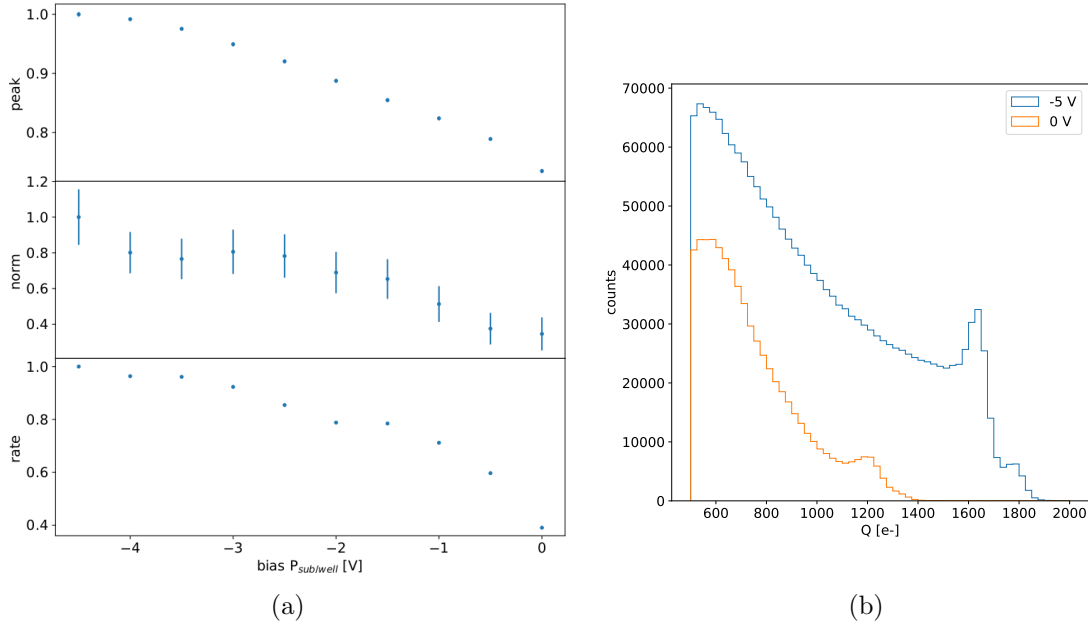


Figure 4.12: (a) Peak position, peak amplitude and rate as a function of the bias. Since during the collection of the whole data the source has been moved, it is not guaranteed that it has always had a repositioning in the same exactly place, then small the fluctuation of the rate along the decreasing trend are acceptable. The peak position and amplitude are estimated by fitting the spectrum with a gaussian in the region around the peak. (b) Fe55 spectrum at different  $P_{sub/well}$  bias. The ToT values have been calibrated as explained in section. 4.1.3.

1346 Looking at the shape of the histogram of the dimension, generally the Sr90 and the  
 1347 cosmic rays produce bigger clusters and hit a higher number of pixels, a trend that can  
 1348 be explained considering that the Fe55 photoelectron is much less energetic than the Sr90  
 1349 electron and cosmic rays.

1350 Below I have also attached a sample of bitmap of events produced by the three different  
 1351 sources (fig.4.14, 4.15 and 4.16).

1352 In figures 4.18, 4.19, 4.20 are shown the distributions per different cluster dimension  
 1353 events, of the charge collected by a single pixel (figures on the left) and the charge collected  
 1354 by summing the charge collected by the pixels within the cluster (figures on the right).  
 1355 Since the noise rate is comparable with the cosmic rays and Sr90 ones, I have removed the  
 1356 single pixel events which are separately shown in figure 4.17; although we cannot identify  
 1357 and select only the noise events, these distributions, and especially the cosmic rays one, are  
 1358 expected to be mostly populated by noise events. The distributions have a peak around  
 1359 the threshold, which is compatible with the fact that the noise events typically have a low  
 1360 ToT.

1361 Looking at the spectra of Sr90 instead (fig:4.19), the maximum of the distribution  
 1362 of the cluster charge seems to follow a linear dependence on the number of pixels hit  
 1363 (tab.4.3); this can be accepted as a first approximation considering that the pitch ( $36\ \mu m$   
 1364 and  $40\ \mu m$ ) depending on the direction, and the epitaxial layer thickness ( $25\text{-}30\ \mu m$ ) are  
 1365 comparable. However a more accurate model which takes into account the impact angle  
 1366 of the particle should be developed for a more precise comparison.

1367 Regarding the Fe55, the bump in the cluster spectrum at  $\sim 1616\ e^-$  corresponds to

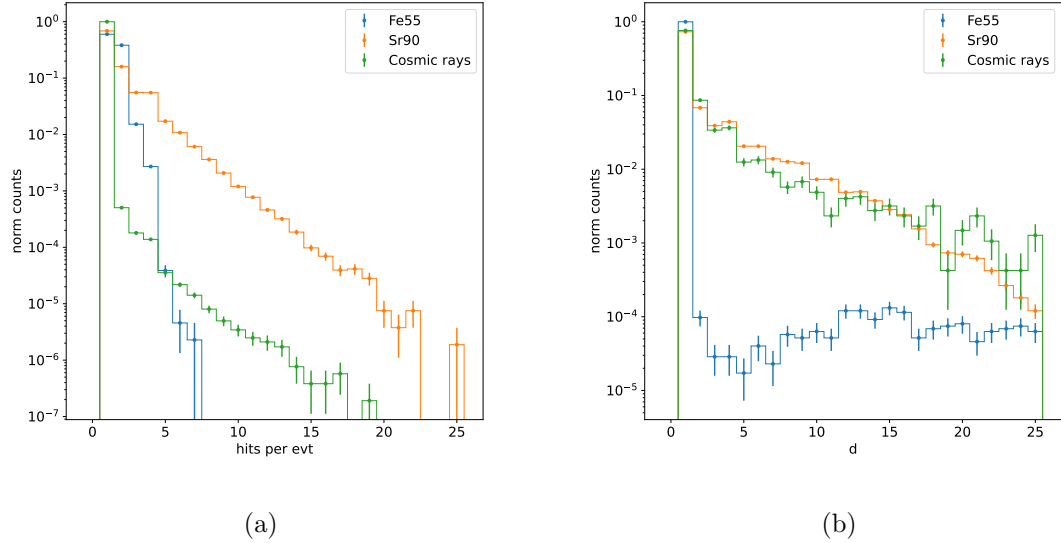


Figure 4.13: (a) Distribution of the number of hits per event with different sources. (b) Dimension of cluster defined as eq.4.1.5. Compared with the Sr90 and the cosmic rays, the Fe55 d distribution is characterized by a clear discontinuity around  $d=5$ . The very thin peak at 0 corresponds to the effective clusters, while the long tail at bigger  $d$  is principally made of random coincidence distant on the matrix.

Pixel per evt	Measured [e-]
2	$950 \pm 30$
3	$1450 \pm 30$
4	$2050 \pm 30$
5	$2450 \pm 30$

Table 4.3: Position of the maximum of the distributions in figure 4.19b of the summed charge released in the clusters depending on the number of pixel in the cluster.

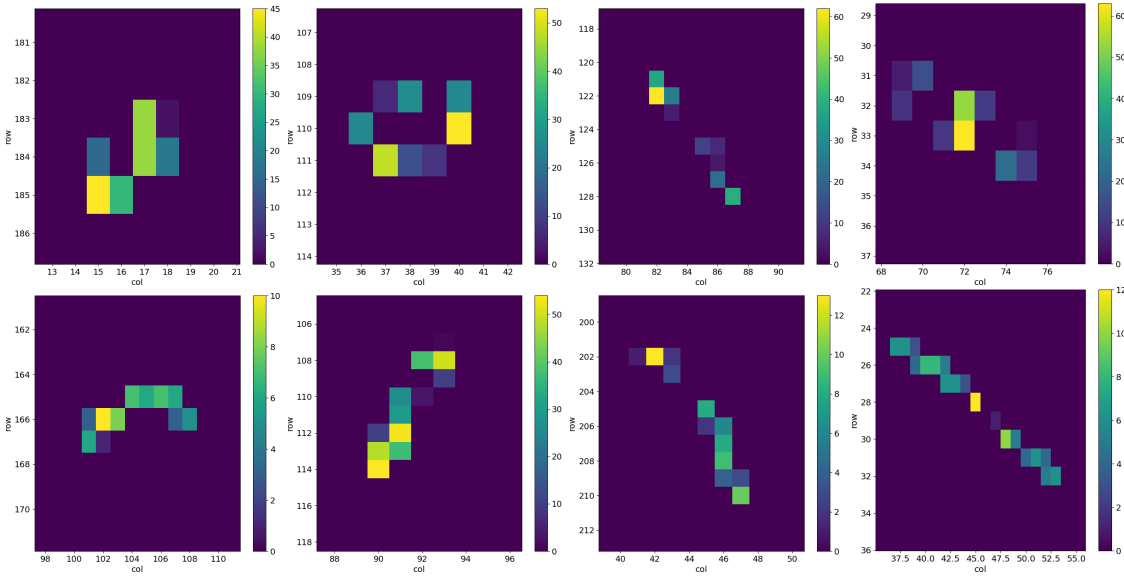


Figure 4.14: 2D histograms of the ToT in different events in an aquisition of cosmic rays.

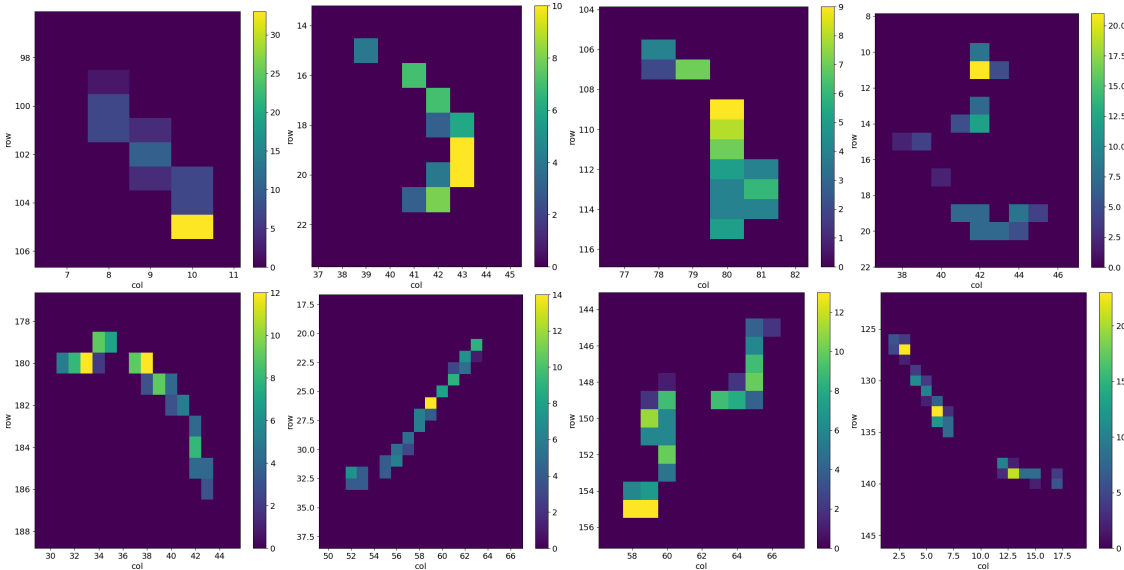


Figure 4.15: 2D histograms of the ToT in different events in an aquisition of Sr90.

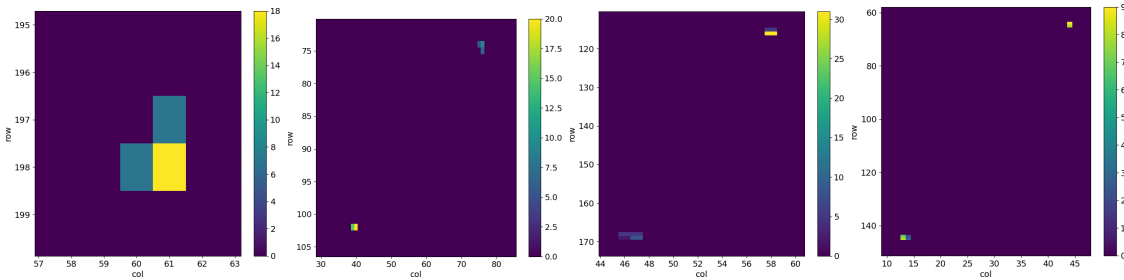


Figure 4.16: 2D histograms of the ToT in different events in an aquisition of Fe55

1368 photons which had converted at the boundary of nearby pixels thus sharing their charge  
 1369 among them. Starting from 4-pixels clusters the peak moves to the right: this is due to the  
 1370 fact that the cluster with more than 3 pixels are principally random coincidence events

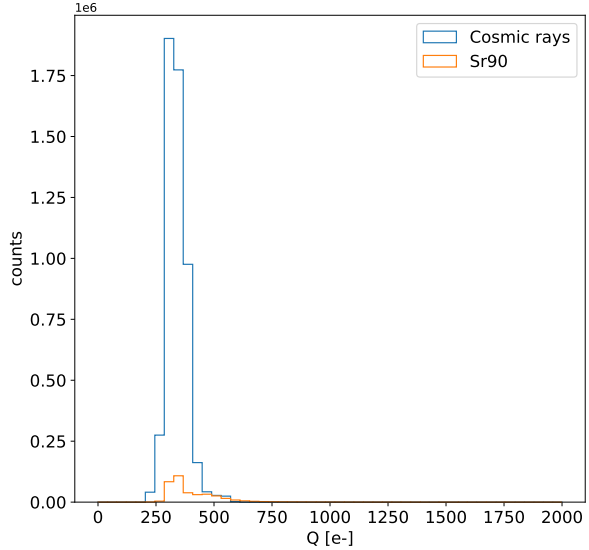


Figure 4.17: Histograms of the charge released in the pixels in events in which only a single pixel turns on.

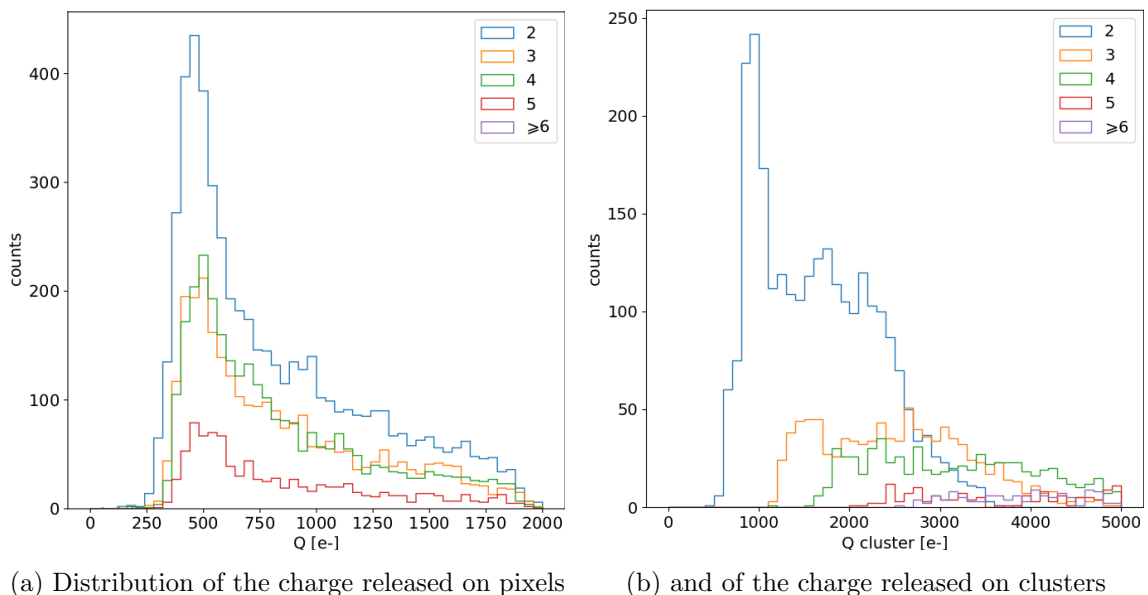
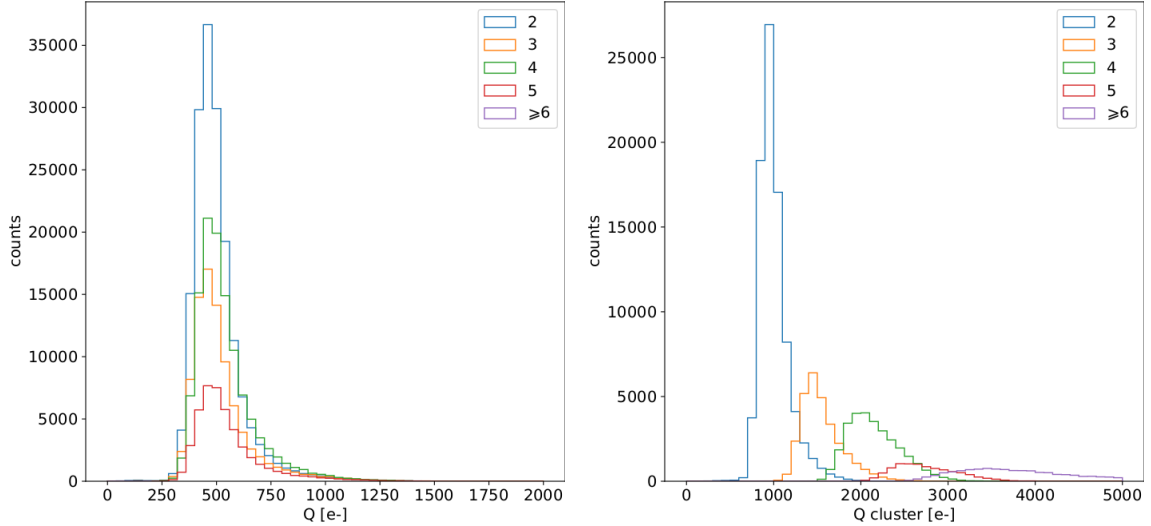


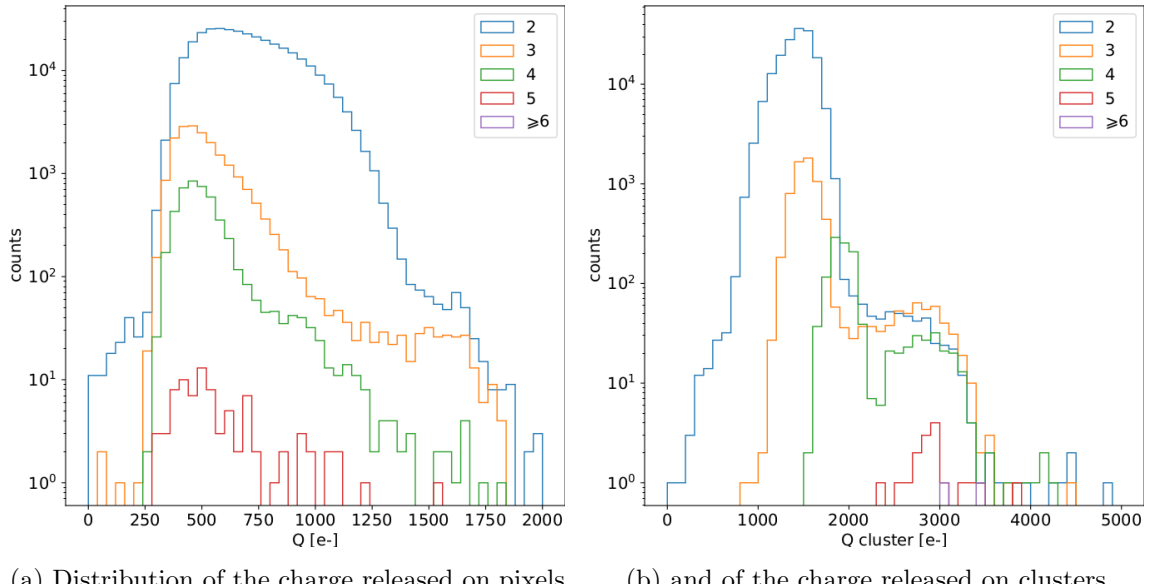
Figure 4.18: Acquisition of cosmic rays with the PMOS B flavor with the same FE setting of the calibration (in particular IDB=40 DAC)



(a) Distribution of the charge released on pixels

(b) and of the charge released on clusters

Figure 4.19: Acquisition of the Sr90 with the PMOS B flavor with the same FE setting of the calibration (in particular IDB=40 DAC)



(a) Distribution of the charge released on pixels

(b) and of the charge released on clusters

Figure 4.20: Acquisition of the Fe55 with the PMOS B flavor with the same FE setting of the calibration (in particular IDB=40 DAC)

1371 Fe55-Fe55 or Fe55-noise. Recalling that the noise typically just exceeds the threshold  
 1372 and then has low ToT, the peak position in the spectrum 4.20b of 4-pixel cluster can be  
 1373 explained admitting that one of the four pixel is a noise signal. The shoulder on the right,  
 1374 instead, which have an edge at about  $3200 e^-$  corresponds to the events with coincidence  
 1375 of two photons. Looking at the charge on the single pixel spectrum (fig.4.20a), instead,  
 1376 a small bump can be seen around  $1616 e^-$ : these events correspond to photons which  
 1377 released almost all the charge on one pixel.

#### 1378 4.1.6 Dead time measurements

1379 The hit loss is due to analog and digital pile up: the first one occurs when a new hit  
 1380 arrives during the pre-amplifier response to a previous event, the second instead when the  
 1381 hit arrives while the information of the previous hit has not yet been transferred to the  
 1382 periphery. Since the pre-amplifier response has a characteristic time  $\sim$ ToT, the dead time  
 1383  $\tau_a$  introduced by it will be at most  $1.6 \mu s$ ; using the IRESET and VRESET FE parameters  
 1384 the reset time can be lowered down, but as explained in section ?? it must be longer than  
 1385 the preamplifier characteristics time in order to not cut the signal. Regarding the latter  
 1386 contribution instead, since only one hit at a time can be stored on the pixel's RAM, until  
 1387 the data have completed the path to get out, the pixel is paralyzed. Moreover since there is  
 1388 no storage memory included on TJ-Monopix1 prototypes, the digital dead time  $\tau_d$  almost  
 1389 corresponds to the time needed to trasmit the data-packets off-chip.

1390 The exportation of data from pixel to the EoC occurs via a 21-bits data bus, therefore  
 1391 only one clock cycle is needed and the dead time bottleneck is rather given by the  
 1392 bandwidth of the serializer which trasmits data off-chip from the EoC. In our setup the  
 1393 serializer operates at 40 MHz, thus to transmit a data packet (27-bit considering the ad-  
 1394 dition of 6 bits to identify the double-column at the EoC) at least 675 ns are needed. For  
 1395 what we have said so far, the R/O is completely sequential and therefore is expected a  
 1396 linear dependence of the reading time on the number of pixels to read:

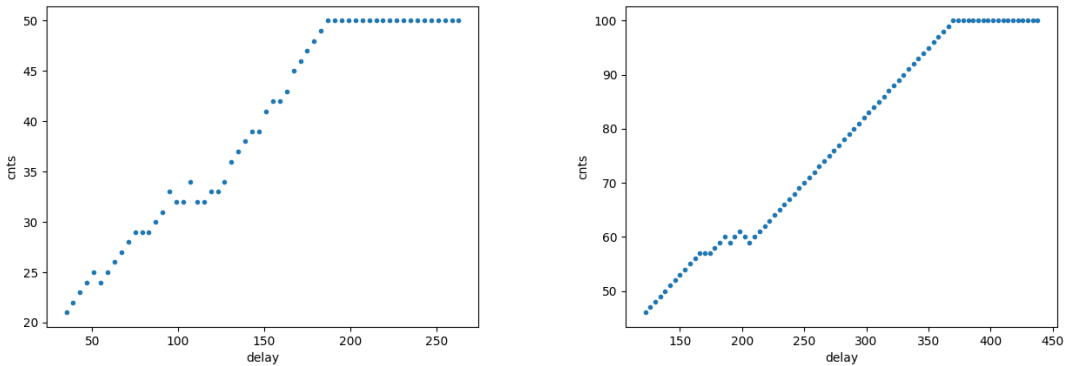
$$\tau = 25 \text{ ns} \times (\alpha N + \beta) \quad (4.13)$$

1397 where  $\alpha$  and  $\beta$  are parameters dependent on the readout chain setting.

1398 To test the linearity of the reading time with the number of pixels firing and to measure  
 1399 it, I have used the injection circuit which allows me choosing a specific hit rate: I made  
 1400 a scan injecting a fix number of pulses and each time changing the number of pixels  
 1401 injected. Indeed the injection mode allows fixing not only the amplitude of the pulse,  
 1402 which corresponds to the charge in DAC units, but also the time between to consecutive  
 1403 pulses (DELAY). The hit rate then corresponds to 25 ns/DELAY.

1404 Unfortunately a high random hit rate on the matrix cannot be simulated by the in-  
 1405 jection because of the long time ( $\sim ms$ ) needed to set the pixel registers of the injection;  
 1406 then I was forced to specify at the start of the acquisition the pixels to inject on, and for  
 1407 convenience I chose those on a same column. In figure 4.21 is shown the dependence of  
 1408 the efficiency on the DELAY parameter in two different cases. For the 5 pixels example  
 1409 the efficiency goes down the 90% at a DELAY of  $\sim 185$  clock counts, which corresponds to  
 1410  $4.625 \mu s$  and to a rate of 216 kHz, while in the 10 pixels example, the efficiency goes under  
 1411 the 100% at  $\sim 380$  clock counts, which corresponds to  $9.5 \mu s$  and to a rate of 105 kHz.

1412 From the efficiency curves I have then looked for the time when the efficency decreases.  
 1413 In figure 4.22(a) is shown the dead time per pixels as a function of N with different R/O



(a) Distribution of the charge released on pixels      (b) and of the charge released on clusters

Figure 4.21: Efficiency vs the DELAY parameters. (a) I made a scan injecting 5 pixels with 50 pulses for each DELAY configuration and (b) 10 pixels with 100 pulses for each DELAY

Parameter	Value [DAC]	Value [ $\mu$ s]
START_FREEZE	64	1.6
STOP_FREEZE	100	2.5
START_READ	66	1.65
STOP_READ	68	1.7

Table 4.4: Default configuration of the R/O: START and STOP refer to the begin and the end of the respective signals starting from the TE of the hit.

parameters configuration, the meaning of which is explained in chapter 3.1.3. The default value suggested by the designer of the chip are reported in table 4.4; moving too much the readout parameters from the default ones, the readout does not work properly, and no hits can be read at all. The problem probably comes from the firmware setting of the readout which are specially fixed for our chip. The single pixel readout time is independent of its position in the matrix, and it is equal to  $??\pm 1$  clock counts. However if many pixels are fire, the dead time  $\tau_d$  depends on the position because the reading sequence goes from row 224 to row 0, and from column 0 to column 112, making the pixel on the bottom right corner the one with the longest dead time.

Furthermore to test that there is no dependence of the digital readout time from the charge of the pulse, I have tried to change the amplitude of the pulse injected, but the parameters found were consistent with the default configuration ones. No difference in the  $\alpha$  and  $\beta$  coefficients has been observed between the two cases. Referring to eq.4.13, the factor  $\alpha$  is proportional to the difference (STOP\_FREEZE - START\_READ), while the offset  $\beta$  lies between 5 and 15 clock counts.

The readout time found by this test is so long because in the prototypes no parallelization of the informations (with the introduction of more serializer for example) and no storage memory are included; this feature are typically added in the final prototypes. An example closely linked to TJ-Monopix1 is OBELIX: it will include on the chip a storage buffer to optimize the dead time and to keep a low occupancy even at high fluence.

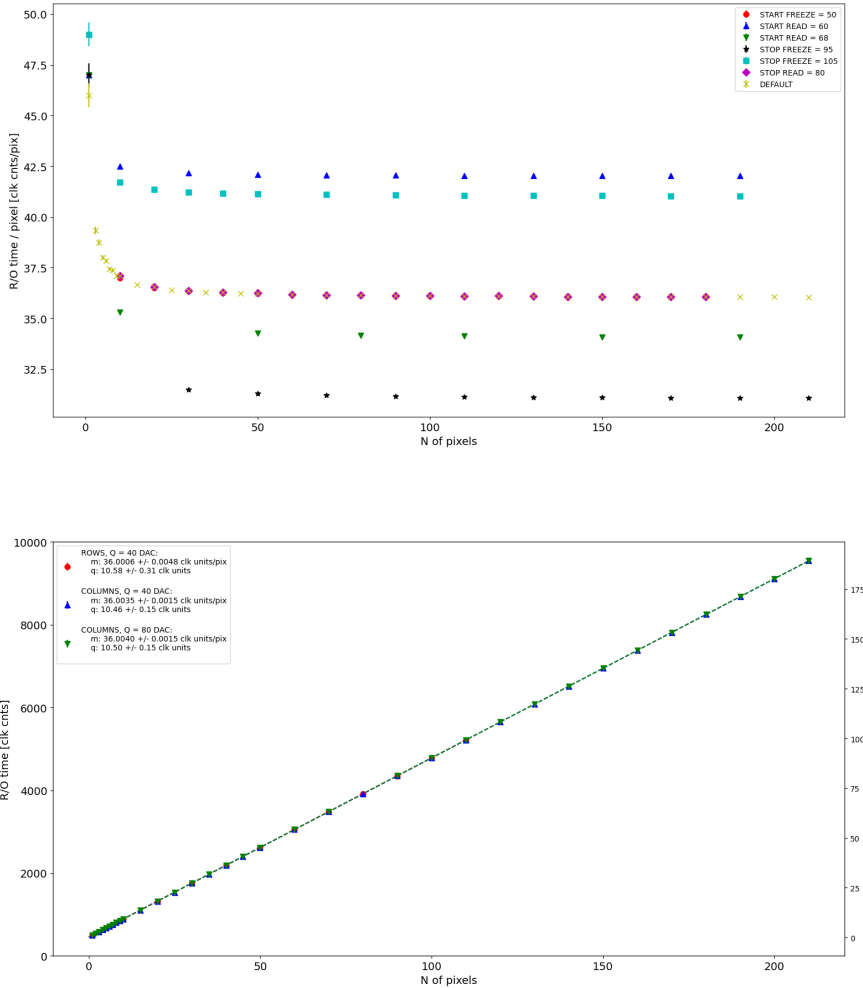


Figure 4.22: (a) Readout time per pixel as a function of the number of pixel injected obtained with different FE setup. (b) Readout time as a function of the number of pixels injected obtained injecting pulses with amplitude of 80 DAC (green), of 40 DAC on the same row (red) and on the same column (blue).

## 1434 4.2 ARCADIA-MD1 characterization

1435 Unfortunately the characterization of MD1 has not yet been completed because of some  
 1436 problems with the functionality of the first chip we received on which we have been able  
 1437 to make only a few electrical and communication test in order to test the operations of the  
 1438 FPGA and the breakout board (BB). We asked for another chip then but, due to delay  
 1439 in the extraction and the bonding of the wafer, we have received it only about one week  
 1440 ago; an initial characterization and testing of the new chip is going on in the clean room  
 1441 on the INFN, and I am going to show here only some preliminary results.

1442 The problem with the damaged chip occurs when it is biased, in particular, when the  
 1443 HV voltage is lowered down 0 V, the sensor requires too much power and a too high current  
 1444 draw sets. We have discussed the problem with the designers of the chip whose helped us  
 1445 identifying the motivation of the malfunction: the chip has been glued using too much  
 1446 conductive tape and hence have a short-circuit between the sides and the back, which

1447 makes impossible the biasing. Unfortunately, since both the sensor and the FE require at  
1448 least -10 V to work properly, no measurement was possible except the acquisition of the  
noise in the FE circuit.

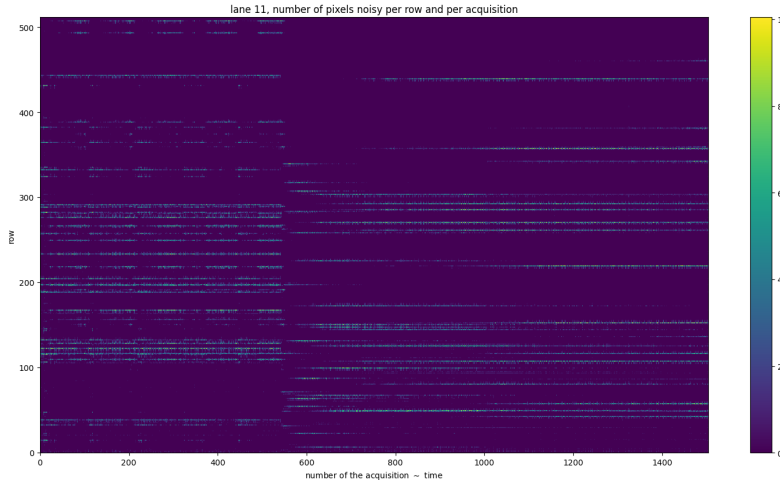


Figure 4.23: Noise in the front end circuit depending on the bias road across the matrix was recorded.

1449  
1450 The second chip we received is a minid2, that is a "mini demonstrator" from the second  
1451 submission. The two have the same characteristics but the minid2 is smaller than the MD1,  
1452 in particular it only have  $32 \times 512$  pixels, instead of  $512 \times 512$ .

1453 Up to now we used the injection circuit in order to make a threshold scan on a few  
1454 pixels: differently from the TJ-Monopix1's characterization where we performed a scan  
1455 changing the injection charge of the pulse, with the minid2 we have instead changed the  
1456 threshold (whose register is VCASN) keeping the charge of the pulse fixed. For each  
1457 threshold we inject 100 pulses of amplitude 10  $\mu$ s. The dependence of the efficiency on the  
1458 threshold for two pixels is shown in figure 4.24. Even if the behavior is reasonable, as the  
1459 threshold is reduced the efficiency becomes higher, it is possible that the bias (-50 V) is  
1460 not enough to full deplete the sensor, since the counts does not reach the 100% steadily.

1461 The value of the SNR and the ENC Charge injection circuit uses  $C_{inj} = 2.325$  fF. The  
1462 SNR, the ENC and the threshold dispersion on the matrix are expected to be respectively  
1463  $\sim 90$ ,  $3 e^-$  and  $\sim 35 e^-$  with a detector capacity of 7 fF, that is about the capacity expected  
1464 for the detector. The injection capacity is expected to be  $\sim 2.325$  fF, and in this condition  
1465 the minimum and maximum signals generated are respectively 0.08 fC and 2.6 fC.

1466 Substantial differences have been observed with VCASN=40 DAC in both the efficiency  
1467 and the threshold among the sections; this suggests that with this particular FE config-  
1468 uration there is a big threshold dispersion on the matrix. The hitmap of an acquisition  
1469 with the Fe55 source is shown in figure 4.25: the whole MD1 matrix with only the bottom  
1470 region (32 rows) working is represented in (a), while in (b) there is a zoomed hitmap. The  
1471 rate seen within the region 8 (green region in the figure (a)) is compatible with the rate  
1472 of the same radioactive source measured with TJ-Monopix1, that it  $\sim 3.3$  kHz.

1473 Looking to the Sr90 acquisitions (fig.4.26) many clusters and tracks can be immidiately  
1474 distiguished, confirming what observed with TJ-Monopix1. More tests will be performed  
1475 in the future to fully characterize ARCADIA-minid2.

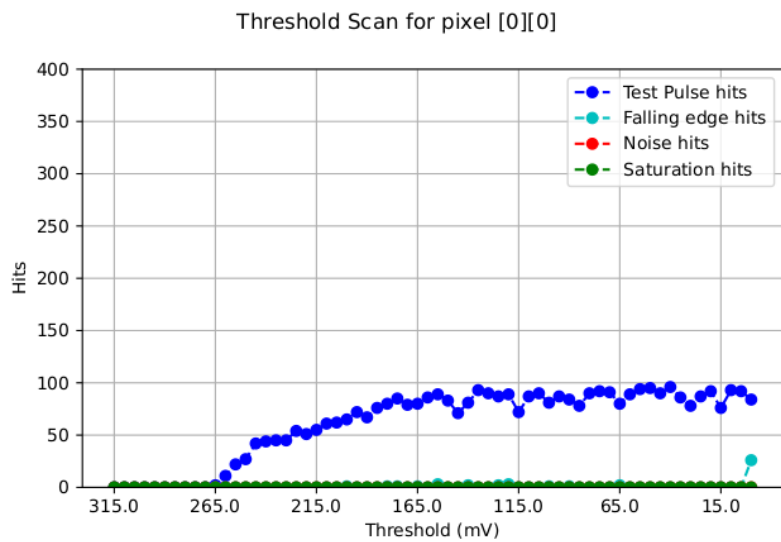


Figure 4.24: Threshold scan on the pixel (0,0). The sensors is polarized with  $\Delta V=-50$  V.

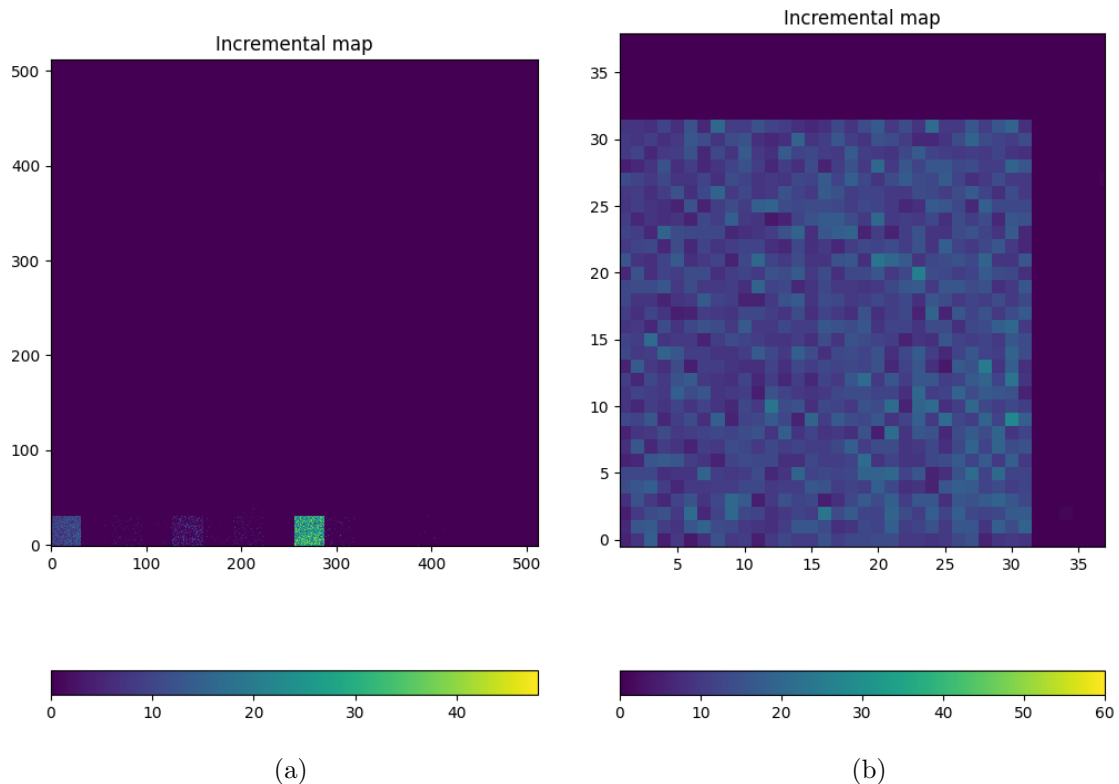


Figure 4.25: Fe55 acquisitions with VCASN=40 DAC. (a) All the matrix  $512 \times 512$  is plotted even if the minid2 has only the rows in range 0-32. (b) A zoom on the first section (col 0-32).

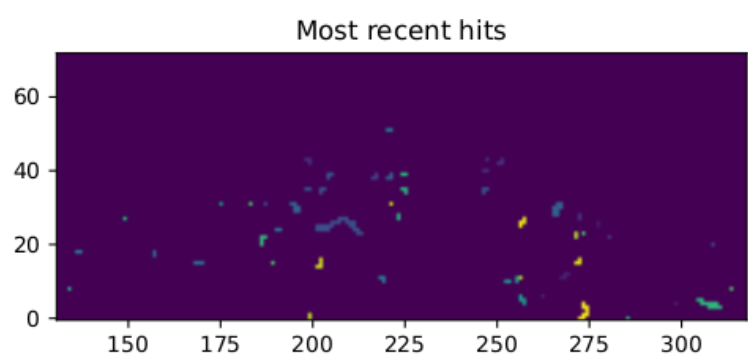


Figure 4.26: Sr90 acquisition with VCASN=40 DAC. The different colours are related with the time of arrival of the hits: in yellow the most recent hits, while in blue the old ones.

1476 **Chapter 5**

1477 **Test beam measurements**

1478 During August 2022 a testbeam took place in Santa Chiara hospital in Pisa, where a  
1479 new accelerator designed for both medical research and R&D on FLASH-RT, and for this  
1480 reason called "ElectronFlash", have been installed a few months ago. The motivation  
1481 of the testbeam measurements were testing TJ-Mopopix1 at high dose rate with a focus  
1482 on investigating the possibility of the application in radiotherapy. Despite this particular  
1483 device does not seem fitting the requirements imposed for that application, especially  
1484 regarding the readout time, the measurements have been useful since help us characterizing  
1485 the setup for future advance, and also give us the possibility of a complete characterization  
1486 of the chip.

1487 Given that in medical physics the dose is the standard parameter to characterize the  
1488 beam, because of its obvious relation with the damage caused in the patient, I am going  
1489 to explain the meaning of it by the point of view of the instrumentation. Infact, when  
1490 interacting with measuring systems a more common and useful parameter is the rate or  
1491 the fluence of particles. The conversion between the two quantity can be found thinking to  
1492 the definition of dose: it is the concentration of energy deposited in tissue as a result of an  
1493 exposure to ionizing radiation. Assuming total absorption of electrons in water, defined  
1494 by law as the ordinary reference medium, the dose can be expressed as:

$$D[Gy] = \frac{NE[eV]}{\rho[g/cm^3]A[cm^2]x[cm]} \quad (5.1)$$

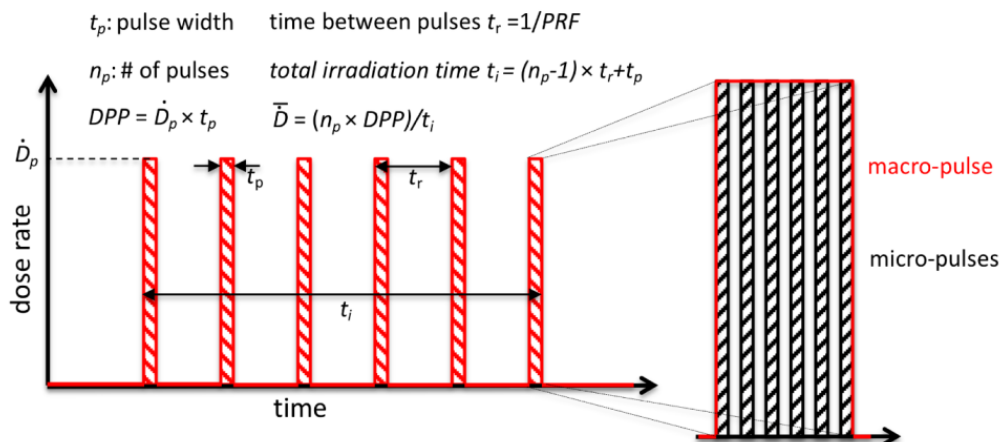


Figure 5.1: Typical beam structure of a beam used in electron radiotherapy

$\bar{D}$	Dose rate (mean dose rate for a multi-pulse delivery)	0.005-10000 Gy/s
$\dot{D}$	Intra pulse dose rate (dose rate in a single pulse)	0.01-1 $10^6$ Gy/s
DDP	Dose in a single pulse	0.04-40 Gy
PRF	Pulse repetition frequency	1-350 Hz
$t_p$	Pulse width	0.2-4 $\mu$ s
n	Number of pulses	single/pulse train

Table 5.1: The parameters that can actually be set by the control unit are the PRF, DDP,  $t_p$  and n (in particular the modality of singular irradiation or pulse train), while the other changes consequently.

1495 After having applied the conversion of the energy from eV to J and noticed that  $E/\rho x$   
 1496 roughly corresponds to the stopping power S of electrons in water, a simple estimation of  
 1497 the dose released in water is:

$$D[Gy] = 1.602 \cdot 10^{-10} N[cm^{-2}] S[MeV cm^2/g] \quad (5.2)$$

## 1498 5.1 Apparatus description

1499 In order to shield the outdoor from ionizing radiation the accelerator is placed in a bunker  
 1500 inside the hospital. The bunker has very thick walls of cementum and both the control  
 1501 units of the accelerator and of the detector were placed outside in a neighbor room.

### 1502 5.1.1 Accelerator

1503 The ElectronFlash accelerator is an electron Linear Accelerator (LINAC) with two energy  
 1504 configurations, at 7 MeV and 9 MeV, and it can reach ultra high intensity (40 Gy/pulse)  
 1505 keeping the possibility of accessing many different beam parameters and changing them  
 1506 independently from each other, a characteristic that makes it almost unique worldwide  
 1507 and which is fundamental for research in FLASH-RT, both for the medical aspects<sup>1</sup> and  
 1508 for the studies on detectors. The accelerator implements the standard beam structure  
 1509 used in RT with electrons (fig. 5.1), that is a macro pulse divided in many micropulses;  
 1510 the parameters used to set the dose and their range of values settable by the control unit  
 1511 is reported in table 5.1.

1512 The accelerator is also provided of a set of triod cannons  $\sim 1.2$  m long and with diameters  
 1513 in range from 1 cm to 12 cm and a collimator that can be used as beam shaper to  
 1514 produce a squircle shape. The triode, which is made by plexiglass, must be fix to the gun  
 1515 during the irradiation and is needed for producing, via the scattering of electrons with it,  
 1516 an uniform dose profile (fig.5.2) which is desired for medical purpose.

### 1517 5.1.2 Mechanical carriers

1518 The tested detector consists in one chip, the Device Under Test (DUT), mounted on a  
 1519 board and connected to FPGA with same arrangement of figure 4.25b. These boards  
 1520 have been positioned vertically in front of the triode on a table specifically built for the

---

<sup>1</sup>For example, it is not yet really clear the dependence of the efficacy of the FLASH effect on the whole beam parameters

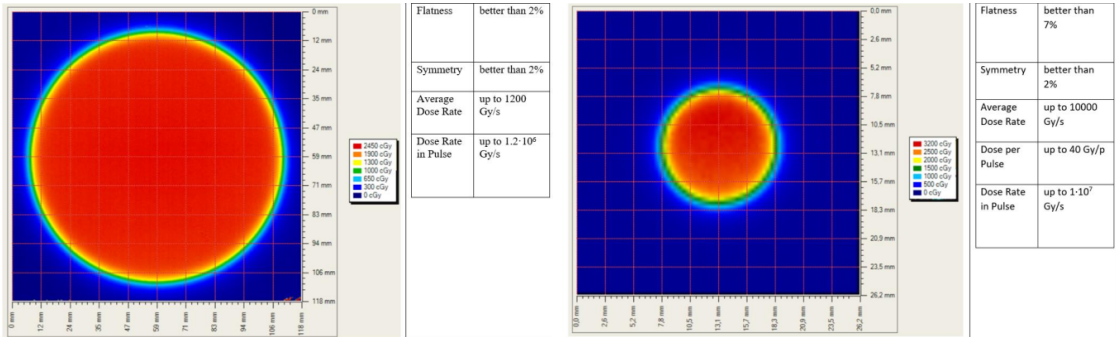


Figure 5.2: Two example of x-y isodose curves for two different triodes, 10 cm and 1 cm respectively, reported by the producer in the manual with the specific of the accelerator (S.I.T. - Sordina IORT Technologies S.p.A.). With the smaller collimator the dose rate in pulse is comparatively higher.

1521 testbeam. The tree board have been enclosed in a box of alluminium with a window on  
 1522 the DUT and with the required holes at the side to enable the biasing via cables and the  
 1523 connection with the DAQ provided via ethernet cable. A trigger signal coming from the  
 1524 control unity and syncronized with the pulses emitted from the beam has been also sent to  
 1525 the FPGA. This digital signal cannot be considered a real trigger, since the TJ-Monopix1  
 1526 prototype has been designed to be triggerless, but its Time of Arrival (ToA) had allowed  
 1527 the reconstruction of the correct timing during the analysis.

1528 In order to shield the sensor from the whole particles emitted from the gun, two  
 1529 alluminium collimators have been fabricated: one has been positioned at the triode exit  
 1530 while the other in front of the DUT. The collimators are  $t=32$  mm thick and have a  
 1531 diameter  $d$  equal to 1 mm: assuming a beam divergence bigger than  $d/t=1/32 = 1.8^\circ$ ,  
 1532 which is the case, the collimator at the triode output was supposed to work as a point  
 1533 source and to reduce the rate on the DUT of a factor at least  $4 \cdot 10^{-4}$ . The second one,  
 1534 being near the DUT, was instead supposed to shield the sensor from the electrons which  
 1535 have passed the first one, except for a region of  $1 \text{ mm}^2$  configurable using **come si chiamano**  
 1536 **quei cacciavitini per settare la posizione? sliding trimmer?**.

## 1537 5.2 Measurements

1538 Because of the dead time of TJ-Monopix1 it is not possible resolving the bunch sub-  
 1539 structure and almost no one pixel can read more than a hit per bunch. I recall, indeed,  
 1540 that the dead time per pixel depends on the location on the readout priority chain and  
 1541 for each pixel  $\lesssim 1 \mu\text{s}$  are needed; therefore, assuming a pulse duration of  $4 \mu\text{s}$ , only a few  
 1542 pixels at the top of the priority chain (placed at the upper left on the matrix) can fire a  
 1543 second time, as they can be read a first time before the end of the pulse and then can be  
 1544 hit again.

1545 Since resolving the single electron track is impossible, a way this sensor could be used  
 1546 in such context is reducing its efficiency and taking advantage of the analog pile up and  
 1547 of the linearity of the analog output (ToT), in order to see a signal produced not by the  
 1548 single particle but by more electrons. Reducing the efficiency and the sensibility of the  
 1549 sensor is essential in order to decrease the high charge signal produced in the epitaxial  
 1550 layer and mitigating the saturation limit: the smaller the output signal produced by a

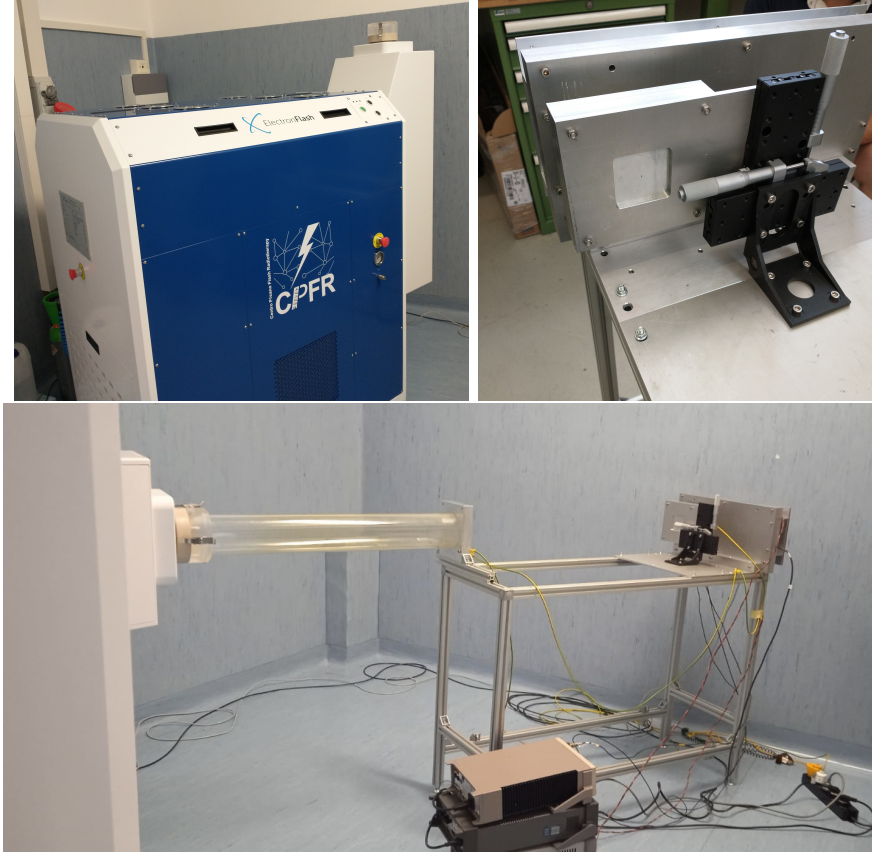


Figure 5.3: Experimental set up. (a) ElectronFlash accelerator: a rotating gantry allows the gun orientation from  $0^\circ$  to  $90^\circ$  (horizontal /vertical). (b) Collimator and DUT box. (c) Whole structure mounted: we used the 10 cm diameter and 1.2 m long triode; the DUT which is in the box behind the two collimators is connected to the power supply units.

1551 particle and the higher the fluence the detector can cope with. There is an obvious limit in  
 1552 this context that is the ToT rollover, indeed, the signal stop giving information when this  
 1553 value has been overridden and is no more bijective. With the standard configuration of  
 1554 the FE parameters and the epitaxial layer completely depleted, a MIP produces a charge  
 1555 at the limit of representation with a 6-bit ToT; to obtain smaller output signals one can  
 1556 operate on the reduction of the gain.

1557 Recalling the results in section 4.1.4, I have shown that concerning the PMOS flavor  
 1558 B, reducing the bias from -6 V to 0 V brings a reduction of efficiency down to 40 %, and a  
 1559 reduction in the gain of a factor  $\sim 1/3$ , while the reduction of the gain of the preamplifier  
 1560 allows a reduction of **circa 10, ma da controllare**.

1561 In order to take advantage of the analog pile up and integrating the charge, for  
 1562 simplicity assume of two electrons, the second one must hit the pixel before the ToT goes  
 1563 under the threshold. The general condition is then  $\overline{\Delta T} < \overline{ToT}$ , but if a high  $P_\mu(n \geq 1)$  is  
 1564 required, a lower  $\overline{\Delta T}$  may be desired:

$$P(n \geq 1) = \sum_{n=1}^{\infty} \frac{e^{-\mu} \mu^n}{n!} = 1 - P(0) = 1 - e^{-\mu} \quad (5.3)$$

1565

$$\mu = \frac{\overline{ToT}}{\overline{\Delta T}} \quad (5.4)$$

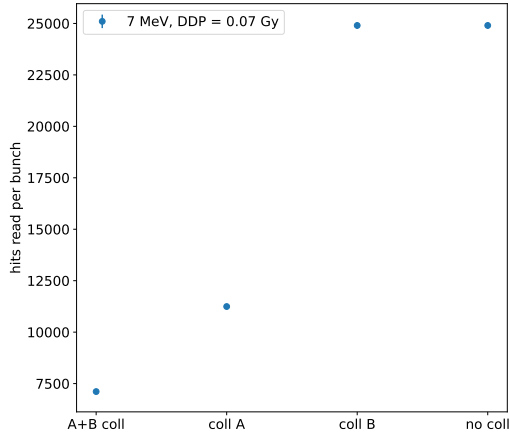


Figure 5.4: Mean number of hits read per bunch at DDP=0.07 Gy, with all the possible setup condition: with both the collimator, with only the collimator far from the chip (A), with only the collimator near the chip (B), and without any collimator.

1566 If a  $P_\mu(n \geq 1) = 99\%$  then the  $\overline{\Delta T}$  must be  $\sim 0.22 \overline{ToT}$ . The ToT is in range [0,64] but  
 1567 since the rollover must be avoided, the  $\overline{ToT}$  must be lower than 32, and then the minimum  
 1568 rate on the pixel must be 1.25 MHz.

1569  
 1570 During the testbeam many runs have been performed, spanning the energy, the dose  
 1571 per pulse and the four possible configurations with/without the collimators. We have  
 1572 collected data with the PMOS flavor A in the standard configuration: with the PWELL  
 1573 and PSUB biased at -6 V and set the standard default FE parameters reported in table  
 1574 ???. During all the data acquisitions we have selected on the control unit of the accelerator  
 1575 pulses with  $t_p$  of 4  $\mu$ m and with the smallest PRF settable, which is 1 Hz, in order to start  
 1576 in the most conservative working point excluding the digital pile up of events from different  
 1577 bunches. In these conditions, even if the whole matrix turns on, the total readout time  
 1578 corresponds to  $25000 \times 1 \mu s = 25 \text{ ms}$  is still lower than the time between two consecutive  
 1579 pulses. In figure 5.4 is shown the mean number of hits read during one accelerator pulse  
 1580 in different setup condition.

1581 The readout starts with the trailing edge of the first pulse going down the threshold:  
 1582 about 50 clk=1.25  $\mu$ s after this moment the FREEZE signal is sent to the whole matrix,  
 1583 and the transmission of the data to the EoC begins. The hits read during the FREEZE  
 1584 signal are the ones whose TE occurred before the start of the FREEZE and which have the  
 1585 TOKEN signal high; the ones, instead, whose TE occur during the FREEZE are stored in  
 1586 the pixel memory until the end of the FREEZE. At this point a second readout starts and  
 1587 a second FREEZE is sent to the matrix. An example of the two sub-pulses corresponding  
 1588 to an electron bunch is shown in figure 5.5: in the acquisition we injected 5 pulses with  
 1589 both the collimators mounted on the table. Looking at the spectrum we can see that the  
 1590 second sub-pulse has a populated tail on the right; this is due to the fact that the hits  
 1591 which arrive before the start of the first FREEZE but have a long ToT that falls during  
 1592 the FREEZE, are read at the second sub-pulse.

1593 The 2D histograms in figure 5.5, reveal an important characteristics of our setup: in

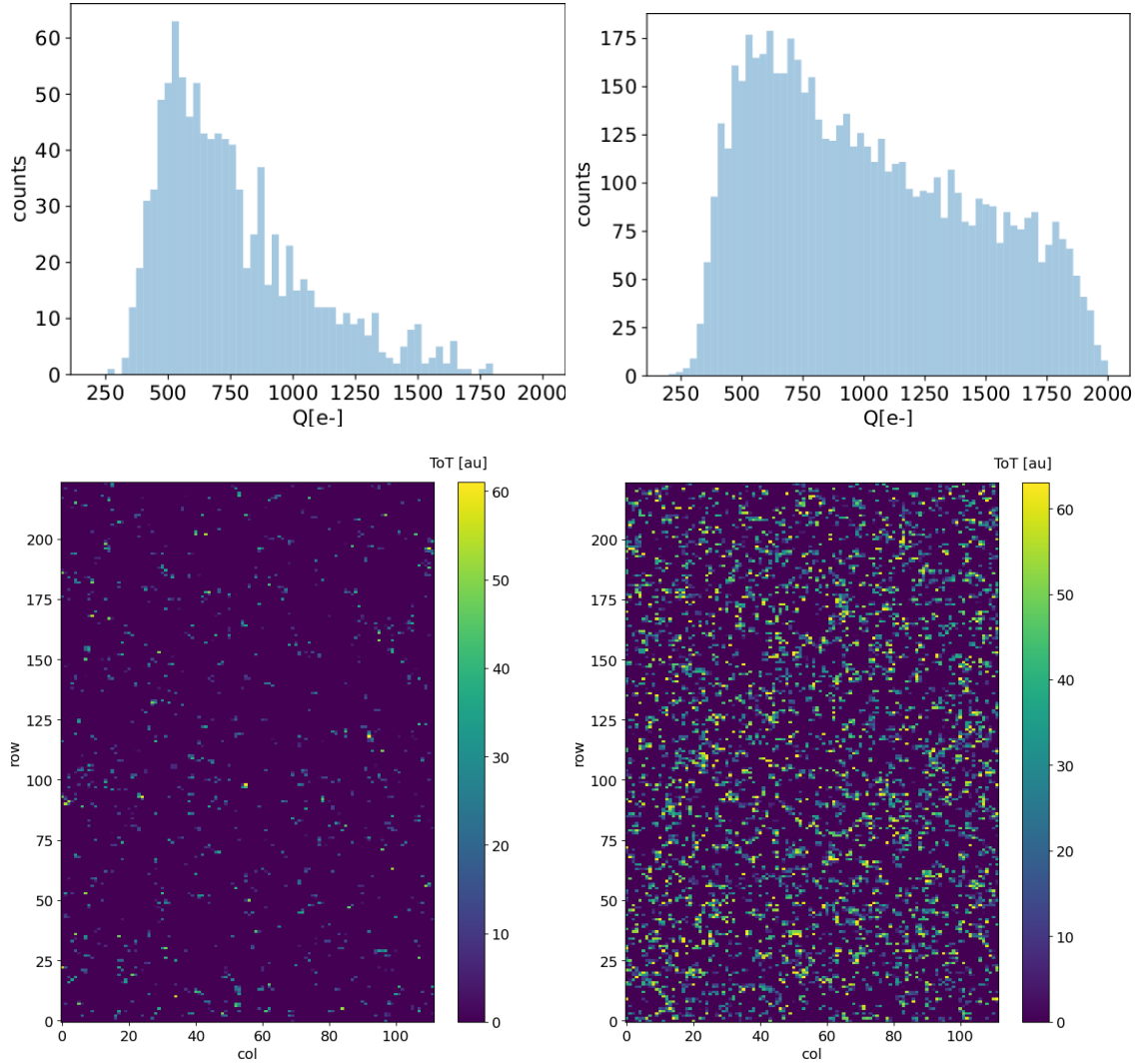


Figure 5.5: Acquisition with both the collimators: 5 pulses at  $DDP=0.07\text{ Gy}$ . (a) Spectrum of the charge released in the sensor: to apply the conversion I used the information found in the previous chapter. (b) 2D histogram of the ToT of the hits arrived in the sub-pulses.

fact, being uniform and not showing disomogenities, it follows that the collimators do not shield all the particles. We supposed that this was due to a Bremsstrahlung photon background higher than expected but a full verification of that and the analysis of the data is still going on. In figure 5.6, instead, the histograms with a higher DDP value is shown; in the example the matrix turns on completely, but again this happens in two different consecutive read chain.

When we have put aside the collimators, instead, the fluence increase a lot and the two-pulses substructure no more appears (fig. 5.7), but, because of the high attivity of the matrix, after each readout new hits with a fixed ToT were induced due to crosstalk. This problem had already been observed on other prototypes of TJ-Monopix1, and thanks to a simulation it has been observed that the main source of crosstalk is the voltage drop of the pre-amplifier ground as a result of the accumulated current that is drawn from the discriminator.

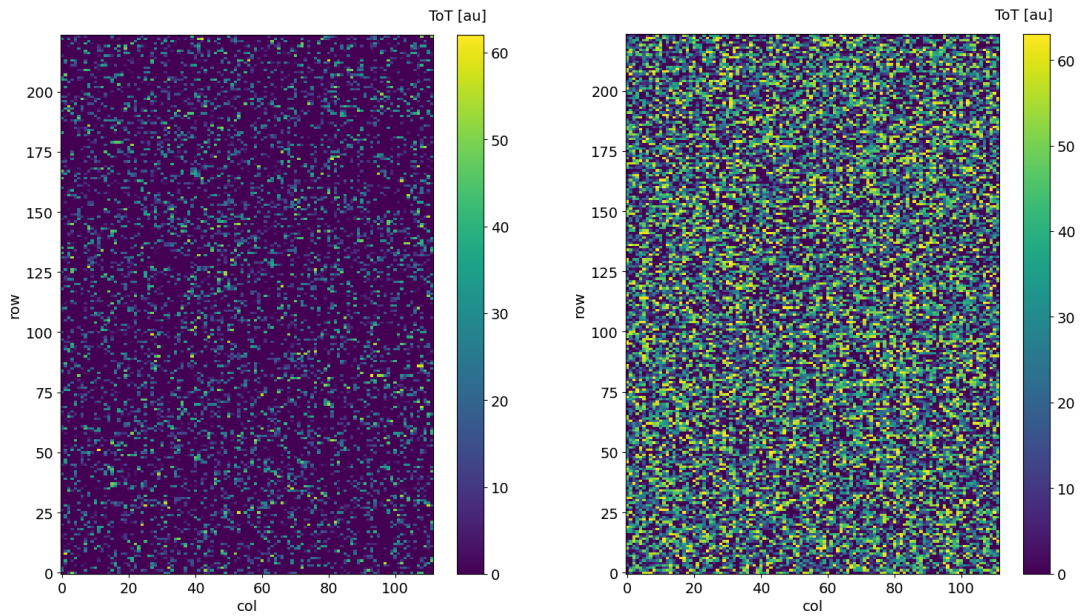


Figure 5.6: Acquisition with both the collimators: 5 pulses at  $DDP=0.6\text{ Gy}$ . 2D histogram of the ToT of the hits arrived in the sub-pulses. Compared with the previous maps, since the DDP is much higher, more pixels turn on.

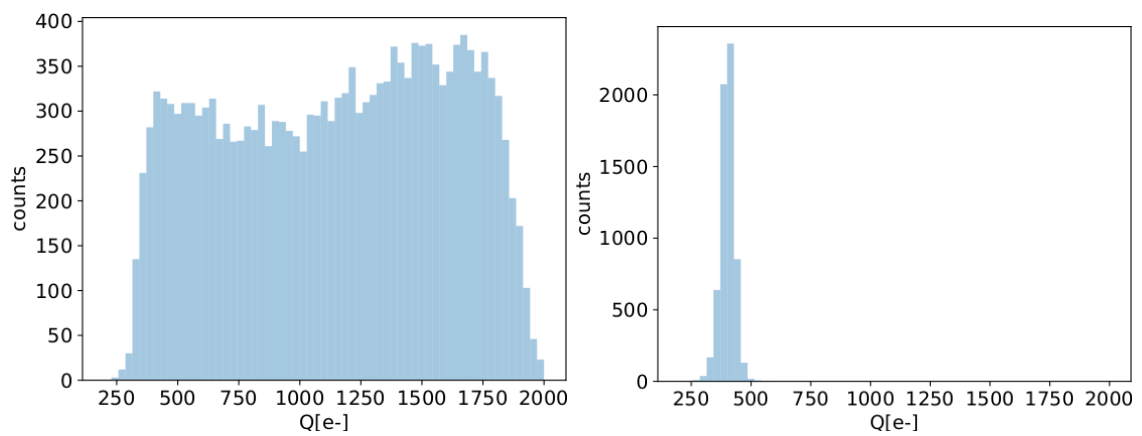


Figure 5.7: Acquisition without any collimator: 5 pulses at  $DDP=0.04\text{ Gy}$ .